Probing the Magnetic Properties of $[\mathbf{Mn}_6^{\mathrm{III}}\mathbf{Cr}^{\mathrm{III}}]^{3+}$ Single-Molecule Magnets by XAS, XMCD and Spin-Resolved Electron Spectroscopy

Dissertation

for awarding the degree of

Doktor der Naturwissenschaften
(Dr. rer. nat)

Faculty of Physics
Bielefeld University

submitted by
Andreas Helmstedt

15. October 2014

Printed on acid free, aging resistant paper according to °° ISO 9706.
Gedruckt auf alterungsbeständigem Papier entsprechend °° ISO 9706.

Contents

List of Figures

1. Motivation

With the wide success of digital technologies in almost every aspect of human life, the impressive amount of approx. 250 Exabytes (1 Exabyte equals 10^{18} byte) of data has been produced worldwide in 2009 [1], with an estimated increase to 1000 Exabytes in 2010. Data storage mainly relies on hard disk drives based on the magnetic recording principle that was first employed by *V. Poulsen* in 1898 [2]. The first hard disk drive was introduced by IBM in 1956 [1], featuring a recording density of approx. 0.002 Mbit/inch^2 [3]. Figure 1.1 visualizes the development of hard disk drive recording densities between 1980 and 2009.

Up to 2009, the recording density had increased to 0.25 Tbit/inch^2 [1], facilitated by the fact that a scaling principle exists for magnetic recording technology [3–5]: Reducing all physical dimensions corresponding to the magnetic read process by the same scale factor results in an unchanged output waveform amplitude [6]. The magnetic writing process scales as well, as long as the applied *write gap field H* is kept constant [6]. Experimental proof for the validity of this scaling principle has been given [7].

The introduction of hard disk drive read heads based on the *giant magnetoresistance* (GMR) effect discovered by *P. Grünberg et al.* in 1996 [8, 9] represents a milestone in the miniaturization of the magnetic recording process, allowing to overcome the noise limitations associated with the inductive pickup method [1]. The practical significance of the GMR discovery was honored by awarding the 2007 Nobel Prize in Physics to P. Grünberg and A. Fert [9].

While the transition from longitudinal to perpendicular magnetic recording [10, 11] in 2005 [1] represented an important step beyond the limitations of the longitudinal recording process, a more severe limit is rapidly approached: Beyond a critical recording density of approx. 1 Tbit/inch^2 [4, 12], thermal fluctuations can overcome the energy barrier of the magnetized areas against magnetization reversal, leading to a thermally (or magnetic field [13]) induced loss of information [4, 5, 14]. This *superparamagnetic limit* [4, 14, 15] is correlated to a magnetic grain size of approx. 10 nm [14]. Single magnetic grains beyond this limit exhibit a superparamagnetic [16] behavior characterized by the absence of a magnetic hysteresis and a linear response to magnetic fields [15].

Possible ways to overcome these physical limits are the use of bit patterned media or the heat-assisted magnetic recording (HAMR) [1, 12, 17, 18]. The first solution relies on microstructured media consisting of physically separated 'magnetic islands' each forming a single magnetic domain instead of a large number of grains with varying preferential directions (see figure 1 of [17]).

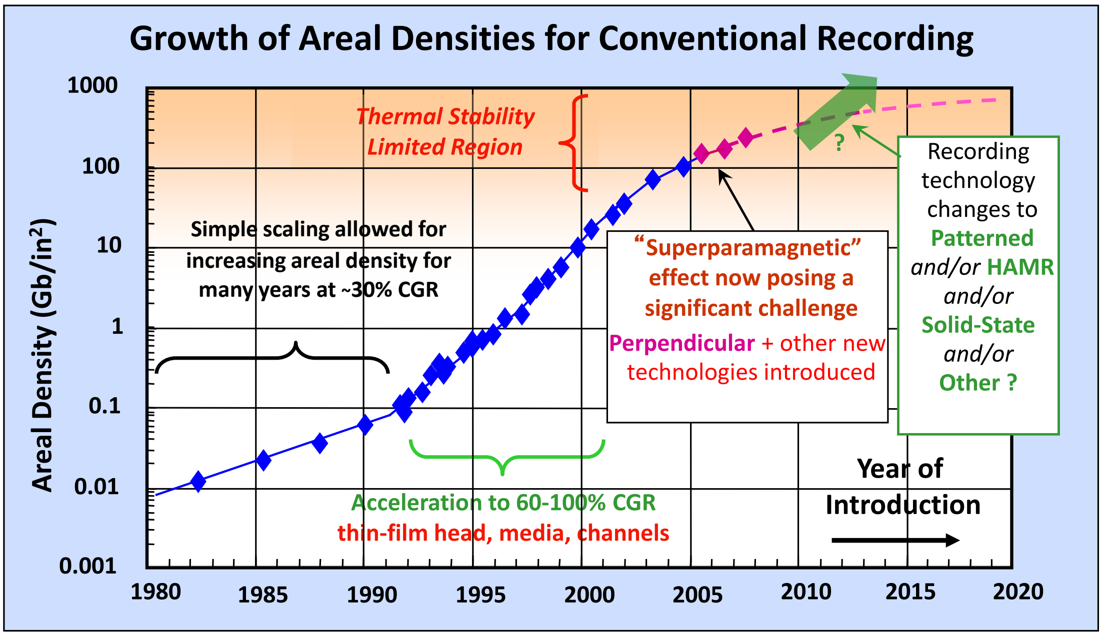

Figure 1.1. Development of hard disk drive recording densities between 1980 and 2009. While simple scaling methods determined the increase in recording density up to 1990, new technological developments like GMR read heads and thin film media [1] were required afterwards. Currently, the thermal stability of magnetization (superparamagnetic limit) represents the technological limit for the recording density. *Figure by courtesy of R. Wood (HGST Western Digital), reprinted from [1], ©2009, with permission from Elsevier.*

HAMR employs higher coercitivity materials and a local, reversible reduction of the magnetic anisotropy by external heating (e.g. by laser) to allow a change of the magnetization by the write head [12, 18].

With the ongoing technological trend to further miniaturization, efforts are made to move from bulk magnetic and semiconductor materials towards single molecules performing as memory units, diodes, transistors or complete logical devices [19–21]. A comprehensive review of logical devices based on single molecules is given in [22].

Single-molecule magnets (SMM) [23–25] represent a very promising approach in the fields of quantum computing and storage technologies [26–29]. Beyond the magnetic concepts, high-capacity information storage in artificially created DNA molecules is considered feasible today [30]. The first experimental proof of the successful grafting of single-molecule magnets to surfaces while maintaining their unique magnetic properties has been given by Mannini *et al.* [31] in 2009. Being able to deposit SMM on surfaces in a regular pattern represents an essential prerequisite with respect to technological applications: The magnetic molecules need to be adressed individually to access the stored information. Recently, a preferential orientation of $\mathbf{Fe_4}$ single-molecule magnets deposited on a gold surface was successfully established [32] and 3D arrays of SMM are investigated [33].

In contrast to the ’serendipitous approach’ [34] that lead to the discovery of the first single-molecule magnet $\mathbf{Mn_{12}ac}$ [35–37], rational bottom-up molecular design was utilized in the synthesis of the $\mathbf{[Mn^{III}_6Cr^{III}]^{3+}}$ single-molecule magnet [38–40] (see section 2.2). Antiferromagnetic coupling between the six Mn^{III} ions and the central Cr^{III} ion (see figure 2.2) leads to a high spin ground state of $S_t = 21/2$ for this SMM [38].

With respect to the remarkable properties of the $\mathbf{[Mn^{III}_6Cr^{III}]^{3+}}$ SMM, the investigation of this single-molecule magnet by suitable physical characterization methods constitutes the main task of the thesis presented here, with the determination of the local spin and orbital magnetic moments of the Mn constituents in $\mathbf{[Mn^{III}_6Cr^{III}]^{3+}}$ SMM being a central question. The possibility of influences on the $\mathbf{[Mn^{III}_6Cr^{III}]^{3+}}$ condition due to the preparation process, the deposition on substrates or the applied measurement methods is closely related to the main task and deserves consideration.

The X-ray Magnetic Circular Dichroism (XMCD) method has become a very useful tool for the investigation of magnetic properties [41–43] since latest generation synchrotron radiation sources (see section 3.1.1) became available. The technique requires magnetic orientation of the investigated samples (see section 3.3.2), which is usually obtained by the use of strong external magnetic fields and low-temperature setups.

However, the application of external magnetic fields represents an unwanted influence on the investigated systems. Distinct changes in the spectral shape of the Mn $L_{2,3}$ absorption have been observed in XAS measurements performed with and without external magnetic fields (see section 5.7.2), hinting to the existence of such influences.

It has been shown by N. Müller *et al.* [44] in 2001 that spin-resolved electron spectroscopy above the Curie temperature and without the application of external magnetic fields yields information comparable to XMCD data: Though the sample atoms are not oriented, spin-polarized electrons are excited using circularly polarized synchrotron radiation. This effect has been described by *U. Fano* in 1969 [45].

Hence the primary excitation step is spin-dependent in both methods – governed by the relativistic dipole selection rules [46]. Due to this common physical foundation, equivalent information about the local magnetic moments is available from XMCD and spin-resolved electron spectroscopy, if certain conditions (see page 86) are met. A thorough review of the broad application of spin polarized photoemission experiments has been given recently by *U. Heinzmann* and *J. H. Dil* [47].

In chapter 2 of this thesis, a short outline of the special properties of single-molecule magnets will be given, along with some basic considerations regarding the formalism of electron spin and spin-dependent scattering processes. The different methods employed within this thesis as well as the $\mathbf{[Mn^{III}_6Cr^{III}]^{3+}}$ preparation process will be introduced in detail in chapter 3. It is followed by a description of the UHV apparatus that has been developed and built for the measurements shown, see chapter 4. Spin polarization measurements and XMCD investigations of

$[\mathbf{Mn^{III}_6Cr^{III}}]^{3+}$ single-molecule magnets and reference substances are presented in chapter 5, along with a comparison of the results obtained from both methods (see section 5.7). X-ray absorption spectroscopy as another synchrotron radiation method was applied to characterize the **$[\mathbf{Mn^{III}_6Cr^{III}}]^{3+}$** samples and the influence of the preparation and the measurement process on the sample condition. A brief summary of the main results obtained within this thesis will be given in chapter 6.

2. Theoretical Background

Following the description of prospective applications of SMM in chapter 1, a short summary of the basic properties of single-molecule magnets will be given in section 2.1. Afterwards, the **$[\mathrm{Mn}_6^{\mathrm{III}}\mathrm{Cr}^{\mathrm{III}}]^{3+}$** SMM representing the main scientific concern of this work is introduced. The basic concept of the electron spin and its polarization is summarized in section 2.3, completing the brief overview of the theoretical background behind the measurements presented in chapter 5.

2.1. Single-molecule magnets

The term 'single-molecule magnet' [23] was established in 1996, following the discovery of the unexpected magnetical properties of the **Mn_{12}ac** [35] complex. It describes a class of coordination compounds which in most cases consist of various transition metal ions [39] carrying a non-vanishing spin magnetic moment due to their incompletely filled valence shell, embedded in a suitable organic ligand structure. The denomination for these compounds refers to the unique properties of single-molecule magnets with respect to their magnetic behavior:

- The existence of an easy-axis type **magnetic anisotropy**, characterized by a negative zero-field splitting parameter D (see [48], p. 17) and an **energy barrier** against spin reversal lead to a system showing magnetic bistability [25, 49].

- A **slow relaxation of the magnetization** occurs [50] for sufficiently low temperatures (blocking temperature, see [48]), which allows the conservation of the magnetic orientation for extended times. This behavior originates from a small number of coupled spins belonging to a single molecule [49], in contrast to the collective effects involving a large number of spins governing the 'classical' ferromagnetism (see figure 2.1 right).

The first transition metal complex showing these distinct magnetic properties was synthesized in 1980: The mixed-valence **Mn_{12}ac** complex [35] consists of eight $\mathrm{Mn}^{\mathrm{III}}$ ions arranged in a ring-shaped structure, viewed along the S_4 symmetry axis. They surround a central tetrahedron comprised of four $\mathrm{Mn}^{\mathrm{II}}$ ions [48]. The **Mn_{12}ac** SMM exhibits a spin ground state of $S_t = 10$ [48, 51], resulting from an antiferromagnetic coupling between the $\mathrm{Mn}^{\mathrm{II}}$ and $\mathrm{Mn}^{\mathrm{III}}$ ions, while the spin of all Mn ions of identical oxidation state has parallel orientation. This spin orientation

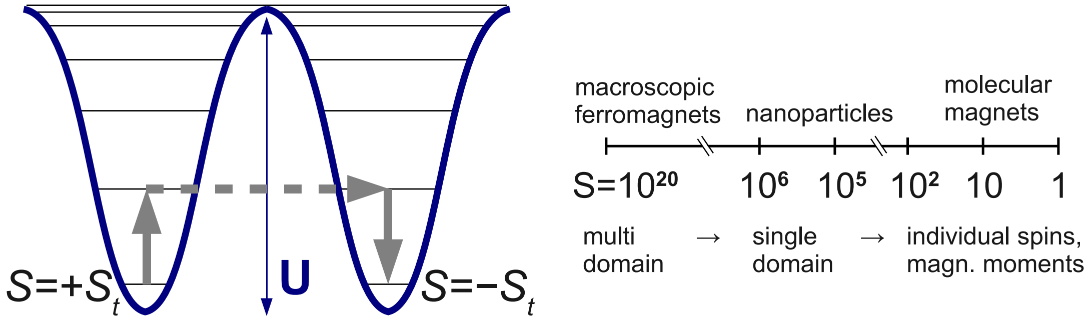

Figure 2.1. Left: The energy barrier against spin reversal present in single-molecule magnets depends on the magnetic anisotropy D as well as on the spin ground state S_t (see text). An alternative magnetization relaxation path by quantum tunneling is indicated by the grey arrows. Figure adapted from [53]. Right: Different magnetic regimes, depending on the number of spins involved. In contrast to macroscopic permanent magnets, SMM usually comprise a small number of magnetically active ions. Figure adapted from [54].

scheme has been verified experimentally [52] using polarized neutron diffraction ([48], p. 138). The magnetization relaxation process is sufficiently slow to observe magnetic hysteresis loops below approx. 2.5 K, see [49] and figure 4.25 of [48].

However, **Mn$_{12}$ac** and other single-molecule magnets have been discovered using 'serendipitous approaches' [34], without being able to predict or optimize the detailed magnetic properties of the synthesized compound. A 'rational design approach' [38] providing close control over the molecular topology was chosen for the $\mathbf{[Mn_6^{III}Cr^{III}]^{3+}}$ SMM instead, see [39, 51] for a thorough review on the topic. The key property concerning future applications of single-molecule magnets is the height of the energy barrier [51]

$$U \sim D \times S_t^2 \tag{2.1}$$

for spin reversal (see figure 2.1), limiting the practical applicability of SMM for information storage to very low operating temperatures. The ground state anisotropy D originates from the projection of the local anisotropies D_i onto the spin ground state S_t [38]. It has to be noted that this projection leads to cancellation effects resulting in a low total D for the case of a cubic symmetry [51]. Thermally activated quantum tunneling (see figure 2.1 left) provides an alternative relaxation path for the SMM magnetization [24, 48, 54] resulting in a loss of the information stored in the spin orientation.

Both problems can be solved by a purposeful SMM design controlling the molecular topology: While keeping the overall symmetry below the cubic case to avoid said cancellation effects, the introduction of an at least threefold symmetry axis completely suppresses the quantum tunneling [38, 51].

The $[\mathbf{Mn_6^{III}Cr^{III}}]^{3+}$ single-molecule magnet (see figure 2.2) investigated within this work has been one of the first results of the rational SMM design approach [38]. A short overview of its chemical and magnetic properties will be given in the following section.

2.2. The $[\mathbf{Mn_6^{III}Cr^{III}}]^{3+}$ SMM

Heptanuclear metal-organic complexes of the $\left[\mathbf{M_6^t\,M^c}\right]^{3+}$ structure type have been investigated thoroughly in the recent past [38–40, 53, 55–59]. The terminal metal ions have been varied ($\mathbf{M^t}$ = Mn, Fe) as well as the central hexacyanometallate ($\mathbf{M^c}$ = Mn, Cr, Fe, Co).

The first $\left[\mathbf{M_6^t\,M^c}\right]^{3+}$ complex exhibiting the expected single-molecule magnet behavior [39] is the $\left[\{(\mathrm{talen}^{t-\mathrm{Bu}_2})\mathrm{Mn}_3^{\mathrm{III}}\}_2\{\mathrm{Cr}^{\mathrm{III}}(\mathrm{CN})_6\}\right]^{3+}$ (abbrev. $[\mathbf{Mn_6^{III}Cr^{III}}]^{3+}$) SMM [38] that has been studied extensively within this work. It consists of two triplesalen-derived ligands $\mathrm{H_6talen}^{t-\mathrm{Bu}_2}$, each forming a bowl-shaped shell [60] embedding three $\mathrm{Mn^{III}}$ ions. Two of these are linked by a hexacyanochromate complex containing a central $\mathrm{Cr^{III}}$ ion, see figure 2.2. The special geometry of the triplesalen ligand facilitates the formation of heptanuclear complexes by applying a molecular recognition principle [55]: The non-planar structure of the ligand optimizes the position of the three metal ions for the formation of a bond with three nitrogen atoms of the hexacyanochromate complex [38, 56]. The approximate dimensions of the $[\mathbf{Mn_6^{III}Cr^{III}}]^{3+}$ core are 2.13 nm (diameter) by 1.22 nm (height) as shown in figure 2.2 [61].

The spin orientation scheme present in $[\mathbf{Mn_6^{III}Cr^{III}}]^{3+}$ is shown in figure 2.2: The $\mathrm{Mn^{III}}$ ions of each triplesalen subunit exhibit a parallel spin orientation, while the spin of the central $\mathrm{Cr^{III}}$ ion points in the opposite direction [39]. With both Mn and Cr being in a high-spin state (see figure 2.2), this leads to a total spin ground state of $S_t = 21/2$ [38, 62].

A comparison between temperature-dependent susceptibility measurements performed on $[\mathbf{Mn_6^{III}Cr^{III}}]^{3+}$ [38] and theoretical calculations allows an estimate of the coupling constants J_{Mn-Mn} between two $\mathrm{Mn^{III}}$ ions of one triplesalen unit and J_{Mn-Cr} between the terminal $\mathrm{Mn^{III}}$ ions and the central $\mathrm{Cr^{III}}$. The obtained value of $J_{Mn-Mn} = -1.03\ \mathrm{cm^{-1}}$ revealed the presence of a weak antiferromagnetic coupling between the $\mathrm{Mn^{III}}$ ions of each triplesalen unit [38], although the central phloroglucinol part of the triplesalen ligand induces ferromagnetic coupling in Cu and Mo complexes [63–65]. However, the stronger antiferromagnetic Mn-Cr coupling indicated by $J_{Mn-Cr} = -5.00\ \mathrm{cm^{-1}}$ [38, 39] enforces the spin orientation scheme shown in figure 2.2.

With the high spin ground state of $S_t = 21/2$, distinct local anisotropies D_i due to the salen-based ligand [66, 67] and a C_3 symmetric geometry avoiding mutual cancellation of the local anisotropies in the projection onto S_t [38], the $[\mathbf{Mn_6^{III}Cr^{III}}]^{3+}$ complex meets the most important requirements for the occurrence of single-molecule magnet behavior.

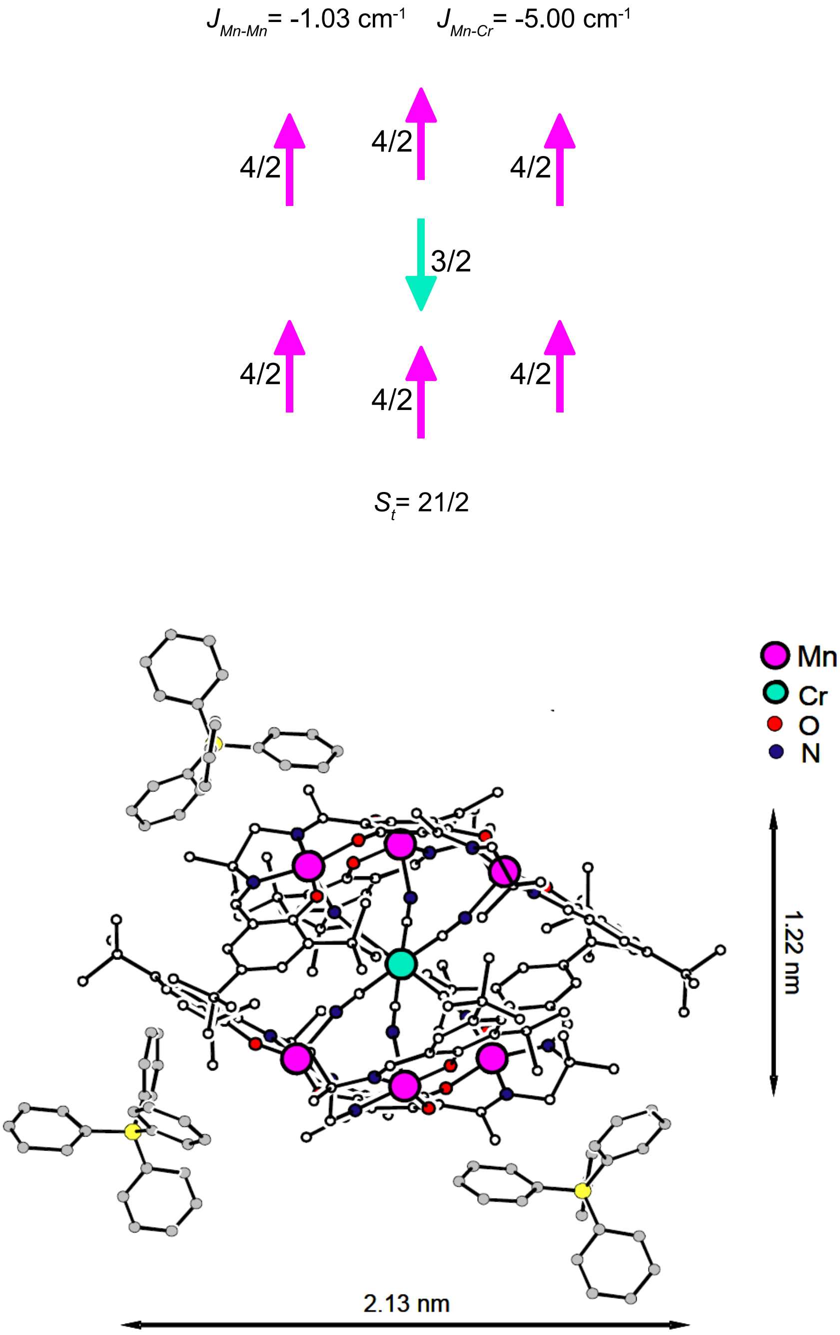

Figure 2.2. The $[\mathbf{Mn}_6^{\mathbf{III}}\mathbf{Cr}^{\mathbf{III}}]^{3+}$ single-molecule magnet. Simplified view of the $[\mathbf{Mn}_6^{\mathbf{III}}\mathbf{Cr}^{\mathbf{III}}]^{3+}$ core with the six terminal Mn$^{\mathrm{III}}$ ions and the central chromium complex. Figure adapted from [38]. Also shown are three BPh_4^- anions surrounding the $[\mathbf{Mn}_6^{\mathbf{III}}\mathbf{Cr}^{\mathbf{III}}]^{3+}$ core to ensure charge neutrality. The spin coupling scheme of the metal ions, the resulting spin ground state and the coupling constants J_{Mn-Mn} between two Mn$^{\mathrm{III}}$ ions of the same triplesalen ligand and J_{Mn-Cr} between Mn$^{\mathrm{III}}$ and Cr$^{\mathrm{III}}$ are given at the top of the figure [39].

Besides, the existence of a C_3 axis suppresses quantum tunneling as an alternative relaxation path as described in section 2.1 above. AC magnetic susceptibility data as well as single-crystal DC magnetization measurements confirm [38] the presence of single-molecule magnet behavior in $[\mathbf{Mn}_6^{\mathbf{III}}\mathbf{Cr}^{\mathbf{III}}]^{3+}$: Below 1.5 K, a distinct hysteresis loop is obtained (see figure 3 of [38]). The height of the energy barrier against spin reversal was determined to be approx. 25.4 K [38] based on the AC magnetic susceptibility measurements.

$[\mathbf{Mn}_6^{\mathbf{III}}\mathbf{Cr}^{\mathbf{III}}]^{3+}$ complexes with the different anions *tetraphenylborate* (BPh_4^-), *lactate* ($C_3H_5O_3^-$) and *perchlorate* (ClO_4^-) have been synthesized to investigate the influence of the anion choice on the $[\mathbf{Mn}_6^{\mathbf{III}}\mathbf{Cr}^{\mathbf{III}}]^{3+}$ core. A detailed description of the synthesis is given elsewhere [38, 53, 61]. Differences in the deposition behavior of the three $[\mathbf{Mn}_6^{\mathbf{III}}\mathbf{Cr}^{\mathbf{III}}]^{3+}$ complexes are described in section 3.2.1, the effect of the anion choice on the radiation stability [61] is discussed in section 5.2.

2.3. The electron spin

An approach based on electron spin polarization measurements (see section 3.4) was chosen for this work to gain insight into the magnetic properties of $[\mathbf{Mn}_6^{\mathbf{III}}\mathbf{Cr}^{\mathbf{III}}]^{3+}$ single-molecule magnets. The electron spin is an essential component of this approach, hence section 2.3.1 gives a short introduction into the properties of the electron spin and its theoretical description. Spin polarization effects in electron scattering processes and their application in electron spin polarization detectors of the Mott type will be outlined in section 2.3.2.

2.3.1. Basic considerations

The well-known experiments carried out by *Stern and Gerlach* on silver atomic beams in 1922 experimentally confirmed the existence of *space quantization* of atomic angular momenta [68, 69], but could then not be explained completely within the framework of quantum theory. A thorough review of the experiments and their interpretation is given in [70], chapters IV and VI.

However, the later interpretation of the experiments hints to the existence of an additional angular momentum: The observed splitting of the atomic beam requires the presence of a magnetic moment – this can not be attributed to the electron orbital momentum with the silver atoms (electron configuration [Kr] $4d^{10}\,5s$) being in a state now known as a $^2S_{1/2}$ ground state. The observed shape of the splitting revealed the existence of only two possible values for this angular momentum [71]. The electron spin as an intrinsic angular momentum of the electron was first postulated by *Goudsmit and Uhlenbeck* [72, 73] in 1925, interpreting the fourth quantum number introduced by Pauli [74] as an additional degree of freedom immanent to electrons.

It has to be noted that the spin angular momentum of the electron must *not* be interpreted as a mechanical rotation, as originally assumed by Goudsmit and Uhlenbeck [70, 75]. The electron spin is characterized within the framework of quantum mechanics by the spin operator S [76]. The components S_x, S_y and S_z in a Cartesian representation satisfy the commutation relations (see [76] p. 171, [77] p. 299)

$$[S_x, S_y] = i\hbar S_z \qquad [S_y, S_z] = i\hbar S_x \qquad [S_z, S_x] = i\hbar S_y, \tag{2.2}$$

which characterize an observable as an angular momentum (see [77] p. 293). As generally true for angular momenta, the operator

$$S^2 = S_x^2 + S_y^2 + S_z^2 \tag{2.3}$$

defined as the square of the spin angular momentum operator commutes with the three components S_x, S_y and S_z, allowing the simultaneous experimental observation of S^2 and S_z [77]. Using the relation [76, 78]

$$\mathbf{S} = \frac{\hbar}{2}\boldsymbol{\sigma} \quad , \tag{2.4}$$

the spin angular momentum operators can be expressed in matrix form, known as the *Pauli spin matrices* [76–78]:

$$\sigma_x = \begin{bmatrix} 0 & 1 \\ 1 & 0 \end{bmatrix} \qquad \sigma_y = \begin{bmatrix} 0 & -i \\ i & 0 \end{bmatrix} \qquad \sigma_z = \begin{bmatrix} 1 & 0 \\ 0 & -1 \end{bmatrix} \tag{2.5}$$

Restricting the situation to spin-$\frac{1}{2}$ particles (like electrons), the general state of a particle can be expressed as

$$\chi = a_1 \cdot \begin{pmatrix} 1 \\ 0 \end{pmatrix} + a_2 \cdot \begin{pmatrix} 0 \\ 1 \end{pmatrix} = \begin{pmatrix} a_1 \\ a_2 \end{pmatrix} \quad \text{(see [77] p. 308)}, \tag{2.6}$$

being a linear superposition of the two eigenvectors $\binom{1}{0}$ and $\binom{0}{1}$ corresponding to the $+\hbar/2$ and $-\hbar/2$ eigenvalues of the σ_z operator, respectively (see [76] p. 175).

An electron ensemble (e. g. an electron beam) is called *polarized* if the two orthogonal spin states with respect to a reference direction are not populated equally, see [79].

Assuming χ as normalized (which is always the case for a one-electron state), i. e. the constraint

$$|a_1^2| + |a_2^2| = 1 \tag{2.7}$$

is satisfied ([76] p. 174, [77] p. 308), the *polarization* is defined as the expectation value of $\boldsymbol{\sigma}$:

$$\mathbf{P} = \langle \chi | \boldsymbol{\sigma} | \chi \rangle \text{ (see [79], p. 9)} \tag{2.8}$$

If $\mathbf{P}$ is a pure spin state in a direction characterized by the polar angles (θ, ϕ), the Cartesian components of $\mathbf{P}$ are derived ([79] p. 10, [77] p. 311):

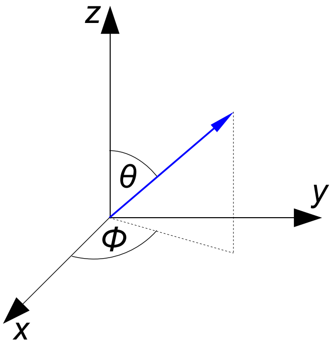

$$P_x = \sin\Theta \cos\Phi$$
$$P_y = \sin\Theta \sin\Phi \tag{2.9}$$
$$P_z = \cos\Theta$$

It has to be noted that the polarization definition of equation 2.8 needs to be modified ([79] p. 12) for a non-normalized χ (as in the case of electron ensembles),

$$\mathbf{P} = \frac{\langle \chi | \boldsymbol{\sigma} | \chi \rangle}{\langle \chi | \chi \rangle}, \tag{2.10}$$

ensuring that the magnitude of $P_{x,y,z}$ stays within the interval $[0, 1]$ under all circumstances. The physical interpretation of the quantities $|a_1|^2$ and $|a_2|^2$ yields the probabilities to find an electron in the spin-up $(+\hbar/2)$ or spin-down $(-\hbar/2)$ state when measuring the spin orientation in the z direction by means of a polarization analyzer. The polarization obtained by such a measurement

$$P = \frac{N_\uparrow - N_\downarrow}{N_\uparrow + N_\downarrow} \tag{2.11}$$

is determined from the number $N_\uparrow$ $(N_\downarrow)$ of electrons detected in the spin up (spin down) state [79].

2.3.2. Spin-dependent electron scattering: The Mott polarimeter

The Dirac equation found by *Dirac* in 1928 [77] represents a relativistic generalization of the Schrödinger equation. It is fundamental for the investigation of electron spin polarization effects, as it correctly predicts the existence of the spin-orbit interaction governing spin-dependent scattering processes ([77] p. 714 and [79] p. 30).

The differential cross section for electrons scattered in the Coulomb field of the atomic nucleus can be obtained from the Dirac equation. However, the full derivation is tedious and will not be given here, see [79] p. 20-35 for a detailed description. The scattering process of an electron from the inital pure spin state χ into the final state χ'

$$\chi = \begin{pmatrix} a_1 \\ a_2 \end{pmatrix} \qquad \longrightarrow \qquad \chi' = \begin{pmatrix} a'_1 \\ a'_2 \end{pmatrix} \tag{2.12}$$

is mathematically expressed in matrix formalism as

$$\chi' = \begin{pmatrix} S_{11} & S_{12} \\ S_{21} & S_{22} \end{pmatrix} \begin{pmatrix} a_1 \\ a_2 \end{pmatrix} = S\chi \tag{2.13}$$

with S being the scattering matrix [79]. Simple expressions are derived for the components of S,

$$\begin{aligned} S_{11}(\theta,\phi) &= \quad S_{22} = f(\theta) \\ S_{21}(\theta,\phi) &= -S_{12} = g(\theta)e^{i\phi} \end{aligned} \tag{2.14}$$

by solving the Dirac equation for incident electrons with longitudinal spin orientation ($\pm z$-direction), see [79] p. 32-35. Choosing the direction of the transverse polarization component $P_\perp$ to be the x direction (see figure 2.3), the resulting differential cross section is

$$\rho(\theta,\phi) = I(\theta)\left[1 - P_t S(\theta)\cdot\sin\phi\right] \quad \text{(see [79], p. 40)}, \tag{2.15}$$

with $I(\theta) = |f|^2 + |g|^2$ being the ϕ-independent differential cross section for an incident beam with a vanishing transverse polarization component $P_\perp$. The differential cross sections into the scattering angles $\phi = 90°$ and $\phi = 270°$ (see figure 2.3) are:

$$\rho(\theta) = \begin{cases} I(\theta)[1 - S(\theta)P_\perp] & \text{for } \phi = 90° \\ I(\theta)[1 + S(\theta)P_\perp] & \text{for } \phi = 270°. \end{cases} \tag{2.16}$$

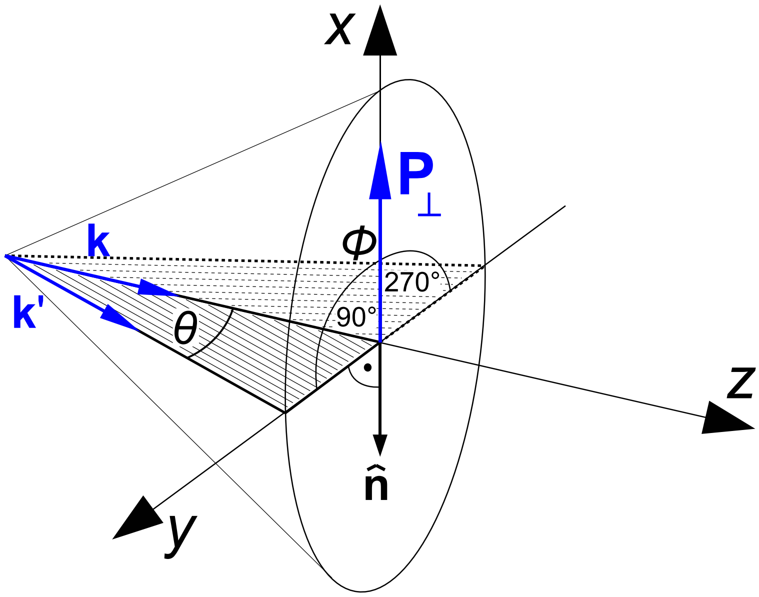

Figure 2.3. Geometry of the polarization-dependent scattering process described in the text: **k** and **k**′ represent the wave vectors of the incoming and the scattered electron wave, respectively. The scattering plane is indicated by the hatched area. The vector **n̂** is perpendicular to the scattering plane. Figure adapted from [79].

This *scattering asymmetry* is the basic physical principle applied in spin polarization detectors of the Mott type [80], like the one that was used for the spin polarization measurements in this work. The *Sherman function* [81] defined as

$$S(\theta) = i\frac{fg^* - f^*g}{|f|^2 + |g|^2} \quad \text{(see [79], p. 35)} \tag{2.17}$$

is determined by the scattering matrix elements S_{nn} (see equation 2.14), depending on the physical conditions of the actual scattering process, i. e. the electron energy and the scattering target material. It provides a means of comparing and characterizing polarization detectors based on scattering processes. A comparison of different spin polarization detectors with respect to their figure of merit

$$F = \frac{I}{I_0}S^2 \tag{2.18}$$

is given by *M. Getzlaff et al.* [82]. F depends on the Sherman function S as well as on the ratio of the scattered and incoming intensities I/I_0.

It has to be noted that the theoretical value for S is not applicable when considering a real scattering experiment due to the influence of multiple scattering processes and other effects. Therefore the polarization sensitivity or *effective Sherman function* S_{eff} is introduced, depending on the thickness of the scattering target as well as on the scattering geometry [82]. The experimentally observed scattering asymmetry between two opposite detectors in the scattering plane (seen from incoming beam direction, figure 2.3)

$$A = \frac{N_{\text{left}} - N_{\text{right}}}{N_{\text{left}} + N_{\text{right}}} \tag{2.19}$$

is related to the polarization component $P_\perp$ of the incoming electron beam [79] via the polarization sensitivity $S(\theta)$ by

$$A = \frac{1 + P_\perp S(\theta) - (1 - P_\perp S(\theta))}{1 + P_\perp S(\theta) + (1 - P_\perp S(\theta))} = P_\perp S(\theta) \quad . \tag{2.20}$$

The differential cross section can be rewritten as

$$\rho(\theta, \phi) = I(\theta)\, [1 + S(\theta)\mathbf{P} \cdot \hat{\mathbf{n}}] \tag{2.21}$$

by introducing the unit vector perpendicular to the scattering plane (hatched area in figure 2.3):

$$\hat{\mathbf{n}} = \frac{\mathbf{k} \times \mathbf{k}'}{|\mathbf{k} \times \mathbf{k}'|} \tag{2.22}$$

This expression is independent of the coordinate system chosen due to the scalar product being invariant under coordinate transformations [79].

3. Methods

3.1. Synchrotron radiation physics

The synchrotron radiation available from different electron storage ring facilities was the most crucial tool for all investigations performed on $[\mathbf{Mn_6^{III}Cr^{III}}]^{3+}$ single-molecule magnets within this thesis, making experimental methods like XAS, XMCD or SPES feasible in the first place. Therefore, a short description of the special properties of synchrotron radiation and the development of synchrotron radiation sources will be given in this section.

3.1.1. Synchrotron radiation sources

Synchrotron radiation was experimentally confirmed first in 1947 [83] at a synchrotron with an electron energy of 70 MeV operated at General Electric laboratories [84]. It had been observed indirectly before by measuring the decrease of the betatron electron orbit due to the energy loss caused by radiation emission [85], confirming calculations estimating the energy loss in betatrons [86].

The emission of synchrotron radiation is based on classical electrodynamics: An electric charge subjected to an acceleration (e. g. by a magnetic field) emits electromagnetic radiation [86]. Most relevant early works on this topic were done by *A. Liénard* [87], *E. Wiechert* [88] and *G.A. Schott* [89]. Due to relativistic effects, the emitted radiation is collimated into a narrow cone with an opening angle of $\pm 1/\gamma$ [90], with γ being the relativistic factor $\gamma = 1/\sqrt{1-\beta^2}$ and $\beta = v/c$ (see figure 3.1). Within the plane defined by the electron orbit, the radiation is completely linearly polarized in this plane. Leaving the plane, the degree of linear polarization is reduced and an increasing fraction of elliptically polarized light occurs [90].

Assuming a constant bending radius over the whole electron orbit, the total power radiated by a beam of N electrons circulating with the frequency f_{orbit} and thereby representing a current of $I = e \cdot N \cdot f_{\text{orbit}}$ can be estimated [84] as

$$P_{\text{rad}}\ (\text{MW}) = 0.088463 \cdot \frac{E^4\ (\text{GeV})}{\rho\ (\text{m})} \cdot I\ (\text{A}), \tag{3.1}$$

with E being the electron energy and ρ the bending radius of the electron orbit. The E^4 dependence of the radiated power represents a severe limitation for the final energy attainable in circular particle accelerators.

First synchrotron radiation experiments were performed in parasitic mode on large synchrotrons designed for high-energy and nuclear physics (see [91] for various examples), usually operating in cycles of injection, acceleration and extraction with high repetition rates, imposing practical limitations on synchrotron radiation experiments. Storage rings are able to overcome these limitations by keeping the electrons on (approximately) circular orbits on the timescale of several hours after injection and acceleration. Upon reaching the nominal energy, the accelerator RF cavity is used to reaccelerate the circulating electrons in order to compensate for the energy loss due to synchrotron radiation. In 1968, the first electron storage ring was operated as a dedicated synchrotron radiation source [92], marking the beginning of a whole era of dedicated synchrotron radiation facilities.

Besides the synchrotron radiation emitted from bending magnets along the storage ring, later third generation synchrotron facilities use *insertion devices* (undulators, wigglers) installed in the straight sections of the storage ring between bending (dipole) magnets. They consist of periodic permanent magnet arrays (see figure 3.2) or (often superconducting) magnet coils to modulate the electron orbit and create radiation with higher intensity and smaller emittance. The theory behind undulators and wigglers was first developed by *Ginzburg* in 1947 [93]. By introducing a longitudinal shift between the split magnet assemblies of a so-called planar elliptical undulator, different polarization modes can be achieved (see [94] and figure 3.2). Thereby a parallel shift of the indicated magnet rows by $\lambda/4$ achieves circular polarization by forcing the electrons on a helical trajectory, an antiparallel shift of $\lambda/2$ results in linear polarization in the vertical plane.

Synchrotron radiation emitted in a bending magnet exhibits a broad spectral width extending from the infrared region up to hard X-rays, see fig. 3 in ref. [95]. The radiated intensity drops sharply beyond a critical energy ϵ_{crit}, although higher photon energies still contribute to the synchrotron radiation spectrum. A simple approximation [96] yields

$$\epsilon_{\text{crit}}\ (\text{eV}) = 2218 \frac{E^3\ (\text{GeV})}{\rho\ (\text{m})} \tag{3.2}$$

with E being the electron energy in GeV and ρ the bending radius in m. In contrast to bending magnet sources, undulators emit a narrow spectrum around a fundamental wavelength defined as [84, 90]

$$\lambda = \frac{\lambda_p}{2\gamma^2}(1 + \frac{K^2}{2}) \tag{3.3}$$

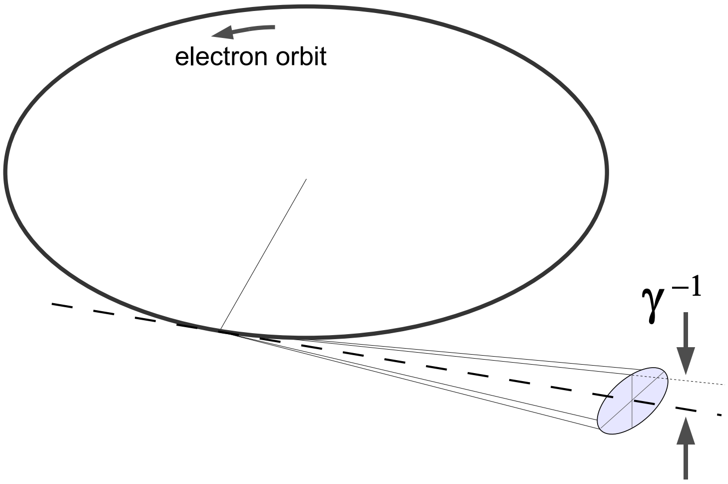

Figure 3.1. Synchrotron radiation emission geometry: The synchrotron radiation emitted by an accelerated electron moving in a circular orbit is focused into a narrow cone within the plane of the electron orbit. The opening angle is determined by the relativistic factor γ due to the relativistic nature of the electron motion.

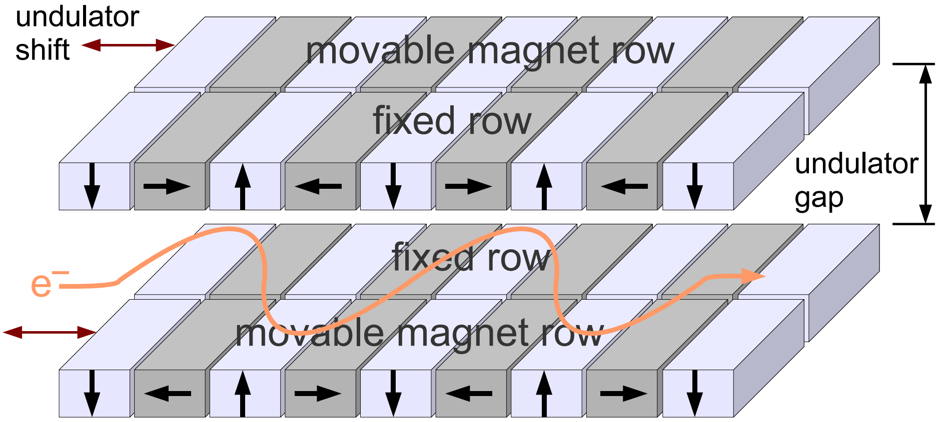

Figure 3.2. The magnetic field created by the magnet rows of an APPLE-II type undulator superimposes an oscillatory transversal component on the electron momentum, leading to the emission of synchrotron radiation in each 'bend'. The emitted wavelength depends on the magnetic field strength, which can be adjusted by changing the undulator gap. A horizontal shift of two magnet rows allows to change the polarization of the emitted synchrotron radiation.

with γ defined as before and λ_p the period length of the undulator. The bandwidth $1/N_p$ [84] of the undulator radiation is determined by the number of magnet periods N_p. K denotes the so-called *undulator parameter* [84]

$$K \approx 0.934 B_0\ (\mathrm{T}) \cdot \lambda_p\ (\mathrm{cm}), \tag{3.4}$$

which depends on the magnetic field strength B_0 of the undulator poles and the undulator period λ_p.

Higher harmonics of the undulator fundamental also occur and represent usable undulator operation modes with different spectral characteristics. As the wavelength of the undulator fundamental (and the harmonics) depends on the magnetic field strength, the emitted spectrum can be shifted to different energies by changing the magnetic field. In permanent magnet undulators as used in most synchrotron radiation facilities, this is done by changing the distance (gap) between the magnet rows (see figure 3.2). Due to the narrow spectrum emitted by an undulator source, the selection of a specific wavelength in an undulator beamline is performed by moving the undulator gap as well as the monochromator grating.

With their high intensity, continuously variable wavelength over a very broad spectral range extending from the far infrared to hard X-rays, and the variable polarization properties of the emitted radiation, synchrotron sources represent a unique light source for scientific work. For the results presented within this thesis, the capability of synchrotron sources to emit circularly polarized radiation of variable wavelength with a high degree of polarization in the soft X-ray range was essential, as there are no laboratory X-ray sources with comparable properties available.

3.1.2. Overview of the synchrotron beamlines used within this work

The results presented within this work have been obtained using different synchrotron radiation beamlines at the facilities *BESSY II* (HZB Berlin, Germany), *MAX-II* (MAX-lab Lund, Sweden) and *SLS* (PSI Villigen, Switzerland). A short overview of the different beamlines and their specifications will be given in this section. The most relevant parameters of all beamlines used are summarized in table 3.1.

Beamline UE52-SGM at BESSY II Berlin

A large part of the spin-resolved measurements has been carried out at the BESSY II undulator beamline UE52-SGM. It utilizes the synchrotron radiation provided by a permanent magnet

beamline	**source type**	**flux** ($\frac{\text{photons}}{\text{s}\cdot\text{100mA}}$)	**spot size** (μm)	**ref.**
BESSY II UE52-SGM	undulator	10^{11}	20 × [exit slit]	[97]
BESSY II UE56/2-PGM2	undulator	$2\cdot10^{11}$	900 × 20-200	[98]
MAX-lab D1011	dipole	10^{10}	1000 × 1000	[99]
SLS X11MA-SIM	undulator	$2\cdot10^{15}$	100 × 30	[100]

Table 3.1. Basic parameters of the synchrotron radiation beamlines used to perform the measurements presented within this work. The given spot sizes (horizontal × vertical) are nominal values that do not necessarily correspond to the spot size used, the latter depending on the position of the apparatus/sample as well as on the exit slit setting. Photon fluxes are nominal values in the relevant 600-700 eV range. For the X11MA beamline, this flux figure has been significantly reduced by increasing the c_{ff} value of the monochromator and inserting an additional aluminium filter.

undulator of the APPLE-II type [94, 101, 102]. The UE52 undulator features 77 magnet periods with a period length of 52 mm [103]. By shifting two of the four magnet rows accordingly, synchrotron radiation of variable polarization (linear, elliptic/circular) can be obtained. The circular polarization mode of the undulator was used for the spin polarization measurements shown in sections 5.4 and 5.5. The usable range of photon energies delivered by the UE52-SGM beamline is approx. 90 eV to 1500 eV with an energy resolution better than 4000 [97].

The UE52-SGM beamline is based on a spherical grating monochromator with three different gratings (900, 1200 and 1500 lines/mm). The incoming radiation is vertically demagnified (17:2.5) [97] onto the entrance slit by a cylindrical mirror. Afterwards, the entrance slit is imaged onto the exit slit by the spherical grating. A cylindrical mirror vertically refocuses the radiation.

In the horizontal plane, focusing is performed by a plane elliptical mirror in the last chamber of the beamline, leading to a spot size of approx. 20 μm (horizontal) [97]. The vertical spot size is determined by the exit slit setting. For our experiments, an off-focus position was chosen for the sample: Due to the beam divergence of 6 mrad (h) by 1 mrad (v) [97], the spot size changes with the distance from the focal point. A spot size of approx. 1 mm^2 was selected by adjusting the UHV apparatus to the appropriate distance.

Using the 3rd harmonic of the UE52 undulator and a 1200 lines/mm monochromator grating, a photon flux of approx 10^{11} photons/s/100mA reached the sample at an exit slit setting of 20 μm, see figure 3.3. During XAS characterization measurements, this flux was significantly reduced by closing a set of baffles in the beamline front-end and using the minimum reproducible exit slit setting of 0.5 μm.

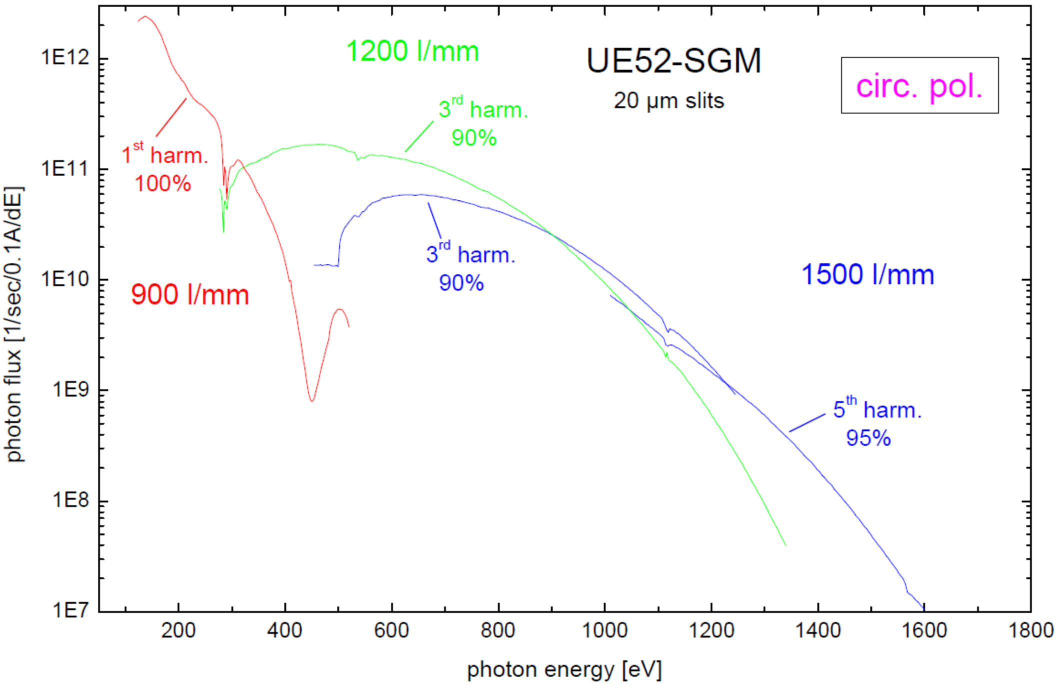

Figure 3.3. The relation between photon energy and resulting photon flux for different undulator harmonics and monochromator gratings at beamline UE52-SGM of the BESSY II synchrotron facility. Figure taken from [104].

Beamline UE56/2-PGM2 at BESSY II Berlin

The UE56/2-PGM-2 beamline at BESSY II is based on a double undulator of the APPLE-II type with a period length of 56 mm and 31 periods in each section. A small angular offset between the synchrotron radiation beams exiting the two undulators allows fast switching between them via a chopper assembly in the post-monochromator beamline optics [105]. The available range of photon energies extends from approx. 90 eV up to 1300 eV. A monochromator resolution of up to 90000 can be achieved at 64 eV photon energy [98].

The synchrotron radiation from the beamline front-end is horizontally focused on the sample position by a toroidal mirror. In the vertical plane, the mirror creates a collimated beam entering the SX-700 type [106, 107] plane grating monochromator. A second mirror deflects the light onto one of two different gratings with 400 lines/mm and 1200 lines/mm. Afterwards, a cylindrical mirror focuses the radiation vertically onto the exit slit. Behind the exit slit, the monochromatized synchrotron radiation is vertically focused onto the sample position by a conical mirror, leading to a final spot size of 900 μm (h) by 20-200 μm (v), depending on the exit slit setting [98, 105]. The available photon flux at the sample position is approx. $2 \cdot 10^{11}$ ph./s/100mA [98]. The baffles in the beamline front-end were used to reduce the photon flux for the XAS characterizations as described for the UE52-SGM beamline before.

Beamline D1011 at MAX-lab Lund

The D1011 soft X-ray beamline at the MAX-II storage ring of the MAX-lab facility in Lund was used for the investigation of the $[\mathbf{Mn_6^{III}Cr^{III}}]^{3+}$ radiation stability and various influences on the condition of the deposited SMM, see sections 5.1 and 5.2. Being a dipole-magnet beamline, D1011 delivers a significantly lower photon flux than undulator beamlines, allowing a detailed study of radiation-dependent effects for the $[\mathbf{Mn_6^{III}Cr^{III}}](BPh_4)_3$ and $[\mathbf{Mn_6^{III}Cr^{III}}](C_3H_5O_3)_3$ SMM despite their high radiation sensitivity.

The beamline uses the synchrotron radiation delivered by a 4.7 mrad bending magnet and covers a usable range of photon energies from 40 eV up to 1500 eV with an energy resolution of 1500 – 13000 [99]. A cylindrical mirror as the first optical element of the beamline horizontally focuses the radiation onto the monochromator exit slit. After the first mirror, the light enters the SX-700 type [106, 108] planar grating monochromator. It is then directed at the 1200 lines/mm planar grating by a plane mirror and afterwards focused onto the monochromator exit slit in the vertical plane by a plane elliptical mirror. As there are no refocusing optics between the exit slit and the first experimental chamber, the radiation is divergent at the sample position with a spot size of approx. 2 mm by 1 mm [99]. During the measurements presented within this work, the spot size was reduced to approx. 1 mm^2 by using a set of baffles further upstream in the beamline.

The flux delivered to the sample for different settings of the monochromator exit slit is shown in figure 3.4. The 6 μm slit setting was used for the radiation damage studies, leading to a photon flux of approx. 10^{10} photons/s reaching the sample at 100 mA ring current. Note that this flux is half the value given in figure 3.4 due to the use of the beamline baffles.

Beamline SIM at PSI Villigen

The XMCD studies of $[\mathbf{Mn_6^{III}Cr^{III}}](ClO_4)_3$ single-molecule magnets have been performed at the X11MA-SIM beamline at the Swiss Light Source (PSI Villigen). The beamline uses the light produced by a set of two permanent magnet undulators with a period length of 56 mm and 64 periods each, comparable to the UE56 undulators operated at BESSY II. Both undulators can be operated with opposite polarization or helicity, allowing fast polarization switching by a chopper system in the beamline optics [100]. The available photon energy range extends from 90 eV up to 2000 eV with an energy resolution better than 5000 [100].

The synchrotron radiation of the undulator is collimated before entering the SX-700 type [106, 108] planar grating monochromator (300 lines/mm or 1200 lines/mm). Afterwards, it is focused onto the exit slit in the vertical plane. Horizontally, the light focus is located on the chopper unit to allow selection of the different polarizations emitted by both undulators. A refocusing mirror images the exit slit onto the sample position, leading to a final spot size of 100 μm (h) by 30 μm (v) [100].

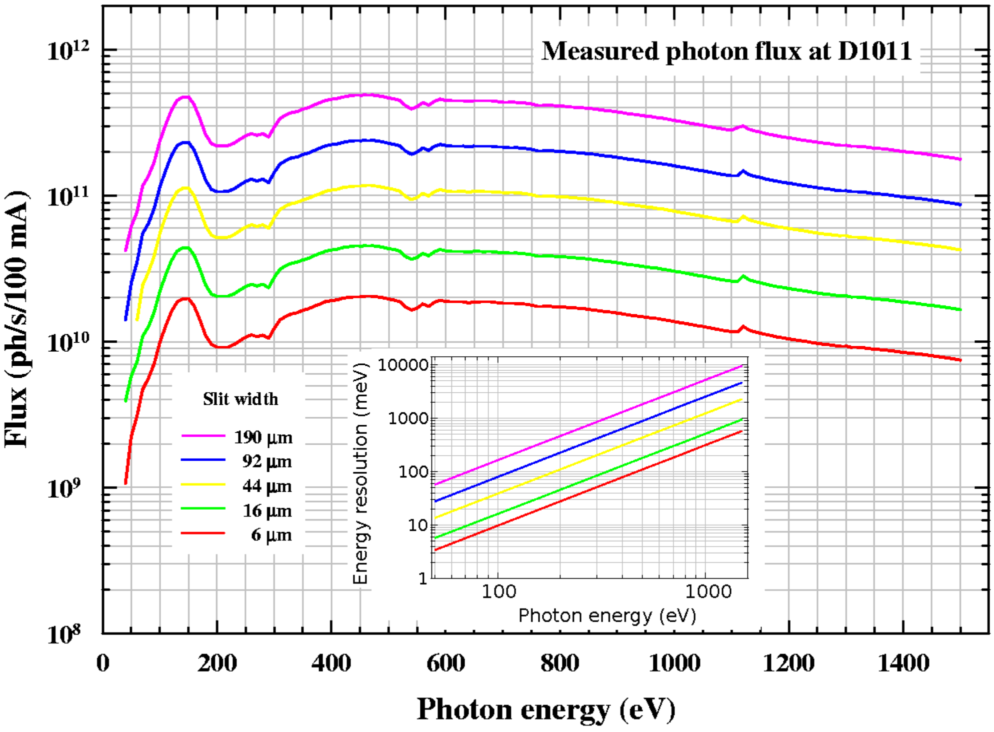

Figure 3.4. The relation between photon energy, monochromator exit slit width and the resulting photon flux for beamline D1011 at MAX-lab, Lund. Flux data are normalized to a ring current of 100 mA. The energy resolution depending on the photon energy is shown in the inset [99].

The nominal photon flux of 10^{15} photons/s/400mA was significantly reduced for the investigation of $[\mathbf{Mn}_6^{\mathbf{III}}\mathbf{Cr}^{\mathbf{III}}]^{3+}$ by tuning the monochromator to a high fix-focus constant

$$c_{\mathrm{ff}} = \frac{sin\alpha}{sin\beta} \simeq 20 \qquad (\alpha, \beta\text{: grating incident and exit angle}) \tag{3.5}$$

instead of the usual value of $c_{\mathrm{ff}} = 2.25$. Increasing c_{ff} leads to a higher spectral resolution and a decreased photon flux due to the lower grating efficiency [107]. An additional aluminium filter was inserted into the photon beam. The XMCD data have been obtained using the XMCD apparatus of the IPCMS Strasbourg, providing a magnetic field of ±6.9 T at a sample temperature of approx. 2 K.

3.2. Sample preparation

The $[\mathbf{Mn}_6^{\mathbf{III}}\mathbf{Cr}^{\mathbf{III}}]^{3+}$ SMM synthesized in the group of Prof. T. Glaser (Faculty of Chemistry, Bielefeld University) were deposited onto substrates in order to perform the measurements described within this thesis. Although the synthesis of the investigated $[\mathbf{Mn}_6^{\mathbf{III}}\mathbf{Cr}^{\mathbf{III}}]^{3+}$ substances yields macroscopic crystals (see figure 3.5 left), these are extremely sensitive to mechanical stress, making it impossible to handle or mount single crystals in a sample holder. Furthermore, the insulating properties of the bulk $[\mathbf{Mn}_{\mathbf{6}}^{\mathbf{III}}\mathbf{Cr}^{\mathbf{III}}]^{3+}$ make sample current based absorption spectroscopy as well as electron spectroscopy almost impossible due to charging effects, enforcing the use of thin $[\mathbf{Mn}_{\mathbf{6}}^{\mathbf{III}}\mathbf{Cr}^{\mathbf{III}}]^{3+}$ layers on conductive substrates.

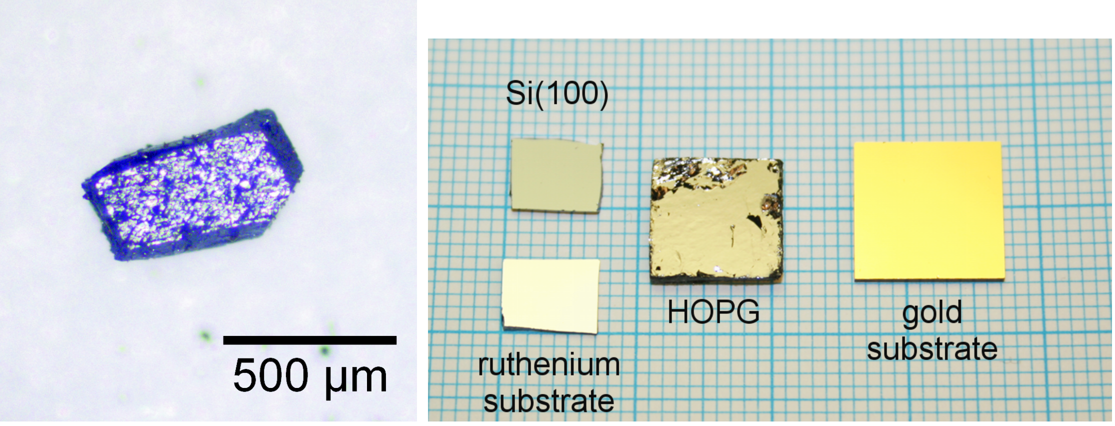

Figure 3.5. Left: Microscope image of $[\mathbf{Mn}_{\mathbf{6}}^{\mathbf{III}}\mathbf{Cr}^{\mathbf{III}}](C_3H_5O_3)_3$ crystallite as obtained from the synthesis. Right: The different substrate materials used for the $[\mathbf{Mn}_{\mathbf{6}}^{\mathbf{III}}\mathbf{Cr}^{\mathbf{III}}]^{3+}$ preparation within this work.

Different metallic substrates as well SiO and HOPG were used for both preparation methods described below (see figure 3.5 right). The substrates were square with an edge length of 5.5 ± 1 mm up to 8 ± 1 mm for the drop-casting method and 11 ± 1 mm for the airbrush preparation. The HOPG [109], gold [110] and silicon [111] substrates were commercially available, the ruthenium substrates were prepared by sputter deposition in the group of Prof. G. Reiss, Bielefeld University [112]. The basic properties of all substrates used for the preparation of $[\mathbf{Mn}_{\mathbf{6}}^{\mathbf{III}}\mathbf{Cr}^{\mathbf{III}}]^{3+}$ samples are summarized in table 3.2.

3.2.1. Drop-casting

Prior to the drop-casting preparation, the crystalline $[\mathbf{Mn}_{\mathbf{6}}^{\mathbf{III}}\mathbf{Cr}^{\mathbf{III}}]^{3+}$ powders were dissolved in methanol. The concentration of the resulting SMM solutions was $4.5{\cdot}10^{-4}$ mol/l. A droplet of approx. 10 μl of the SMM solution was then placed on a horizontally oriented substrate by using an adjustable μl-capable pipette. Microcrystallites began to form in the solution covering the substrate during solvent evaporation, leading to the formation of a granular $[\mathbf{Mn}_{\mathbf{6}}^{\mathbf{III}}\mathbf{Cr}^{\mathbf{III}}](ClO_4)_3$ deposit on the substrate surface. AFM investigation (see figure 3.6) revealed particle heights between 250 nm and 3000 nm with a large fraction of the microcrystallites being in the (500 ± 250) nm height range. The total area coverage calculated from the AFM data shown in the inset of figure 3.6 was approx. 30% [61].

substrate	composition	source, reference
gold	250 ± 50 nm Au 2.5 ± 1.5 nm Cr 0.7 ± 0.1 mm borosilicate glass	'Arrandee' [110]
ruthenium	50 nm Ru 10 nm Ta 0.5 mm Si(001)	AG Reiss [112]
silicon	Si(100), n-doted (phosphorus), thickness 525 μm	MaTeck GmbH [111]
HOPG	type ZYB, 10·10·1.2 mm^3 mosaic spread 0.2-1.2 deg	Anfatec Instruments AG [109]

Table 3.2. Composition and basic properties of the substrates used for the $[\mathbf{Mn_6^{III}Cr^{III}}]^{3+}$ preparation.

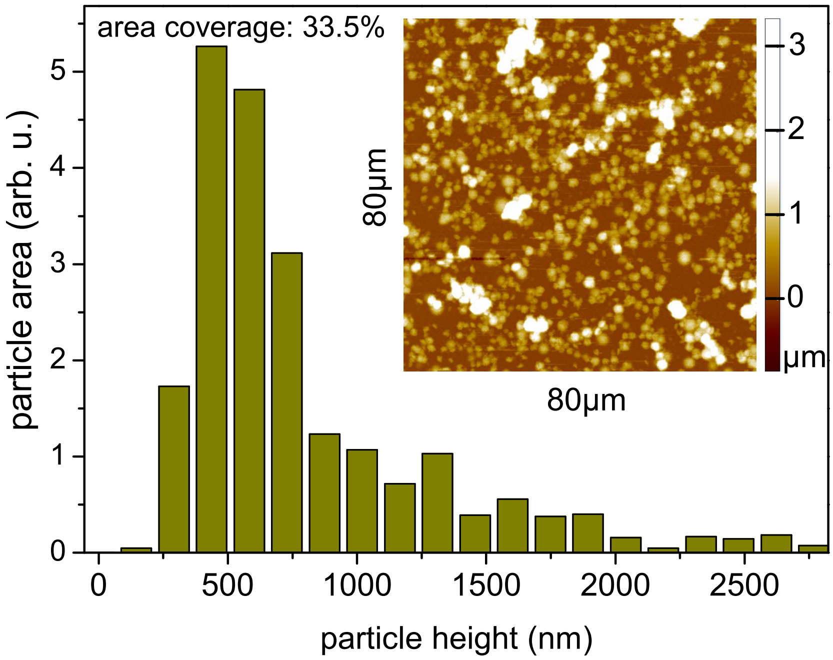

Figure 3.6. AFM characterization of a $[\mathbf{Mn_6^{III}Cr^{III}}](ClO_4)_3$ sample prepared by drop-casting. The height distribution of the microcrystallites forming on the substrate surface upon solvent evaporation is given. Inset: The height distribution was determined from the 80μm by 80μm section of the sample shown in this AFM micrograph. Image taken from [61].

A closed deposit layer with a few irregular aggregations of microcrystallites forms upon solvent evaporation in the case of $\mathbf{[Mn_6^{III}Cr^{III}]}(BPh_4)_3$. Particle sizes are comparable to the results obtained from $\mathbf{[Mn_6^{III}Cr^{III}]}(ClO_4)_3$ [61], although the total abundance of microcrystallites on the sample surface is much lower and most of them are found at the sample edges.

A remarkably different wetting behavior is found for the methanol solution of the SMM with lactace anions $\mathbf{[Mn_6^{III}Cr^{III}]}(C_3H_5O_3)_3$: No microcrystallite formation could be observed, the sample surface is covered with a plain deposit layer without any discernible structures. An amount of 5 μl of the $\mathbf{[Mn_6^{III}Cr^{III}]}(C_3H_5O_3)_3$ solution was sufficient to form a complete deposit layer [61].

Another remarkable feature of the $\mathbf{[Mn_6^{III}Cr^{III}]}(C_3H_5O_3)_3$ deposition was the formation of self-supporting membrane-like structures (see figure 3.7 left) on small circular metal grids available for transmission electron microscopy (400 mesh, supplier: Plano, see [113]). Drop-casting preparation on TEM grid substrates was carried out as described before, while keeping the TEM grid in self-closing tweezers to avoid contact between the solution droplet and the surface below the grid.

Scanning electron microscopy revealed a distinct, brushstroke-like substructure in the self-supporting membranes spanning over the meshes of the TEM grids (see figure 3.7). Most of the membranes seem to be cracked in the central part, possibly due to mechanical stress during solvent evaporation and membrane formation. It has to be noted that a higher $\mathbf{[Mn_6^{III}Cr^{III}]}(C_3H_5O_3)_3$ concentration results in membranes appearing more massive in optical microscopy and not showing any signs of cracking.

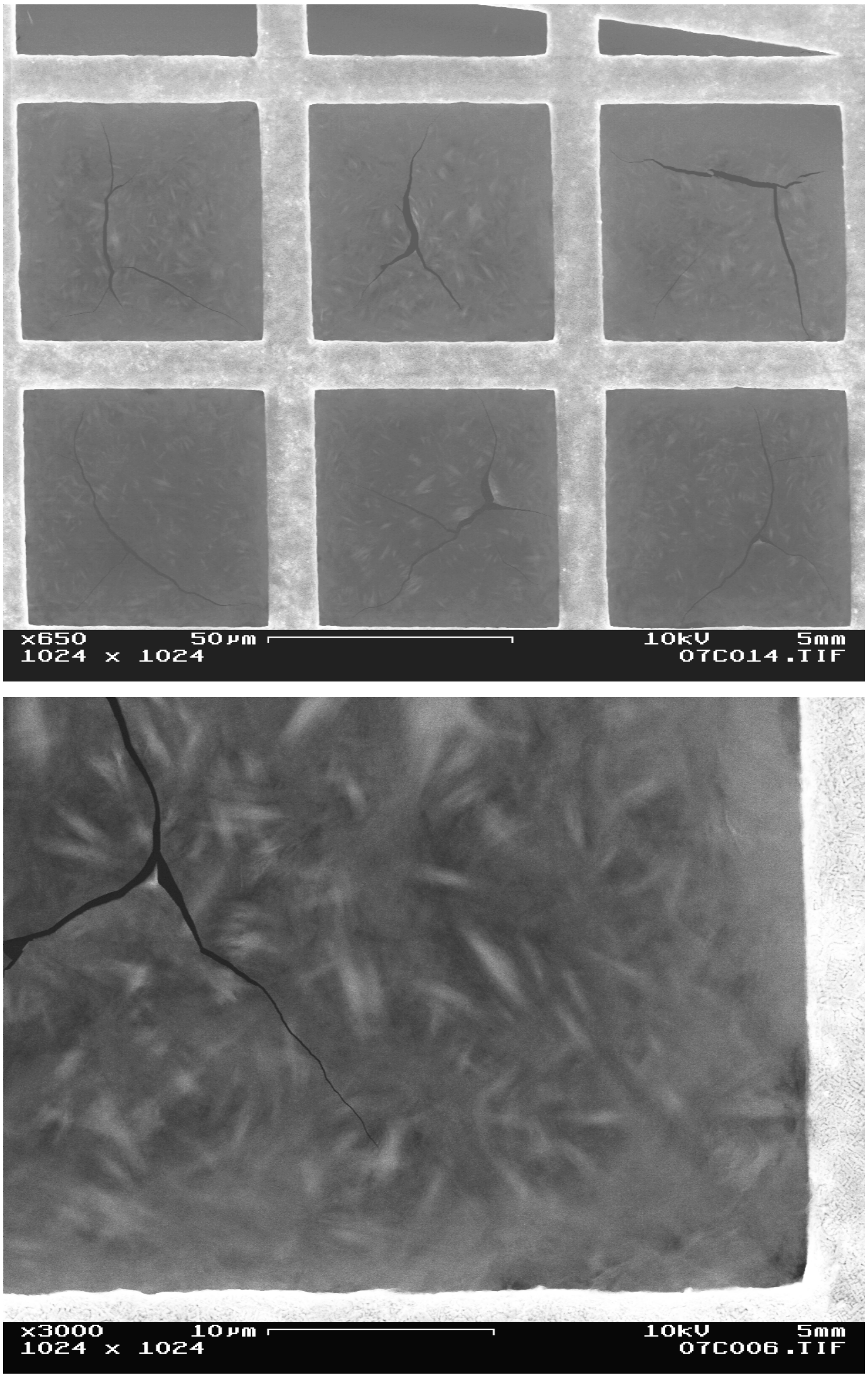

Figure 3.7. Scanning electron microscopy images of the membranes formed on TEM grids by $[\mathbf{Mn_6^{III}Cr^{III}}](C_3H_5O_3)_3$. Top panel: Overview showing several TEM grid meshes with the $[\mathbf{Mn_6^{III}Cr^{III}}](C_3H_5O_3)_3$ membranes. Bottom panel: Detailed image of the upper middle mesh showing the characteristic brushstroke-like substructure.

3.2.2. Airbrush method

The sensitivity of the investigated $[\mathbf{Mn_6^{III}Cr^{III}}]^{3+}$ SMM against exposure to soft X-rays on one hand (see section 5.2) and the need for either a high photon flux or comparatively long integration times in order to apply spin-resolved electron spectroscopy on the other hand presented one of the main challenges within this work. These conflicting requirements were met by the introduction of sample scanning: During SPES data acquisition, the radiation exposure of each position on the $[\mathbf{Mn_6^{III}Cr^{III}}]^{3+}$ sample was limited to an acceptable dose (remaining Mn^{III} content ≥ 0.8) and the data obtained from different positions on the sample were accumulated.

The application of sample scanning required $[\mathbf{Mn_6^{III}Cr^{III}}]^{3+}$ samples showing comparable signal intensities as well as an identical $[\mathbf{Mn_6^{III}Cr^{III}}]^{3+}$ molecule condition over large areas of approx. 100 mm^2. These requirements regarding sample homogeneity could not be met by the drop-casting method mentioned before, leading to the development of a preparation method investigated and optimized by N. Dohmeier in the context of his diploma thesis. It is based on a commercially available precision airbrush tool (model: Grafo T1, see [114]).

The basic principle of this preparation method (see figure 3.8 left) can be summarized as follows: The airbrush tool equipped with a nozzle of 150 μm bore diameter was operated using high-purity nitrogen at a pressure of approx. 1.5 bar. A $[\mathbf{Mn_6^{III}Cr^{III}}](ClO_4)_3$ solution with a concentration of $9 \cdot 10^{-5}$ mol/l was used for the preparation. Approx. 200 μl of the SMM

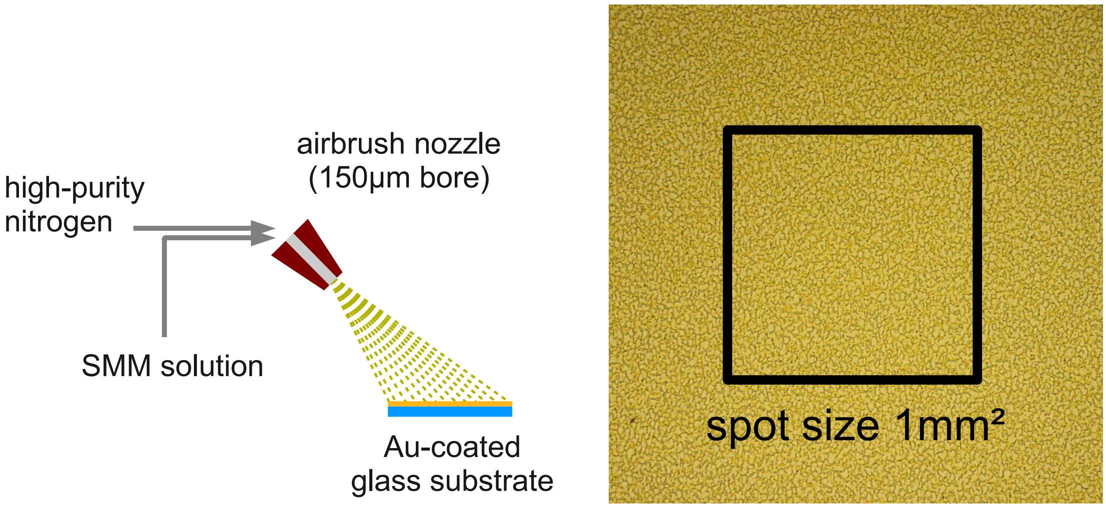

Figure 3.8. Left: Schematic representation of the airbrush preparation method. Right: Optical microscopy image of a $[\mathbf{Mn_6^{III}Cr^{III}}](ClO_4)_3$ sample prepared by airbrush technique. The black square represents the approx. synchrotron radiation beam cross section used. For an overview of the complete sample, see figure 5.3 right.

solution were sprayed onto the substrate, repeatedly scanning the airbrush nozzle over the substrate in a regular pattern at a distance of approx. 40 mm from the substrate. Irregularities of the spraying due to changes in distance or scanning speed are averaged out in the process, leading to a deposited $[\mathbf{Mn_6^{III}Cr^{III}}](ClO_4)_3$ film with homogeneous appearance over large scales.

Optical microscopy of samples prepared by the airbrush method (see figure 3.8 right) reveals a $[\mathbf{Mn_6^{III}Cr^{III}}]^{3+}$ deposition behavior with a lot of small, labyrinth-like irregularities. However, on length scales above 0.2 mm the deposit appears homogeneous, even over a sample area of approx. 100 mm^2 (see figure 5.3, right for comparison). Given the typical synchrotron radiation spot size of approx. 1 mm^2 used within this work, the small irregularities seen in optical microscopy will be averaged out during a measurement.

3.3. X-ray absorption spectroscopy and magnetic circular dichroism

X-ray absorption spectroscopy in the soft X-ray regime ($L_{2,3}$ edge XAS) provides an important tool to characterize $[\mathbf{Mn_6^{III}Cr^{III}}]^{3+}$ samples with respect to the oxidation state of the metal constituents, giving insight into radiation-induced reduction processes (see section 5.2) as well as into preparation-related changes of the $[\mathbf{Mn_6^{III}Cr^{III}}]^{3+}$ sample condition. The closely related XMCD technique using circularly polarized synchrotron radiation is capable of providing element-specific information about the local magnetic moments of the metal constituents in $[\mathbf{Mn_6^{III}Cr^{III}}]^{3+}$. Both methods and their underlying principles will be introduced in this section.

3.3.1. Introduction to XAS

Photons in the soft X-ray range (250 eV up to 10 keV, see figure 1.1 of [115]) carry sufficient energy to ionize electrons from atomic core states. The binding energy of these core states is highly element-specific (see [116–119]). Absorption spectra obtained by varying the incident photon energy and measuring the absorption (see figure 3.10) therefore represent an element-specific tool, giving access to the elemental composition as well as to information about the chemical environment of selected atoms, such as the oxidation state [120–126].

The overall structure of the absorption spectrum with its characteristic edge structures corresponding to the binding energies of atomic core states is depicted schematically in figure 3.10. For transition metals, these edges exhibit prominent absorption peaks, the so-called

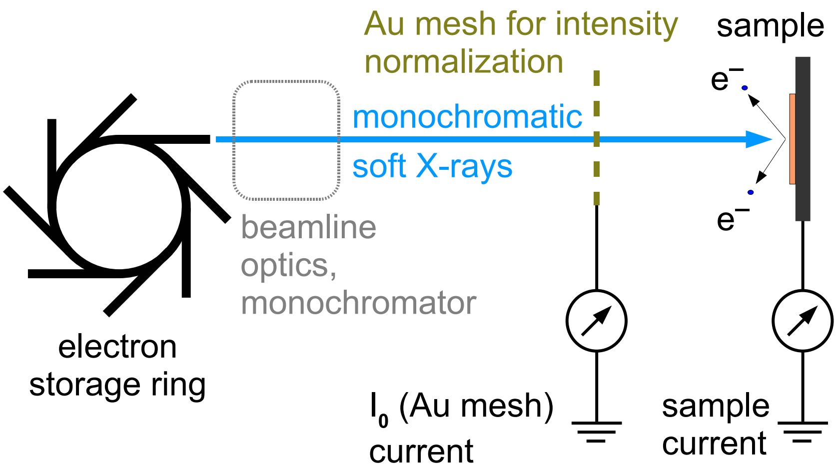

Figure 3.9. Experimental setup for absorption spectroscopy (XAS): Monochromatized synchrotron radiation generated in a storage ring is monochromatized and focussed onto the sample. The radiation excites electrons from core states, depending on the photon energy. The current flowing to the sample is a direct measurement of the number of electrons ejected (total electron yield mode). The current generated in a gold mesh is used for intensity normalization purposes.

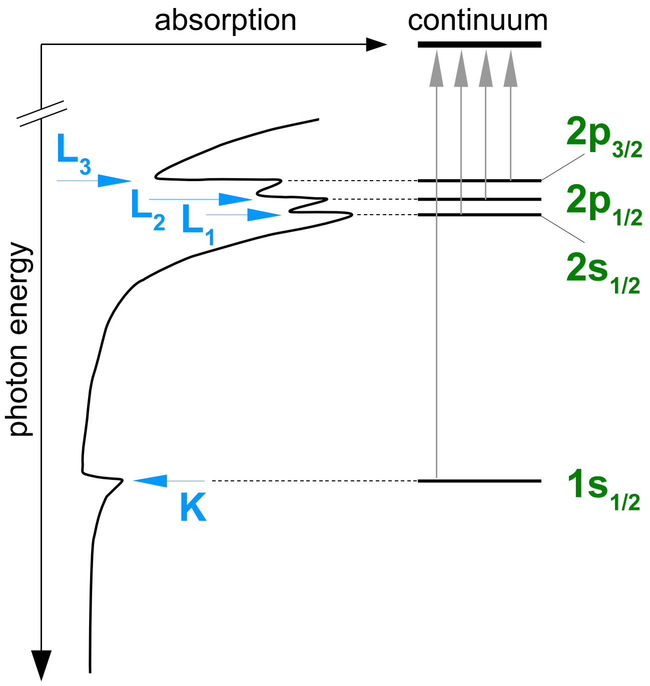

Figure 3.10. Simplified sketch depicting the characteristic structure of X-ray absorption vs. photon energy spectra. The correlation between the distinct edges in the X-ray absorption and the corresponding core states excited by the X-ray photons is shown.

white lines [127]. Resonant absorption into the large density of empty $3d$ states is the main reason for the existence of these absorption features in $3d$ transition metals like Mn [128]. Note that the core states in figure 3.10 are given in a truncated form of the most common notation (see [129]) for the description of atomic states

$$nX_J\,, \tag{3.6}$$

where n is the principal quantum number, X denotes the orbital momentum by a letter (s, p, d, f, ... corresponding to $L = 1,2,3,4,...$) and J gives the total angular momentum. Besides, the *X-ray notation* is used to denote absorption edges: Depending on its principal quantum number, a letter (K, L, M, ... corresponding to $n = 1,2,3,...$) is assigned to each absorption edge, accompanied by a subscript number denoting the subshell [119].

According to *Fermi's Golden Rule* the probability W for a transition from the initial state Φ_i to the final state Φ_f is given by the expression (see [130])

$$W = \frac{2\pi}{\hbar} |\langle\Phi_f| T |\Phi_i\rangle|^2 \delta_{E_f - E_i - \hbar\omega} \tag{3.7}$$

with T being the transition operator. Limiting the picture to one-photon transitions, the first order transition operator T_1 can be expressed as the first term of the interaction Hamiltonian [130]

$$T_1 = H_1 = \frac{e}{mc}\mathbf{p}\cdot\mathbf{A} \tag{3.8}$$

with $\mathbf{p}$ the electron momentum operator and $\mathbf{A} = \frac{1}{2}\hat{\mathbf{e}}_q A_0 e^{i(kx-wt)}$ the vector field of the incident plane electromagnetic wave [130]. Following the derivation given in [130], neglecting all higher order contributions and taking only electric dipole transitions into account leads to the so-called *dipole approximation* of the transition operator:

$$T_1 = \sum_q (\hat{\mathbf{e}}_q \cdot \mathbf{r}) \tag{3.9}$$

Thereby $\mathbf{r}$ denotes the position operator and $\hat{\mathbf{e}}_q$ represents a unit vector in the polarization direction q of the incident wave. The transition probability can then be rewritten as

$$W \propto \sum_q |\langle\Phi_f| \hat{\mathbf{e}}_q \cdot \mathfrak{r} |\Phi_i\rangle|^2 \delta_{E_f - E_i - \hbar\omega} \qquad \text{(see [130])} \tag{3.10}$$

The transition matrix element $|\langle\Phi_f|\hat{\mathbf{e}}_q \cdot \mathbf{r}|\Phi_i\rangle|^2 = M^2$ can be assumed to be approximately constant with energy, thus the absorption signal I_{XAS} probes the density ρ of empty final states [130]:

$$I_{\mathrm{XAS}} \sim M^2 \cdot \rho \tag{3.11}$$

The basic detection principle for X-ray absorption is based on the comparison of the incident and transmitted photon flux I_0 and I_{trans} by X-ray detectors, giving a direct measure of the linear absorption coefficient μ [131] as

$$\mu x = ln\left(\frac{I_0}{I_{\mathrm{trans}}}\right), \tag{3.12}$$

with x being the sample thickness. The detection of X-ray fluorescence resulting from the decay of the primary core hole created in the absorption process represents another method of measuring the X-ray absorption [132, 133]. However, in the soft X-ray regime ($E_{h\nu} < 1$ keV) the X-ray attenuation length is less than 1 μm [130], which complicates direct transmission measurements by requiring very thin samples [134]. Besides, the fluorescence yield decreases significantly [130, 131] in favor of Auger processes dominating the decay of the core hole.

A very common experimental approach [130, 135] to obtain I_{XAS} in the soft X-ray regime is based on the proportionality between absorption cross section and photoelectric yield, i. e. the total number of photoelectrons, Auger electrons and secondary electrons leaving the sample upon irradiation. This proportionality has been described first by Gudat *et al.* in 1972 [136]. The measurement principle is shown in figure 3.9: The synchrotron radiation produced by an electron storage ring is monochromatized and hits the sample. Depending on the selected photon energy, photoelectrons are ejected from the sample upon absorption. The sample current replacing these electrons represents a direct measurement of the total number of electrons emitted by the sample. This mode of operation is called *total-electron-yield* (TEY) mode. As the intensity of the synchrotron radiation varies with energy and storage ring current, the photocurrent of a transparent gold mesh in front of the sample is used to provide an intensity normalization of the absorption signal. A direct detection of the photoelectrons ejected from the sample is possible by using electron detectors instead of measuring the sample current. An energy discrimination is introduced by retarding potentials to select only electrons with a kinetic energy above a given threshold [137, 138]. This measuring mode is usually named *partial-electron-yield* (PEY).

All detection methods depending on electron yield measurements are highly surface sensitive due to the stronger interaction of excited electrons within the sample compared to X-ray photons, leading to a material-dependent probing depth of 3-10 nm in the soft X-ray range [130]. The high absorption cross section of rare earths and transition metals at transition edges leads to absorption lengths [139] and probing depths shorter than expected [134, 135] from the universal curve [140].

3.3.2. XMCD and sum rules

The **X**-ray **M**agnetic **C**ircular **D**ichroism effect being the fundamental principle behind the correspondent XMCD method was described theoretically in 1975 [141]. It has been shown experimentally first on iron by Schütz *et al.* in 1987 [142] using hard X-rays to probe the iron K-edge region. The first application to the $L_{2,3}$ edge of $3d$ transition metals has been done by Chen *et al.* in 1990 [143] using a Ni sample.

The experimental approach is comparable to the X-ray absorption spectroscopy method described in section 3.3.1 (see figure 3.11). The application of circularly polarized radiation and the use of magnetized samples leads to differences in the obtained X-ray absorption spectra depending on the relative orientation of the light helicity and the sample magnetization. Information on the local spin and orbital magnetic moments of the sample can be gathered from these differences in absorption using the sum rule formalism described later.

Exposure to circularly polarized X-rays induces core-valence transitions that are governed by the relativistic dipole selection rules [144]:

$$\Delta j = 0, \pm 1 \qquad \Delta l = \pm 1 \qquad \begin{array}{ll} \Delta m_j = +1 & \text{(positive helicity)} \\ \Delta m_j = -1 & \text{(negative helicity)} \end{array}$$

The XMCD effect observed in $3d$ transition metals can be explained by a 'two step model' (see [145, 146]). As circularly polarized radiation is used, the photon carries an angular momentum that is transferred to the excited core electron due to the presence of spin-orbit coupling, leading to the creation of oriented $2p$ core holes and spin-polarized photoelectrons (see [145, 147, 148]) in the first step. This has been theoretically described by N. A. Cherepkov in 1979 [149].

Looking at the $2p_{3/2} \rightarrow 3d$ (L_3 edge) and $2p_{1/2} \rightarrow 3d$ (L_2 edge) transitions relevant for the measurements presented here, the application of the selection rules limits the available excitation channels to the $\Delta m_j = +1$ transitions as shown in figure 3.12, if radiation of positive helicity is used in the excitation step. The relative transition probabilities for both $2p_{1/2}$ and $2p_{3/2}$ excitations are also given in figure 3.12. It has to be noted that these have been calculated using a non-relativistic approximation [150].

The resulting core hole polarization for the $p_{3/2} \rightarrow d$ transition is obtained [151] using the individual transition probabilities a_i and the spin polarization s_i of each initial channel calculated from the Clebsch-Gordan coefficients [150]:

$$\begin{aligned} \mathbf{P} = \sum a_i s_i &= (0.045 \cdot (-1)) + (0.03 \cdot (-1)) + (0.135 \cdot (-\frac{1}{3})) \\ &\quad + (0.04 \cdot (-\frac{1}{3}) + (0.27 \cdot \frac{1}{3}) + (0.03 \cdot \frac{1}{3}) + (0.45 \cdot 1) \\ &= \mathbf{0.417} \end{aligned} \tag{3.13}$$

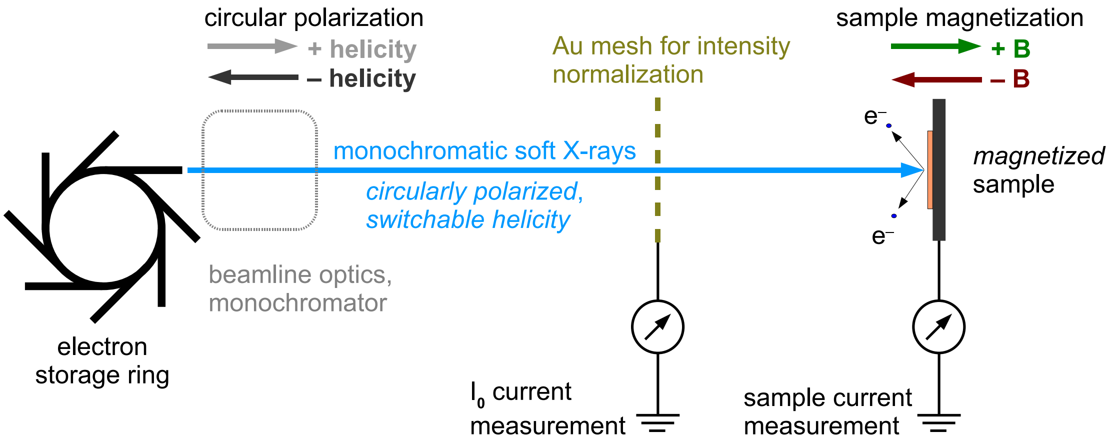

Figure 3.11. Experimental setup for XMCD measurements. The basic principle is similar to XAS (see figure 3.9). XMCD measurements require the use of circularly polarized X-rays and magnetically oriented samples. The XMCD asymmetry can be obtained by either switching the helicity of the light or the orientation of the field (parallel vs. anti-parallel to the light helicity).

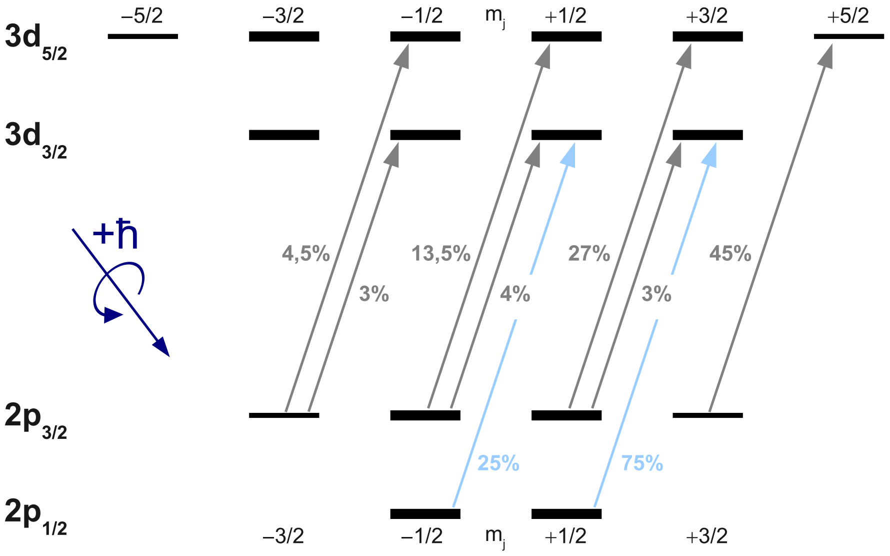

Figure 3.12. Transition scheme for $2p \rightarrow 3d$ transitions using circularly polarized light of positive helicity. Only $\Delta m_j = +1$ transitions are allowed due to the relativistic dipole selection rules. Relative excitation probabilities calculated in a non-relativistic approximation are given [150]. Thin bars denote pure spin states. Figure adapted from [150].

An overview of the mixed $2p$ ($m_j = \pm 1/2$) and $3d$ ($m_j = \pm 1/2, \pm 3/2$) m_j-states and their corresponding Clebsch-Gordan coefficients is given in appendix A.

In a second step, the magnetically oriented $3d$ states perform as a spin detector: Assuming a magnetized sample with the magnetization *parallel* to the photon **k** vector, the majority spin orientation is *anti-parallel* to the magnetization direction (spin down). Therefore the empty $3d$ states available as final states for the $2p_{3/2} \rightarrow 3d$ transition are preferentially oriented parallel to the magnetization (spin up), leading to a difference in the transition probabilities for X-rays with positive and negative helicity. With the magnetization parallel to the incoming beam, a higher absorption is seen for positive helicity light. The situation is reversed for the L_2 edge ($2p_{1/2}$ core states) due to the opposite sign of the spin orbit coupling [146].

The second step of the simple model often used to describe XMCD [146, 152, 153] influences the absorption yields σ^+ (σ^-) for light of positive (negative) helicity via the empty state densities $\rho^\uparrow$ ($\rho^\downarrow$) for the two spin directions parallel (anti-parallel) to the k vector of the radiation [152]:

$$\sigma^+ = f(\alpha^\uparrow \rho^\uparrow + \alpha^\downarrow \rho^\downarrow) \qquad \text{positive helicity light} \tag{3.14}$$

$$\sigma^- = f(\beta^\uparrow \rho^\uparrow + \beta^\downarrow \rho^\downarrow) \qquad \text{negative helicity light} \tag{3.15}$$

Thereby $\alpha^\uparrow$ ($\alpha^\downarrow$) represents the probability to excite a spin-up (spin-down) photoelectron in the primary excitation step with positive helicity light. The correspondent probabilities for negative helicity light are given by $\beta^\uparrow$ and $\beta^\downarrow$. Note the equalities

$$\alpha^\uparrow = \beta^\downarrow \qquad \alpha^\downarrow = \beta^\uparrow \tag{3.16}$$

are valid [152], resulting in the fact that reversal of the magnetic field direction (and thereby reversing the minority/majority spin population) is equivalent to switching the light helicity and yields the same XMCD result.

The difference in the absorption yields normalized by the total absorption is known as the XMCD asymmetry

$$A_{\text{XMCD}} = \frac{Y^+ - Y^-}{Y^+ + Y^-} \quad , \tag{3.17}$$

where Y^+ (Y^-) denotes the absorption yield with the light helicity parallel (anti-parallel) to the sample magnetization.

It has to be noted that the commonly used simplified XMCD picture [146, 152, 153] has severe limitations. Within the more detailed configuration picture, an atom is excited from an initial state configuration into a final state configuration, with the spin-orbit splitting of the p shell not being an initial state effect [145]. Equivalency between configuration picture and one-electron model exists merely for d^9 ground state configurations [154]. The often used graphical representation of the XMCD effect [146, 153, 155] depicts the $p_{3/2}$, $p_{1/2}$ sublevels as pure spin states, which is not the case [150–152]. Moreover, the spin-orbit splitting in the final $3d$ states is often neglected, taking only the predominant exchange splitting in magnetic materials into account.

A wide field of practical applications for the XMCD method was opened by the so-called *sum rules* proposed by Thole *et al.* [156] in 1992 for the orbital magnetic moment and Carra *et al.* [157] in 1993 for the spin magnetic moment. These sum rules relate the difference in absorption yields $Y^+ - Y^-$ to the local spin and orbital magnetic moments of the sampled atom, thereby allowing the element-specific determination of magnetic moments within the sample. Defining the integrals

$$p = \int_{L_3} \left(Y^+ - Y^-\right) dE \qquad \text{L}_3 \text{ edge XMCD signal} \tag{3.18}$$

$$q = \int_{L_{3,2}} \left(Y^+ - Y^-\right) dE \qquad \text{L}_{3,2} \text{ edge XMCD signal} \tag{3.19}$$

$$r = \int_{L_{3,2}} \frac{1}{2} \left(Y^+ + Y^-\right) dE \qquad \text{L}_{3,2} \text{ edge averaged absorption} \tag{3.20}$$

the sum rules for the orbital magnetic moment μ_{orbit} and the spin magnetic moment μ_{spin} can be expressed as follows [146, 158]:

$$\mu_{\text{orbit}} = -\frac{2 \cdot q \cdot (10 - n_{3d})}{3r} \tag{3.21}$$

$$\mu_{\text{spin}} + 7 < T_z > = -\frac{(3p - 2q) \cdot (10 - n_{3d})}{r} \tag{3.22}$$

In these expressions, n_{3d} represents the number of $3d$ holes available as final states. $< T_z >$ denotes the magnetic dipole operator, see [146] for a more detailed description. Due to the approximations used to derive the above equalities, the practical use of the sum rules for the determination of magnetic moments is subject to a number of limitations that will be discussed in the following section.

3.3.3. Limitations of the sum rule approach for 3d transition metals

Being based on a single-ion approach [156], the sum rule formalism as described above is based on a number of assumptions and simplifications, limiting the accuracy of the determined spin and orbital magnetic moments [159–163]:

- It is assumed that **no hybridization** between shells occurs and therefore l represents a good quantum number [160].

- **Only dipole transitions** $p \rightarrow d$ are taken into account, transitions into s final states are neglected [146, 162].

- The **radial matrix elements** R_d, R_s for d and s states are assumed to be **energy-independent** and constant for all transitions [159, 162]. It has been shown for Ni surfaces that these matrix elements vary linearly with the photon energy and change by approx. 30% across the d band. While this influence cancels out in the orbital momentum sum rule, it represents a problem for the applicability of the spin sum rule [162].

- In solid state systems, the **number of d holes N_h is not always well defined [159].**

- The **magnetic dipole contribution $<T_z>$** is often regarded as zero. In fact, $<T_z>$ is only negligible in the presence of cubic symmetry [160]. However, for 3d transition metals, the influence has been shown to be small by Teramura *et al.* [164].

The orbital sum rule is reported to be accurate to approx. 10% [159], mainly suffering from deviations due to the neglection of $s, p-d$ hybridization effects in the derivation of the sum rule. Hybridization of different l shells represents the main limitation of the spin sum rule for transition metals, leading to large deviations [160].

For both sum rules, the spin-orbit splitting of the core levels needs to be significantly larger than other interactions, such as the core-valence Coulomb interaction. The $2p-3d$ Coulomb interaction is non-negligible for 3d transition metals and severely limits the significance of the spin sum rule due to deviations up to 30% [164].

Calculations performed by Teramura *et al.* [164] yield correction factors for the application of the spin sum rule to 3d transition metals. However, manganese ions of the $\mathrm{Mn^{II}}$ and $\mathrm{Mn^{III}}$ oxidation state give rise to additional difficulties associated with the non-negligible overlap of the L_2, L_3 regions. No correction at all is provided for $\mathrm{Mn^{III}}$ [164] due to the strong mixing of the $2p_{1/2}$ and $2p_{3/2}$ contributions. A comparison of spin sum rule results with ab-initio calculations [165] generally disputes the applicability of the spin sum rule for $3d^4$ systems like $\mathrm{Mn^{III}}$ due to the large discrepancies obtained from the calculations.

However, Piamonteze *et al.* [166] suggest an approach to correct sum rule results by simulating the experimental data using multiplet calculations and derive the sum rule error from a comparison between theoretical expectation values of $<T_z>$ and $<S_z>$ and the sum rule value obtained from the simulated spectra. This method has been successfully applied to manganese ions in $3d^4$ configuration in magnetites by Küpper *et al.*, see [167]. The correction factor obtained by the described method has been applied to our results obtained from $\mathbf{[Mn_6^{III}Cr^{III}]}^{3+}$. The manganese ions in $\mathbf{[Mn_6^{III}Cr^{III}]}^{3+}$ are of the same $3d^4$ configuration, though embedded in a different environment, thus the derived correction gives a better estimate of the spin magnetic moment than the uncorrected sum rule result.

3.4. Electron Spectroscopy

Spin-resolved electron spectroscopy was the most crucial scientific tool with respect to the main subject of this work, the spin polarization data obtained from reference materials as well as from $\mathbf{[Mn_6^{III}Cr^{III}]}^{3+}$ single-molecule magnets, presented in sections 5.4 and 5.5, respectively. The details of the experimental setup will be described in chapter 4 and various details concerning the applicability of the method and the interpretation of the data are explained along with the results in chapter 5. The basic principles behind this electron spectroscopy method will be outlined here.

Electron **S**pectroscopy for **C**hemical **A**nalysis is a well established, highly versatile X-ray based characterization method today, a comprehensive review of the field including its historical development can be found in [168]. Outstanding contributions to the development of this method have originated in the Swedish group of K. Siegbahn (see [169, 170]), where high resolution magnetic and electrostatic spectrometers were developed for electron spectroscopy use. The 1981 Nobel Prize in Physics was awarded to K. Siegbahn in honor of his achievements concerning the development of electron spectroscopy as a scientific tool [171].

The element specificity of atomic core states already mentioned in section 3.3.1 is one reason for the chemical sensitivity of ESCA [172]. Beyond the mere information on electron binding energies, the existence of so-called *chemical shifts* in these binding energies depending on the oxidation state of the emitting atom as well as on its chemical surrounding [168] is crucial for the versatility of ESCA for chemical characterization, which has been thoroughly investigated by Siegbahn's group [169, 170].

3.4.1. Theoretical aspects of electron spectroscopy

The theoretical description of the processes taking place upon the absorption of an X-ray photon and the subsequent excitation of an electron from an atomic core state into an unoccupied shallow valence state or into the continuum has been outlined in section 3.3.1, leading to the final expression of the transition probability W given in equation 3.10.

In the simplified *sudden approximation* [140, 168] it is assumed that the final state $|\Phi_f\rangle$ of equation 3.10 decouples into independent contributions for the ejected photoelectron and the remaining $N-1$ electron system - any interaction taking place after the absorption process is neglected [140]. The sudden approximation holds well for high kinetic energies and free atoms or molecules [168]. Energy losses [173, 174] due to inelastic scattering of the photoelectrons moving to the surface of the solid have to be taken into consideration when investigating solid state systems.

The commonly used *three-step model* of photoemission [175] regards the photoemission process as a sequence of three events, the **primary excitation** step, the **electron transport** through the solid to the sample surface and finally the **emission** of the photoelectron from the surface into the vacuum [117].

In this model the energy distribution $I(E,\omega)$ of the photoelectrons ejected from the sample with an energy E upon the absorption of radiation having the energy $\hbar\omega$ consists of electrons which did not take part in any inelastic processes and an additional background of electrons that lost energy due to scattering [117]:

$$I(E,\omega) = \underbrace{I_0(E,\omega)}_{\substack{\text{non-scattered}\\\text{electrons}}} + \underbrace{I_s(E,\omega)}_{\substack{\text{electrons with}\\\text{energy loss due to}\\\text{scattering}}} \tag{3.23}$$

The distribution of primarily excited photoelectrons $PE(E,\omega)$ is modified by two functions describing the transmission through the solid ($T(E)$) and the escape into the vacuum at the surface ($D(E)$) (see [117]):

$$I_0(E,\omega) = PE(E,\omega) \times T(E) \times D(E) \tag{3.24}$$

Assuming that the scattering probability is related to the existence of an energy-dependent mean free path length for electrons $l_e(E)$, the transmission function $T(E)$ can be expressed as

$$T(E) = \frac{l_e(E)/\lambda(\omega)}{1 + l_e(E)/\lambda(\omega)} \qquad \text{(see [117, 175])}, \tag{3.25}$$

with $\lambda(\omega)$ being the attenuation length for a photon of the energy $\hbar\omega$. Only electrons having sufficient kinetic energy normal to the surface to overcome the potential barrier $V = E_F + \Phi$ consisting of the Fermi energy E_F and the work function Φ [176] are capable of leaving the surface, leading to the expression

$$D(E) = \frac{1}{2}\left[1 - \left(\frac{V}{E}\right)^{\frac{1}{2}}\right] \qquad \text{for } E > V = E_F + \Phi$$
$$= 0 \qquad \text{otherwise} \tag{3.26}$$

for the aforementioned escape function $D(E)$ [117, 177]. Both functions $T(E)$ and $D(E)$ are assumed to vary only slowly with the energy E, thus they may change the photoelectron distribution, but are not expected to cause structures in $I_0(E, \omega)$ [117].

3.4.2. Application to $[\mathbf{Mn}_6^{\mathrm{III}}\mathbf{Cr}^{\mathrm{III}}]^{3+}$: Spin-resolved electron spectroscopy

Following the more general introduction to electron spectroscopy above, this paragraph gives an outline of the practical application with respect to the investigation of $[\mathbf{Mn}_6^{\mathrm{III}}\mathbf{Cr}^{\mathrm{III}}]^{3+}$ SMM being the main topic of this work.

Auger processes (see figure 3.13) represent the predominant decay channel for the core hole created in the primary excitation [130] in the soft X-ray regime below 1 keV. The results presented in sections 5.4 and 5.5 are based on this fact, using the $L_{2,3}M_{2,3}V$ Auger decay as a means of detecting the primary core hole spin orientation after excitation with circularly polarized light. The two electrons involved in the Auger decay exhibit a predominant singlet coupling (see page 82), leading to the fact that the core hole orientation is reflected in the Auger electron polarization. A detailed discussion of the role of this Auger channel for the spin-resolved electron spectroscopy results is given in sections 5.3 and 5.4.1.

The energy of the ejected $L_{2,3}M_{2,3}V$ electrons is analyzed by an electrostatic spherical-field spectrometer, see section 4.1. Overviews of various electrostatic energy analyzer concepts

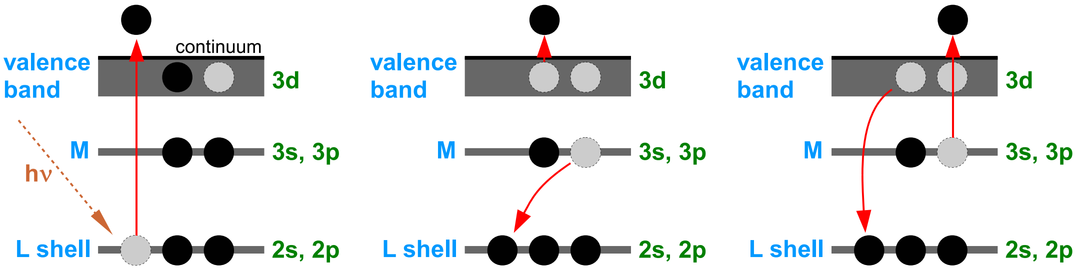

Figure 3.13. Principle of Auger decay: An L shell electron is excited by the absorption of an X-ray photon (left). The resulting core hole is filled by an M shell (valence) electron, releasing sufficient energy to eject a valence (M shell) electron into the vacuum, see middle (right). Note that the two possible decay paths shown in the middle and right image lead to the ejection of an Auger electron of the same energy, i. e. they cannot be distinguished by electron spectroscopy.

can be found in [178, 179]. In addition to the energy analysis, the spin polarization of the Auger electrons is measured. A Mott polarimeter based on the physical principle described in section 2.3.2 performs the spin analysis, see section 4.1 for a detailed description of the Mott polarimeter and the electron detectors used within this work.

Other detection principles based on spin-dependent effects in low-energy electron diffraction (LEED) exist, see [180]. Devices based on magnetized iron films have been developed recently [181, 182], reaching polarization sensitivities of up to 30% with a reflected/scattered intensity of approx. 10% [182]. A comparison of different spin polarization measurement methods with regard to polarization sensitivity and efficiency is given in [82].

A non-zero spin polarization of the electron beam entering the Mott polarimeter leads to an asymmetry between the counts N_2 and N_4 recorded in the two detectors. The spin polarization P of the electron beam can be obtained [82, 183] from

$$P \cdot S_{\mathrm{eff}} = \frac{\sqrt{N_2^+ N_4^-} - \sqrt{N_2^- N_4^+}}{\sqrt{N_2^+ N_4^-} + \sqrt{N_2^- N_4^+}} \,, \tag{3.27}$$

using circularly polarized light of both helicities to eliminate inherent asymmetries (electron beam path, geometry, see [183]) of the apparatus. Thereby $N_2^\pm$ and $N_4^\pm$ represent the detected counts in electron detector 2 and 4 for positive and negative helicity of the light used for the excitation, respectively. The polarization sensitivity S_{eff} of the spin detector has been explained before, see section 2.3.2. Introducing the parameter

$$Q = \sqrt{\frac{\frac{N_2^+}{N_4^+}}{\frac{N_2^-}{N_4^-}}} = \sqrt{\frac{N_2^+ \cdot N_4^-}{N_4^+ \cdot N_2^-}} \,, \tag{3.28}$$

the spin polarization expression given in equation 3.27 can be rewritten as a function of Q:

$$P \cdot S_{\mathrm{eff}} = \frac{\sqrt{N_2^+ N_4^-} - \sqrt{N_2^- N_4^+}}{\sqrt{N_2^+ N_4^-} + \sqrt{N_2^- N_4^+}} = \frac{Q-1}{Q+1} \tag{3.29}$$

The error introduced into Q via the statistical uncertainties $\Delta N_{2,4}^\pm = \sqrt{N_{2,4}^\pm}$ of the count rates $N_{2,4}^\pm$ can be derived using the Gaussian law of error propagation [184, 185]:

$$\Delta Q = \sqrt{\underbrace{\left(\frac{\partial Q}{\partial N_2^+}\Delta N_2^+\right)^2}_{a} + \underbrace{\left(\frac{\partial Q}{\partial N_4^-}\Delta N_4^-\right)^2}_{b} + \underbrace{\left(\frac{\partial Q}{\partial N_4^+}\Delta N_4^+\right)^2}_{c} + \underbrace{\left(\frac{\partial Q}{\partial N_2^-}\Delta N_2^-\right)^2}_{d}} \tag{3.30}$$

With the rearranged evaluations

$$a = \left(\frac{N_4^- \cdot \sqrt{N_2^+}}{2\sqrt{\frac{N_2^+ N_4^-}{N_4^+ N_2^-}} N_4^+ N_2^-} \right)^2 = \frac{N_4^-}{4 N_4^+ N_2^-}$$

$$b = \left(\frac{N_2^+ \cdot \sqrt{N_4^-}}{2\sqrt{\frac{N_2^+ N_4^-}{N_4^+ N_2^-}} N_4^+ N_2^-} \right)^2 = \frac{N_2^+}{4 N_4^+ N_2^-}$$

$$c = \left(\frac{N_2^+ N_4^- \cdot \sqrt{N_4^+}}{2\sqrt{\frac{N_2^+ N_4^-}{N_4^+ N_2^-}} \left(N_4^+\right)^2 N_2^-} \right)^2 = \frac{N_2^+ N_4^-}{4 \left(N_4^+\right)^2 N_2^-}$$

$$d = \left(\frac{N_2^+ N_4^- \cdot \sqrt{N_2^-}}{2\sqrt{\frac{N_2^+ N_4^-}{N_4^+ N_2^-}} N_4^+ \left(N_2^-\right)^2} \right)^2 = \frac{N_2^+ N_4^-}{4 N_4^+ \left(N_2^-\right)^2}$$

for the expressions *a*, *b*, *c* and *d* within the square root of equation (3.30) a simple expression for the statistical error of the parameter Q is obtained:

$$\begin{aligned} \Delta Q &= \sqrt{\frac{1}{4} \cdot \frac{N_2^+ N_4^-}{N_4^+ N_2^-} \left(\frac{1}{N_2^+} + \frac{1}{N_4^-} + \frac{1}{N_4^+} + \frac{1}{N_2^-} \right)} \\ &= \frac{1}{2} \cdot Q \cdot \sqrt{\frac{1}{N_2^+} + \frac{1}{N_4^-} + \frac{1}{N_4^+} + \frac{1}{N_2^-}} \qquad (3.31) \end{aligned}$$

This result leads to an expression of the total statistical error of the measured spin polarization by applying the law of error propagation to equation 3.28:

$$\Delta(S_{eff} \cdot P) = \frac{Q}{(Q+1)^2} \cdot \sqrt{\frac{1}{N_2^+} + \frac{1}{N_4^-} + \frac{1}{N_4^+} + \frac{1}{N_2^-}} \qquad (3.32)$$

The expressions given in equations 3.28 and 3.32 have been applied to obtain the spin polarization results and the statistical errors shown in sections 5.4 and 5.5. The uncertainty of the Mott polarimeter sensitivity ΔS_{eff} (see section 4.1) has also been considered.

4. Experimental Setup

A mobile UHV apparatus which could be taken to synchrotron radiation facilities under vacuum conditions without subsequent baking was designed and built up for the SPES measurements presented in this work. Its main components are the measurement chamber with the electron spectrometer and the Mott detector needed for spin analysis, a preparation chamber with sample storage and preparation facilities and a load-lock assembly to transfer samples from atmospheric to UHV conditions.

All main components are mounted to a rectangular frame made of aluminium profiles (90 mm by 90 mm square cross section) with the dimensions 900 mm (in beam direction) by 1500 mm (perpendicular to the beam) and a height of 550 mm. The frame carrying the vacuum components is connected to a larger base frame (1120 mm by 1800 mm). Height adjustment in a range of 125 mm is provided by four variable posts carrying the base frame.

A set of three orthogonal Helmholtz coil pairs wound on a cubic frame with an edge length of 1.20 m surrounds the measurement chamber and electron spectrometer, providing a compensation of the earth's magnetic field to a residual field of normally less than 5 μT.

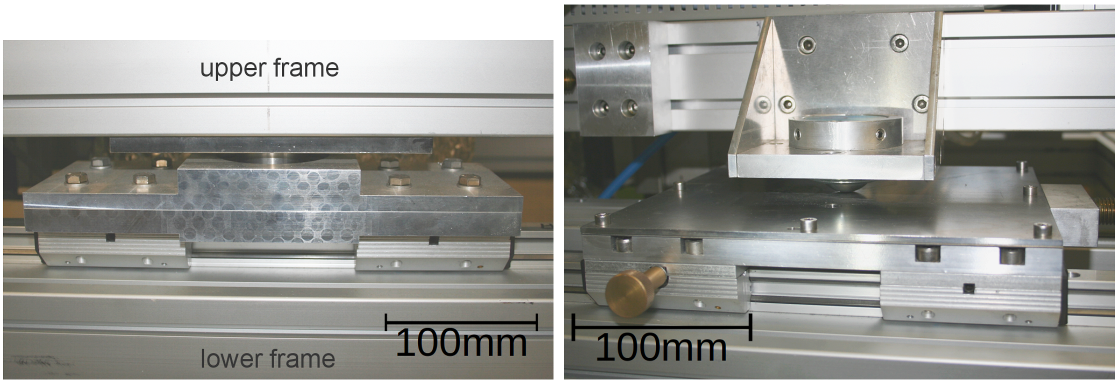

Figure 4.1. The adjustment mechanism used to align the UHV system to the synchrotron radiation beam axis. Left: The self-aligning roller bearing supports the front of the upper frame. Note the linear guide connecting the bearing to the base frame. Right: Ball casters carrying the weight of the UHV system without restricting the rotary motion of the roller bearing.

The magnitude of the residual fields is strongly correlated with the magnetism of the surrounding components like UHV valves and pumps. The required current in the field coils is determined by means of a flux gate magnetometer which is moved around the measuring chamber while adjusting the coil current.

The connection between the upper frame with the UHV system and the base frame is made by a specially designed adjustment mechanism: A large self-aligning roller bearing allows the rotation of the whole upper frame assembly around a vertical axis through the light entrance of the electron spectrometer (see figure 4.1 left). Two stainless steel ball casters on the back end of the upper frame provide mechanical support for the weight of the apparatus without limiting the rotary motion of the adjustment mechanism (see figure 4.1 right).

The roller bearing as well as the stainless steel base plates for the ball casters are mounted on horizontal linear guides oriented perpendicular to the axis of the incoming synchrotron light beam, thereby providing another degree of freedom of the adjustment mechanism: Besides the rotation around the light entrance point, the whole UHV apparatus can be moved perpendicular to the beam axis. This allows a fast and easy three-dimensional alignment of the apparatus to the synchrotron radiation beam along with the height adjustment of the base frame.

The main components of the UHV apparatus will be described in more detail in the following sections, along with a short discussion of the vacuum design and requirements. A schematic overview is given in figure 4.2, images of the UHV apparatus installed at BESSY-II beamline UE52-SGM are shown in appendix B.

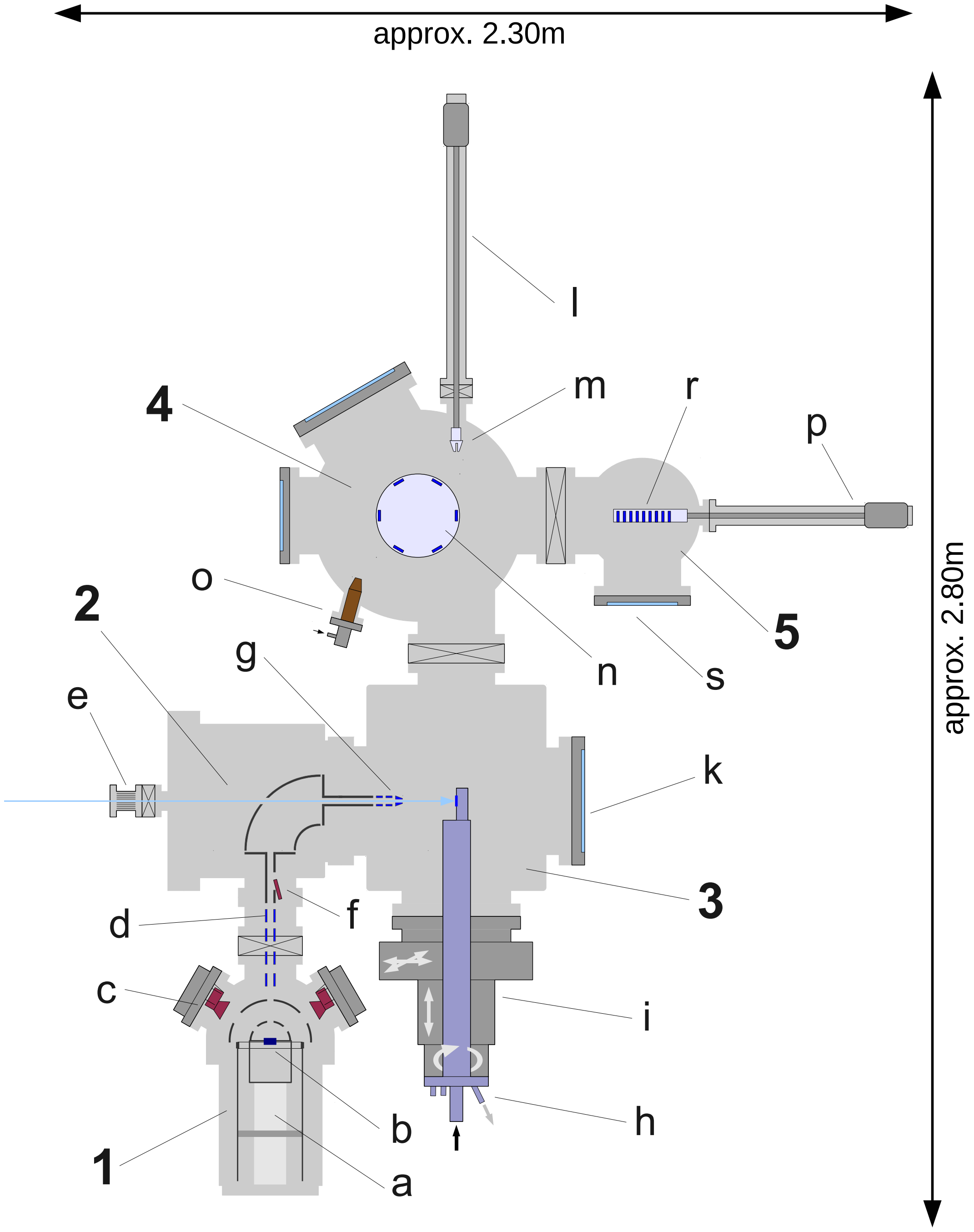

Figure 4.2. Overview of the apparatus (not to scale): **(1)** Mott detector with high-voltage feedthrough **a**, scattering target **b**, electron detectors **c** and transfer optics **d**. **(2)** Electron spectrometer with bellows to the beamline **e**, auxiliary electron detector **f** and entrance optics **g**. **(3)** Measuring chamber with lHe cryostat **h**, motorized sample stage **i** and viewport **k**. **(4)**. Preparation chamber with transfer rod **l**, sample transfer system **m**, rotatable sample storage **n** and ion gun **o**. **(5)** load-lock with rotatable transfer rod **p**, sample storage **r** and access door **s**. The horizontal arrow (cyan colored) represents the incoming synchrotron light.

4.1. Electron spectrometer and Mott polarimeter

The two components being most essential for the spin-resolved electron spectroscopy experiments presented in this work have been used successfully before [44, 186–189] and were described in more detail elsewhere (see [188, 189]). A schematic view of the setup is shown in figures 4.2 and 4.3.

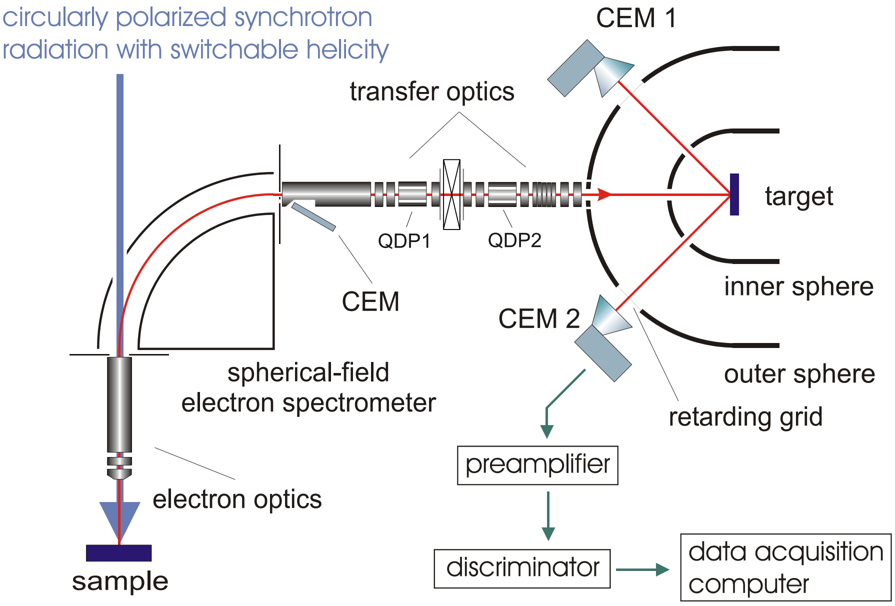

Figure 4.3. Schematic view of the electron spectrometer and the Mott polarimeter. Also shown is the position of the main electron detectors (**CEM1**, **CEM2**) and the auxiliary detector (**CEM**) mounted off-axis behind a separate exit slit. Note that the Mott polarimeter is shown rotated around its axis by 90°.

In the currently used setup, the electrons escaping from the sample surface enter a three-element electron lens that images the source point into the entry plane of the 90° spherical-field spectrometer. The spectrometer has a mean radius of 84 mm [186]. A set of three auxiliary electrodes on each side of the spherical section reduces the influence of fringe fields on the electron path. Using a path energy of 140 eV and an exit slit width of 2 mm, the energy resolution was approx. 1.7 eV for the main detection channels CT2 and CT4 in the Mott polarimeter (see figure 4.4). The auxiliary channel electron multiplier (type KLB210, see [190]) within the electron spectrometer which is used to record intensity spectra without spin resolution exhibits a slightly better energy resolution of 1.1 eV due to its smaller (separate) exit slit. The energy offset of the auxiliary detector being mounted slightly off-axis behind a separate exit slit was determined to be +2,5 eV with respect to the main electron trajectory towards the Mott polarimeter.

Determination of the electron spectrometer resolution. The condition of the electron spectrometer was checked regularly by measuring the $4f$ photoelectrons from an Au coated sample substrate. The spin-orbit split double peak structure with binding energies of 87.6 eV (Au $4f_{5/2}$) and 83.9 eV (Au $4f_{7/2}$) [118] allows the estimation of the obtained energy resolution in the three detection channels used. The data shown in figure 4.4 reveal FWHM peak widths of 1.63 eV (Au $4f_{7/2}$) and 1.75 eV (Au $4f_{5/2}$) obtained with the main detection channels CT2 and CT4. With the intrinsic linewidth of these peaks being less than 0.3 eV [191] and an excitation bandwidth of the same order of magnitude, the peak widths are predominantly determined by the spectrometer resolution.

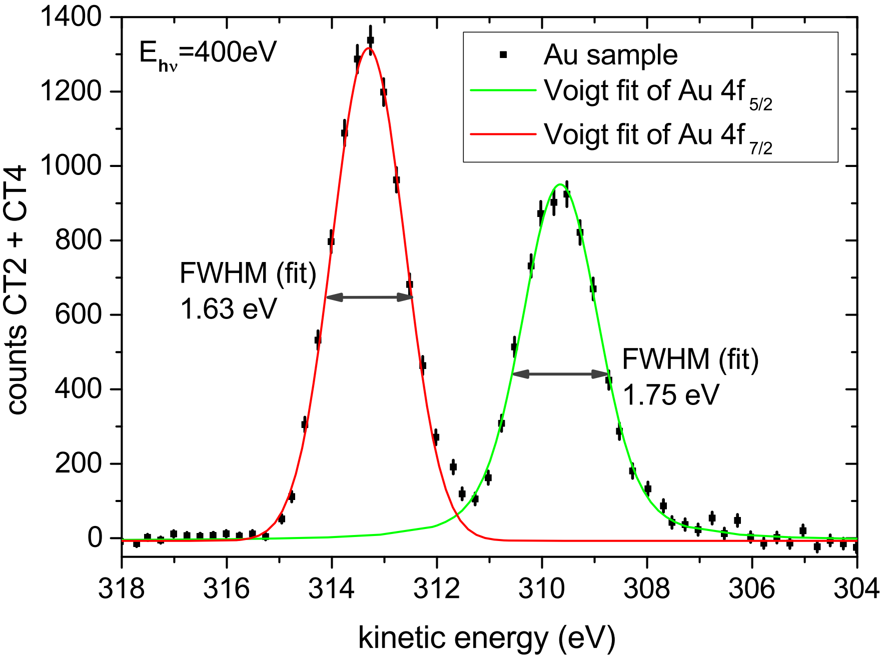

Figure 4.4. The spin-orbit split Au $4f$ double line recorded with the electron spectrometer. The counts from both detection channels CT2 and CT4 of the Mott polarimeter have been summed up, the errorbars show the statistical error of the combined measurements. A background subtraction was performed and both peaks were each fitted with a Voigt profile, leading to the FWHM results shown in the figure. With both the intrinsic linewidth and the bandwidth of the synchrotron radiation being approx 0.3 eV, the FWHM values represent the resolution of the electron spectrometer.

A comparison of the energetic positions of the Au $4f$ lines with reference data (see [118]) in principle allows the determination of the spectrometer work function Φ_{Spec}. By using the relation [192]

$$E_{\text{kin}} = h\nu - E_B - \Phi_{\text{Spec}} \tag{4.1}$$

a calibration of the spectrometer with respect to the binding energy E_B can be established if the spectrometer work function is known. However, large shifts on the energy scale were observed due to charging effects involved in the electron spectroscopy measurement of highly insulating $[\mathbf{Mn}_\mathbf{6}^{\mathbf{III}}\mathbf{Cr}^{\mathbf{III}}]^{3+}$ and $\mathrm{Mn}^{\mathrm{II}}$acetate samples. Therefore an absolute energy calibration was not performed. The electron spectroscopy results shown in Chapter 5 are given with respect to the valence band maximum (VBM) instead, which required the recording of spectra up to the valence band edge, but allowed the correction of charging related energy shifts.

The electrons leaving the spectrometer are guided to the Mott polarimeter by a transfer electron optics (see figure 4.3). A single lens at the spectrometer exit collimates the electron beam which is then retarded to a low energy at the entrance hole in the outer sphere of the Mott polarimeter, minimizing errors due to a non-zero lateral impulse of the electrons entering the spherical acceleration field. The other elements shown are operated at the same potential and act as a simple drift tube. Two sets of beam-steering plates (**BSP1**, **BSP2**) are used to adjust the electron beam.

Upon entering the spherical Mott polarimeter of the Rice type [193], the incoming electrons are accelerated by a potential difference of 45 kV between the outer and the inner sphere of the polarimeter and hit a thorium target mounted in the centre of the inner sphere. Electrons scattered back into the ±120° directions cross the accelerating field again in opposite direction and are decelerated. They are collected by two channel electron multipliers outside the outer sphere. The scattering process at the high-Z target material is spin dependent due to spin-orbit coupling (see section 2.3.2) and a spin polarization of the incoming electrons leads to an asymmetry in the count rates of the two detectors. Retarding grids in the openings of the outer sphere allow discrimination against inelastically scattered electrons due to their energy loss. Only electrons with an energy loss below 630 eV have been accepted by the detectors for the measurements presented within this work.

The pulses from the channel electron multipliers are processed by low-noise preamplifiers (type PAD06, see [190]) followed by a discriminator operated in integral mode. The preamplifiers are operated from a sealed lead acid (SLA) battery supply providing the symmetric ±6 V needed. Pulse counting is performed by a computer-based data acquisition system accessible via LabView control software. The count rates of all three detectors can be monitored easily via analogue rate meters for fast adjustment purposes.

Calibration of the Mott polarimeter. The spin polarization sensitivity S_{eff} of a Mott polarimeter depends on the scattering energy resp. acceleration voltage as well as on the scattering angle (see section 2.3.2) and the properties of the scattering target used. The following procedure was performed to provide a means of calibration for the Mott polarimeter used within this work:

Low-energy electron diffraction (LEED) on a platinum single crystal leads to a spin polarization of up to 80 % in the outgoing electron beams forming the diffraction pattern if certain conditions with respect to electron energy and diffraction geometry are met. Based on the method described in [194], a LEED experiment was done on a platinum(111) crystal surface, using an electron energy of 80 eV and an angle of incidence of 47° with respect to the surface normal. The specular reflection (0th order diffraction, scattering angle equals incident angle) was selected. Rotating the Pt crystal in its surface plane leads to a characteristic pattern in the recorded polar diagrams with respect to intensity and spin polarization (see [194] page 71). Figure 4.5 shows an example of a polar diagram recorded at a Mott polarimeter acceleration voltage of 25kV.

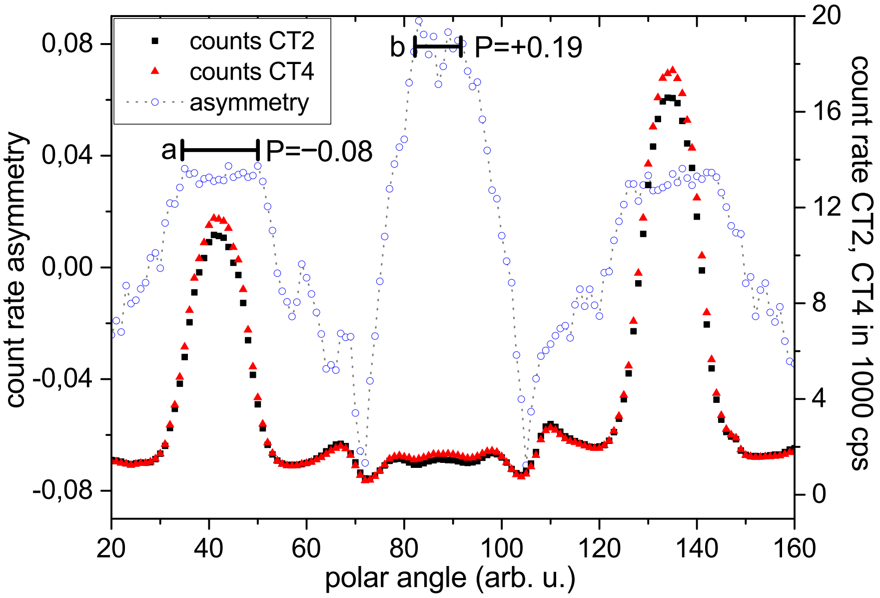

Figure 4.5. An example for the polar diagrams used in the Mott polarimeter calibration process. The black squares and red triangles represent the count rates $I_{\mathrm{CT2,\,CT4}}$ of the two electron detectors (right vertical axis). The blue circles show the count rate asymmetry calculated as $(I_{\mathrm{CT4}} - I_{\mathrm{CT2}})/(I_{\mathrm{CT4}} + I_{\mathrm{CT2}})$ (left vertical axis). The spectral features marked **a** and **b** are easily identified in [194], the spin polarizations obtained in [194] are given next to the markings.

According to equations 2.19 and 2.20 the polarization P, the Sherman function S and the count rates of the two detectors placed symmetrically on two sides of the scattering target are connected by the following relation:

$$\frac{N_{\mathrm{left}} - N_{\mathrm{right}}}{N_{\mathrm{left}} + N_{\mathrm{right}}} = P \cdot S \tag{4.2}$$

As the LEED setup did not allow to flip the whole scattering geometry in order to eliminate inherent asymmetries of the measurement setup, an additional parameter r is introduced to account for this apparatus-related asymmetry. Replacing the theoretical Sherman function S

with the polarization sensitivity S_{eff} introduced in chapter 2.3.2 then yields:

$$\frac{rN_{\text{left}} - N_{\text{right}}}{rN_{\text{left}} + N_{\text{right}}} = P \cdot S_{\text{eff}} \tag{4.3}$$

As shown in figure 4.5, two characteristic spectral features have been identified in the polar diagrams. Therefore two sets of correlated values for (N_{right}, N_{left}, P) are available. Based on equation 4.3 and the known values for the count rates N_{right}, N_{left} and the polarization P (P=-0.08 for region *a*, P=+0.19 for region *b*) a system of two equations with two unknowns S_{eff} and r has to be evaluated.

A different experimental approach was chosen instead of recording polar diagrams as shown in figure 4.5 in order to reduce the statistical error of the measurements: Based on these diagrams, a polar angle corresponding to region *a* or *b* was set and then data were integrated at each fixed angular position for 300s. The measurements were performed for different acceleration voltages of the Mott polarimeter, leading to the following results:

$$S_{\text{eff, 25kV}} = -0.17 \pm 0.02 \qquad\qquad S_{\text{eff, 45kV}} = -0.23 \pm 0.02$$

The error of the polarization sensitivity S_{eff} has been determined from the statistical error of the two count rates and the error of the polarization data from [194]. For the latter, an uncertainty of ±0.01 has been estimated from the polarization diagram given in [194].

4.2. Electron detectors

The electron detectors currently used in the Mott polarimeter are based on ceramic channel electron multipliers (manufacturer: Dr. Sjuts Optotechnik, see [190]) due to their durability and the reasonably low dark count rates (approx. 1.5 s^{-1}) compared to the previously used multichannel plate (MCP) detectors (up to 20 s^{-1}). The MCP detectors provided a circular active area of approx. 40 mm diameter. A special type of channel electron multiplier with a circular funnel of 25 mm diameter (type KBL25RS/90, see [190] and figure 4.6 left) was selected as a replacement, minimizing the loss of sensitivity due to the smaller area presented to the (diverging) scattered electron beam.

The electron multiplier is mounted to an adjustable aluminum carrier that connects to the CF63 stainless steel base flange via three threaded bronze rods, allowing to adjust the height of the electron multiplier above the base flange as well as the angle with respect to the flange axis (see figure 4.6 right). The selected combination of materials avoids galling in the threads under vacuum conditions. A circular auxiliary electrode with an inner diameter of 38 mm

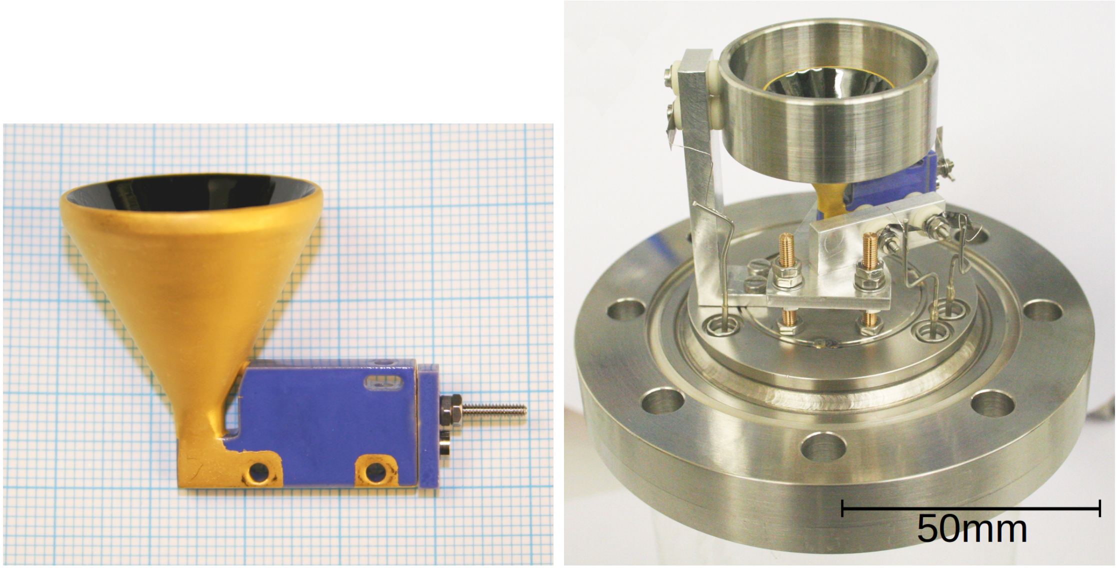

Figure 4.6. Left: Type KBL25RS/90 channel electron multiplier with 25 mm diameter entry funnel used for the electron detection in the Mott polarimeter. Right: Complete detector assembly with the mounted channel electron multiplier and the auxiliary electrode, the bias voltage divider and readout capacitor are placed under a stainless steel enclosure at the back of the base flange.

around the channel electron multiplier funnel is mounted via electrically isolating ceramic spacers and allows to constrict the trajectories of the incoming electrons in order to maximize the electron collection efficiency of the detector.

The outside of the detector base flange is covered by an metal cup containing the bias voltage divider chain for the channel electron multiplier as well as the readout capacitor and the BNC and SHV connectors for the signal, the multiplier high voltage and the auxiliary electrode potential. The design of the voltage divider chain elevates the entry funnel of the electron multiplier to approx. +200 V with respect to ground potential. Signal readout is performed via a 1 nF ceramic capacitor followed by a pair of antiparallel protection diodes (type 1N4148). In case of voltage spikes exceeding the approx. 1 V forward voltage of the diodes, they start conducting and limit the voltage, thereby protecting the sensitive input of the preamplifier.

4.3. Load-lock, sample transfer system and preparation chamber

The measuring chamber with the electron spectrometer and Mott polarimeter described before is completed by a preparation chamber, a sample storage and load-lock system that allows a convenient transfer of samples from air to UHV within approx. one hour.

After preparation (see section 3.2) the $\mathbf{[Mn_6^{III}Cr^{III}]^{3+}}$ samples are mounted to rectangular stainless steel or tantalum sample plates compatible to the commercially available sample transfer tool (see figure 4.7 left) made by Omicron Nanotechnology [195]. A load-lock equipped with a 100 mm diameter access door and a sample tray with a capacity of nine sample plates is used to transfer the $\mathbf{[Mn_6^{III}Cr^{III}]^{3+}}$ samples to the UHV system. The sample tray is mounted to a rotatable magnetic transfer rod that allows sample transfer to the preparation chamber.

A second magnetic transfer rod perpendicular to the first one is equipped with the aforementioned tool and provides sample transfer from the preparation chamber to the measuring chamber (see figure 4.2). It is non-rotatable; the rotation of the magnet operates the opening/closing mechanism of the transfer tool via a second, coaxial shaft instead. The preparation chamber is equipped with a rotatable, wheel-shaped sample storage that can be moved vertically between two planes: The lower plane is accessible by the magnetic transfer rod and allows transfering samples to the measuring chamber and the load-lock sample tray while the upper plane contains an ion gun for sample surface preparation and is prepared for further sample characterization equipment such as a LEED system. One of the sample holders of the storage wheel is mounted via isolating ceramic spacers and allows electron bombardment heating of a sample by means of a tungsten filament mounted behind the sample holder. A quadrupole mass spectrometer installed in the preparation chamber provides residual gas analysis for leak detection as well as during sample preparation (i.e. monitoring heating or sputtering processes).

Besides sample preparation, the preparation chamber allows the storage of up to six samples under UHV conditions. Interruptions in the measurement process due to load-lock pumpdown are avoided because the sample transfer from the preparation chamber to the measuring chamber is independent from the load-lock transfer rod.

Upon transfer into the measurement chamber, the sample is inserted into a specially shaped slot at the head of a lHe flow cryostat capable of cooling the sample to the 20 K temperature range. A spring-loaded molybdenum frame presses the sample against the cryostat head (see figure 4.7 right). While the pressure of the spring mechanism keeps the sample plate sufficiently fixed for room temperature measurements, four non-magnetic bronze screws are used to tighten the molybdenum frame against the sample plate to ensure a good thermal contact between sample plate and cryostat head when lHe cooling is used. The whole cryostat head is electrically insulated from the vacuum vessel by a sapphire plate to allow sample current measurements. Sapphire was chosen due to its good electrical insulating properties and sufficiently high thermal conductivity.

A three-axis manipulator (y and z ranges ± 25 mm, x range 150 mm) with an additional differentially pumped rotary stage allows the positioning of the sample in front of the spectrometer entrance optics as well as rotating the sample stage for transfer purposes. The x and y directions of the manipulator are motorized by stepper motors for convenient sample positioning and sample scanning during the measuring process.

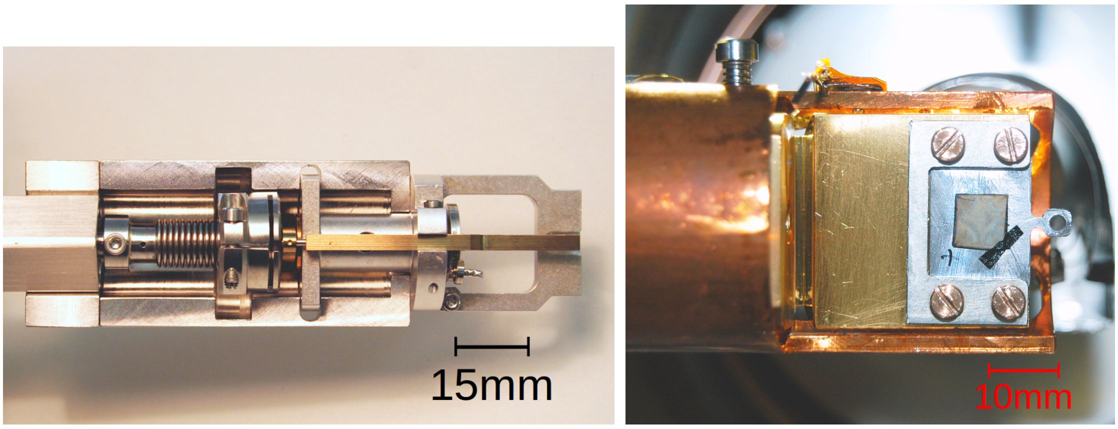

Figure 4.7. The sample transfer system used in the UHV apparatus. Left: The sample transfer tool (manufacturer: Omicron Nanotechnology, see [195]) mounted at the end of a magnetic transfer rod. Right: The sample holder at the head of the lHe cryostat. The molybdenum frame is spring-loaded from the back side of the cryostat head and keeps the sample in place. A tantalum sample plate with a $[\mathbf{Mn}_6^{\mathbf{III}}\mathbf{Cr}^{\mathbf{III}}]^{3+}$ sample on Si is shown inserted into the sample holder. The cryostat assembly (apart from the sample holder region shown) is surrounded by a copper radiation shield cooled from an intermediate stage of the cryostat.

4.4. Vacuum design and requirements

The vacuum system of the apparatus was planned and constructed with respect to three main requirements, leading to the final design (see figure 4.8 for an overview) that will be described in detail within this section.

- The **UHV conditions** necessary for the planned electron spectroscopy experiments at synchrotron facilities have to be provided.
- A **load-lock** system allowing fast sample transfer from air to UHV has to be implemented, as the limited radiation stability of the $[\mathbf{Mn}_6^{\mathbf{III}}\mathbf{Cr}^{\mathbf{III}}]^{3+}$ samples requires frequent sample changes.
- A **short setup time** to reach the operational state after transporting the apparatus to a synchrotron radiation facility is mandatory, as beamtime allocation is usually severely restricted.

The first requirement determined the choice of pumps for the measurement chamber and the preparation chamber. Both are pumped by ion getter pumps during normal operation, providing a pumping speed of approx. 270 l/s each. The pumps are equipped with eight diode cells of approx. 100 mm · 200 mm per pump. Differential pumping elements using both Ti and

Ta plates increase the pumping efficiency for noble gases. An additional titanium sublimation pump in each chamber is operated in 2-hour intervals. Turbomolecular pumps with a pumping speed of 70 l/s (N_2) backed by a diaphragm roughing pump are used during pump-down after venting as well as during noble gas ion gun operation. The rotary feedthrough for the sample cryostat comprises two differential pumping stages: The UHV side is pumped by a small (approx. 2 l/s) ion getter pump whereas the high-pressure part is connected to an intermediate port of the measuring chamber turbomolecular pump. The Mott polarimeter is pumped independently from the measuring chamber by a 40 l/s ion getter pump, a turbomolecular pump is connected temporarily for pump-down. The pressures after bakeout as well as during normal operation are given in table 4.1. Note that the operating pressure of the Mott polarimeter is limited by the fact that the ion getter pump has to be deactivated during measurements due to electron detector noise issues. Pumping the Mott polarimeter from the main chamber is less efficient and causes the pressure rise indicated in table 4.1.

The load-lock of the apparatus is accessible via a flange of 100 mm inner diameter sealed by a non-bakeable viton gasket, limiting the base pressure of the load-lock to approx. $5 \cdot 10^{-8}$ mbar. Pumping is done via a 70 l/s turbomolecular pump, a complete vent and pump-down cycle of the load-lock takes approx. one hour until a pressure of $5 \cdot 10^{-7}$ mbar is reached. The load-lock can be vented using either dry nitrogen or high-purity inert gas, the latter allowing preparation of samples in the load-lock under inert gas conditions.

Vacuum measurement is done by ionization gauges in all parts of the apparatus except in the load-lock. A cold cathode (inverted magnetron) gauge is used there instead, taking the detrimental influence of ionization gauges on $\mathbf{[Mn_6^{III}Cr^{III}]^{3+}}$ samples [61] at higher pressures (see section 5.5) into account. Additional convection-enhanced Pirani manometers complement the ionization gauges in the high-pressure regime up to atmospheric pressure for all vessels except the Mott polarimeter. The inlet pressure of the diaphragm roughing pump serving all turbomolecular pumps via a distribution board is also measured by a Pirani gauge. The rotation of all turbomolecular pumps as well as the roughing vacuum pressure are monitored by an interlock system that automatically closes pneumatically actuated vacuum valves (see figure 4.8) in case of a mains power or pump failure.

Measurement and preparation chamber are pumped down and baked out prior to the transport to reduce the setup time needed to reach a fully operational state after transporting the apparatus to a synchrotron facility. With all valves closed, the vacuum in the main chambers is sustained for a period of more than 24 hours without pumping. Subsequent restarting of the ion pumps reestablishes the base pressure within a few hours. A pressurized nitrogen gas cylinder connected to the apparatus ensures the correct operation of the pneumatically actuated valves during transport.

The Mott polarimeter and the magnetic transfer rod attached to the preparation chamber are removed during transport, requiring valves to separate them from the evacuated vessels. These components are reinstalled upon reaching the beamline. A fourth turbomolecular pump is connected to the Mott polarimeter; additional removable connections to this pump allow the pump-down of the transfer rod and the bellows connection to the beamline as well.

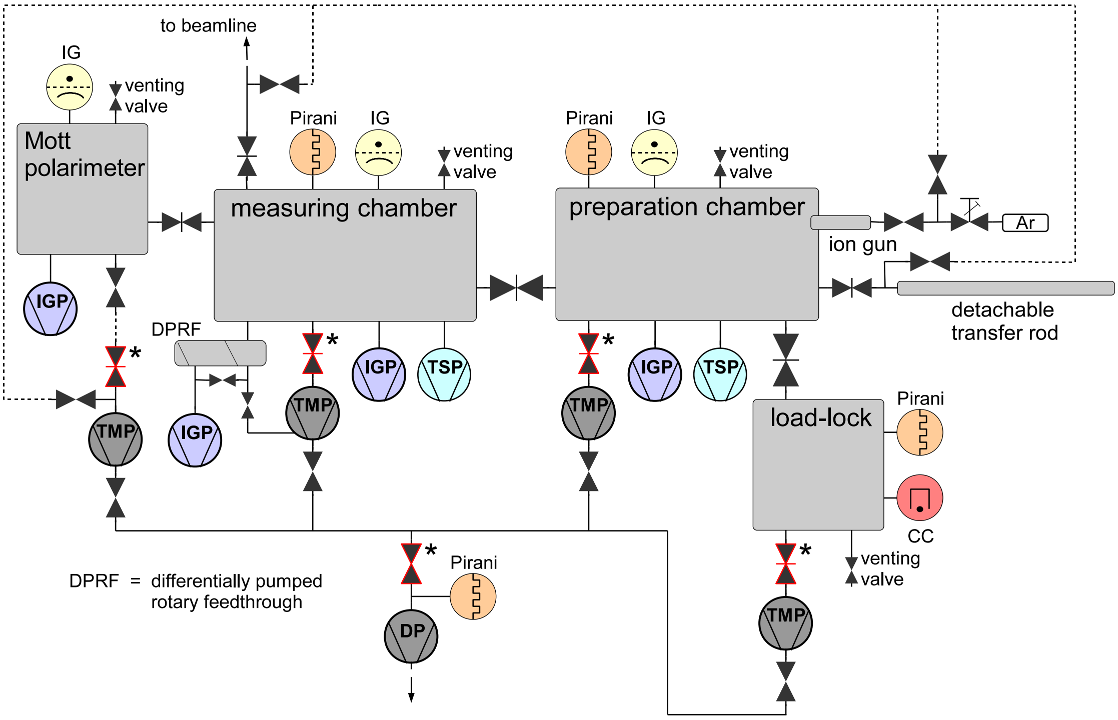

Figure 4.8. Schematic overview of the vacuum system. The pumping types shown are turbomolecular pumps (**TMP**), ion getter pumps (**IGP**), titanium sublimation pumps (**TSP**) and a diaphragm roughing pump (**DP**). Vacuum measurement is done by ionization gauges (**IG**), convection-enhanced Pirani gauges and a cold cathode gauge (**CC**) in the load-lock. The valves with red outlines* are closed automatically by an interlock system if any of the turbopumps or the roughing pump fail. Connections indicated by dotted lines are made temporarily for pump-down purposes only.

measuring chamber	prep chamber	Mott detector	load-lock
	pressures after bakeout (mbar)		
$\leq 1 \cdot 10^{-10}$	$1 \cdot 10^{-10}$	$5 \cdot 10^{-10}$	$5 \cdot 10^{-8}$
	pressures during normal operation (mbar)		
$\approx 5 \cdot 10^{-10}$	$5 \cdot 10^{-10}$	$5 \cdot 10^{-9}$	$1 \cdot 10^{-7}$

Table 4.1. Vacuum conditions: The pressure in different parts of the apparatus after pump-down and bakeout and during normal measurement operation is shown. Note that the load-lock is not baked due to the non-bakeable viton gasket of the access door.

5. Results and Discussion

The results obtained from $[\mathbf{Mn_6^{III}Cr^{III}}]^{3+}$ SMM as well as from different reference materials using the methods and the experimental setup described above will be presented. X-ray absorption spectroscopy was used for sample characterization, giving important insights into effects related to preparation and radiation exposure, see sections 5.1 and 5.2. XPS investigation of $[\mathbf{Mn_6^{III}Cr^{III}}]^{3+}$ samples provided information about the Auger lines used for the spin-resolved measurements as well as about radiation damage effects, see section 5.3. Spin-resolved electron spectroscopy and X-ray circular dichroism results yield information about the magnetic properties of the Mn constituents in $[\mathbf{Mn_6^{III}Cr^{III}}]^{3+}$ being discussed in sections 5.4 to 5.7.

5.1. Characterization of $[\mathbf{Mn_6^{III}Cr^{III}}]^{3+}$ samples

Prior to any further investigations, the $[\mathbf{Mn_6^{III}Cr^{III}}]^{3+}$ samples prepared as described in chapter 3.2 were characterized by X-ray absorption spectroscopy at the Mn L_3-edge. This method is a very useful tool for detecting preparation-related changes of the molecule condition due to its sensitivity to the oxidation state of the Mn constituents in the $[\mathbf{Mn_6^{III}Cr^{III}}]^{3+}$ SMM.

Reference data obtained by XAS from bulk manganese oxides Mn_2O_3 (Mn^{III}) and MnO (Mn^{II}) are shown in figure 5.1. The distinct peak observed at 640.1 eV (labeled **A** in figure 5.1) in MnO is known to be characteristic for the Mn^{II} oxidation state [196]. Accordingly, the broad absorption feature at approx. 642 eV (labeled **B** in figure 5.1) can be attributed to the main Mn^{III} L_3-edge absorption [120].

Using these reference spectra, the Mn^{III} content of a $[\mathbf{Mn_6^{III}Cr^{III}}]^{3+}$ sample can be estimated from the **B**/**A** peak ratio following the approach described on page 72 (see [61] for details). This provides a simple method to quantify and compare the influence of preparation parameters, environmental influences or radiation exposure on the $[\mathbf{Mn_6^{III}Cr^{III}}]^{3+}$ sample condition.

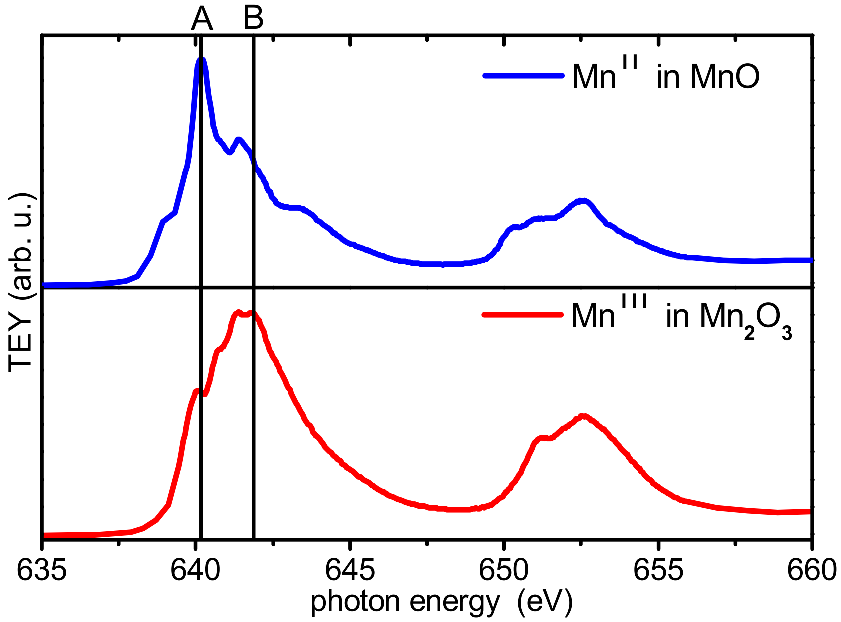

Figure 5.1. Mn $L_{2,3}$-edge XAS reference data obtained from manganese oxides MnO (Mn^{II}) and Mn_2O_3 (Mn^{III}). The markings **A** (**B**) refer to spectral features characteristic for Mn^{II} (Mn^{III}). Figure already published in [61].

5.1.1. Characterization of samples prepared by drop-casting – the influence of $[Mn_6^{III}Cr^{III}]^{3+}$ layer thickness

The first $[\mathbf{Mn_6^{III}Cr^{III}}]^{3+}$ samples were prepared by drop-casting (see chapter 3.2.1) the SMM solutions onto square substrates of approx. 5×5 mm^2. XAS measurements were performed in order to detect possible changes of the molecule condition due to the preparation of the $[\mathbf{Mn_6^{III}Cr^{III}}]^{3+}$ solutions and the deposition process. It is well known for other SMM species like $\mathbf{Mn_{12}ac}$ that the interaction with the substrate surface [197, 198] leads to changes of the SMM condition upon deposition, altering or even completely suppressing the unique magnetic behavior of the SMM [31, 198]. Charge transfer processes between the substrate and the adsorbed SMM layer are considered to be the predominant reason for the observed reduction effects upon deposition [199].

Different $[\mathbf{Mn_6^{III}Cr^{III}}](ClO_4)_3$ samples on gold and ruthenium substrates (see chapter 3.2) were prepared by drop-casting from SMM solutions in order to investigate the role of the molecule-substrate interaction. The following range of concentrations was used, each dilution step leading to a five times lower $[\mathbf{Mn_6^{III}Cr^{III}}]^{3+}$ concentration:

$\mathbf{4.5\cdot10^{-4}}$ mol/l	→	$\mathbf{9\cdot10^{-5}}$ mol/l	→	$\mathbf{1.8\cdot10^{-5}}$ mol/l	→	$\mathbf{3.6\cdot10^{-6}}$ mol/l
μm-sized microcrystallites				monolayer equivalent		

Microcrystallites with a size of approx. 3 μm form on the substrate during solvent evaporation for the highest concentration (see figure 3.6). The occurrence of monolayer-like island structures for lower concentrations of the $[\mathbf{Mn_6^{III}Cr^{III}}]^{3+}$ solution has been confirmed by non-contact AFM measurements [200]. The obtained $[\mathbf{Mn_6^{III}Cr^{III}}]^{3+}$ samples were then characterized by XAS (see figure 5.2).

In contrast to results obtained from $\mathbf{Mn_{12}ac}$ [199], no substrate- or deposition-induced reduction effects of the Mn constituents in $[\mathbf{Mn_6^{III}Cr^{III}}]^{3+}$ could be observed – the characteristic shape of the Mn L_3-edge absorption clearly indicates the predominance of $\mathrm{Mn^{III}}$ (see the $\mathrm{Mn^{III}}$ vs. $\mathrm{Mn^{II}}$ comparison in figure 5.1). A quantitative evaluation yields a $\mathrm{Mn^{III}}$ fraction very close to 1.0 even for the highest dilutions (see insets in figure 5.2), confirming the feasibility of $[\mathbf{Mn_6^{III}Cr^{III}}]^{3+}$deposition on surfaces without degradation of the SMM molecules due to molecule-substrate interaction.

5.1.2. Homogeneity of samples prepared by airbrush method

The application of sample scanning (see chapter 3.4) required a preparation method capable of obtaining large homogeneous samples. This requirement was met by the airbrush preparation technique (see section 3.2.2). Sample homogeneity with respect to the $[\mathbf{Mn_6^{III}Cr^{III}}]^{3+}$ condition (oxidation state) is crucial in order to allow combining the results from a large number of sample positions. The homogeneity of the $[\mathbf{Mn_6^{III}Cr^{III}}]^{3+}$ samples prepared by the airbrush technique has been checked by performing a number of XAS measurements on different positions covering the sample surface of 11×11 mm^2 (see figure 5.3).

The results of the XAS characterization show a very good agreement between different positions on the sample prepared by airbrush technique. All measured positions show comparable absorption yields, confirming the homogeneous covering of the sample surface with $[\mathbf{Mn_6^{III}Cr^{III}}]^{3+}$ deposits already found in optical microscopy (see figure 3.8).

Furthermore, all positions exhibit a comparable $[\mathbf{Mn_6^{III}Cr^{III}}]^{3+}$ condition with respect to the Mn oxidation state, as indicated by the overall shape of the Mn L_3 edge absorption (see fig. 5.1 for comparison). This is the most important condition to be fulfilled with regard to sample scanning during the SPES measurements, ensuring that only $[\mathbf{Mn_6^{III}Cr^{III}}]^{3+}$ molecules in the same condition are considered when collecting data from a large number of different sample positions.

5.1.3. Detrimental influences on the $[\mathbf{Mn_6^{III}Cr^{III}}]^{3+}$ sample condition

Other detrimental influences on the sample condition may be present besides a possible molecule-substrate interaction as found for $\mathbf{Mn_{12}ac}$ SMM [199]: The preparation is carried

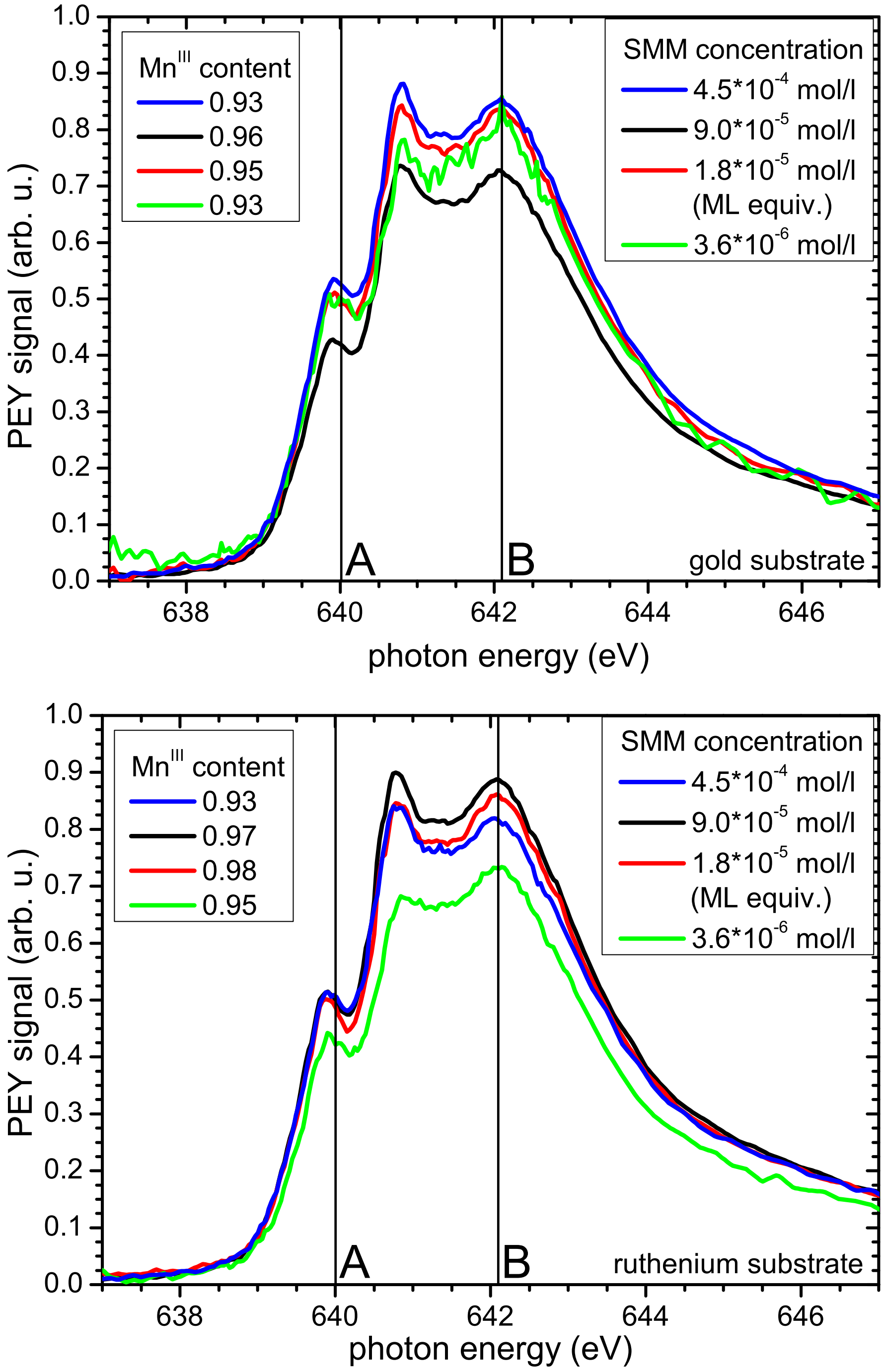

Figure 5.2. XAS characterization of [$\mathbf{Mn_6^{III}Cr^{III}}$](ClO$_4$)$_3$ samples prepared by drop-casting technique from solutions with different [$\mathbf{Mn_6^{III}Cr^{III}}$]$^{3+}$ concentrations on gold (top panel) and ruthenium (bottom panel) substrates. The concentrations used as well as the Mn^{III} content calculated from the **B**/**A** peak ratio are given in the insets. The XAS spectra shown are obtained by averaging over several scans to improve the signal-to-noise ratio, especially for the low [$\mathbf{Mn_6^{III}Cr^{III}}$]$^{3+}$ concentrations.

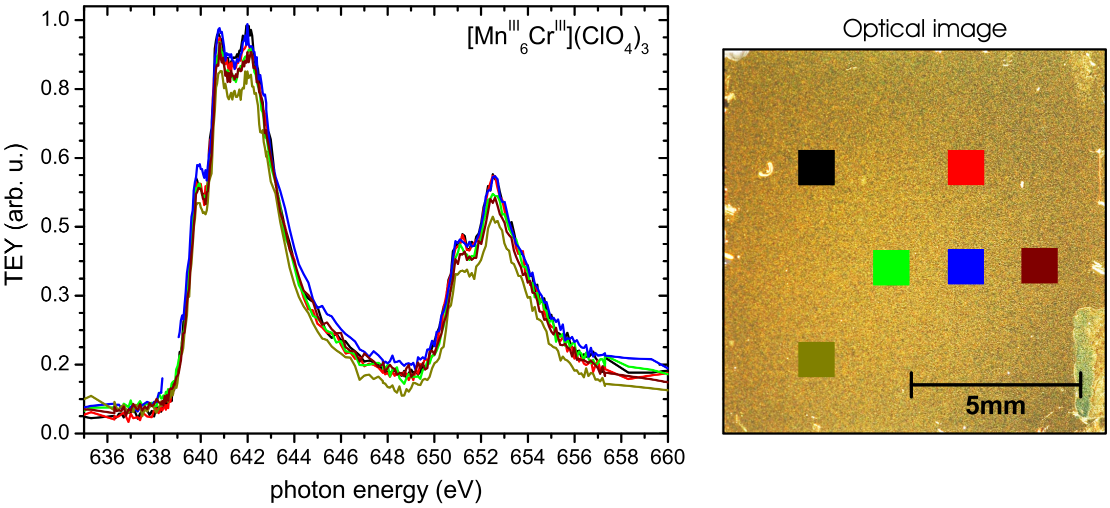

Figure 5.3. XAS characterization of $[\mathbf{Mn_6^{III}Cr^{III}}](\mathrm{ClO_4})_3$ samples prepared by airbrush technique. Left: Mn L_3-edge absorption spectra obtained from different positions on the 11×11 mm^2 substrate are in good agreement with respect to signal intensity and spectral shape. Right: Optical image of the airbrushed $[\mathbf{Mn_6^{III}Cr^{III}}](\mathrm{ClO_4})_3$ sample. The colored squares mark the measurement positions for the absorption spectra on the left.

out in ambient conditions, thus atmospheric humidity as well as oxygen are present during the deposition process and the sample handling. Upon transfer into the load-lock of the UHV system, the $[\mathbf{Mn_6^{III}Cr^{III}}]^{3+}$ samples are subject to changing vacuum conditions and possible influences of ion pumps, sublimation pumps and ionization gauges. Systematic studies of these influences on the $[\mathbf{Mn_6^{III}Cr^{III}}]^{3+}$ condition have been carried out.

Solvent contamination and aging

The methanol being used as a solvent as well as the prepared $[\mathbf{Mn_6^{III}Cr^{III}}]^{3+}$ solutions are exposed to atmospheric humidity during sample preparation and storage. A deliberate water contamination of 1.0 % and 5.0 % (referring to volume) was introduced into dried methanol (SeccoSolv brand by Merck) to study the influence of water on the condition of the $[\mathbf{Mn_6^{III}Cr^{III}}]^{3+}$ solutions. Samples prepared from these solutions have been characterized by XAS (see figure 5.4, top panel). The effect of atmospheric humidity being present during the SMM deposition on the substrate was also studied: A silicon substrate was cooled down to liquid nitrogen temperature and then exposed to atmospheric conditions during the warm-up to room temperature. A water film originating from atmospheric humidity formed on the substrate surface. The preparation process was then conducted as described before, followed by XAS sample characterization.

The presence of atmospheric oxygen is known to cause corrosion effects in industrial storage and handling of methanol [201, 202]: The partial oxidation of methanol leads to the formation of formic acid causing stress corrosion cracking in metallic vessels. The existence of methanol oxidation in ambient conditions might lead to an aging process of the solvent used for the $\mathbf{[Mn_6^{III}Cr^{III}]^{3+}}$ preparation, causing a formic acid contamination increasing with time. To study possible influences on the SMM sample condition, a deliberate contamination of the solvent by 0.5 % and 5 % (referring to volume) formic acid was introduced prior to the preparation process and the resulting samples were characterized by XAS (see figure 5.4, bottom panel).

According to the XAS measurements performed on these samples (see figure 5.4), no significant influence of the presence of water or formic acid contaminations during the preparation and deposition of the SMM on the oxidation state of the manganese constituents in the molecule is found.

The overall spectral shape of the Mn L_3 absorption does not change with respect to the non-contaminated reference samples in the case of water contamination. A comparison with oxidic references (see figure 5.1) clearly indicates the predominance of manganese in the Mn^{III} oxidation state expected for the intact $\mathbf{[Mn_6^{III}Cr^{III}]^{3+}}$ SMM. Even the presence of an adsorbed water film on the substrate during the deposition process does not show a detrimental influence on the sample condition, which is in strong contrast to results obtained from $\mathbf{Mn_{12}ac}$ SMM [125]: For $\mathbf{Mn_{12}ac}$ the presence of water during preparation leads to an immediate reduction of the Mn constituents to the Mn^{II} oxidation state.

A contamination of the solvent with formic acid leads to significant changes in the spectral shape of the Mn L_3 absorption (see arrow in figure 5.4, bottom panel). However, the oxidation state of the Mn constituents remains unchanged, as indicated by the **B**/**A** peak ratio. It is notable that the spectral shape of the Mn L_3-edge for $\mathbf{[Mn_6^{III}Cr^{III}]}(BPh_4)_3$ samples influenced by formic acid resembles the results obtained from $\mathbf{[Mn_6^{III}Cr^{III}]}(C_3H_5O_3)_3$ (see figure 5.8) without exposure to formic acid.

Ionization gauge operation

Initially a Bayard-Alpert [203] ionization vacuum gauge was used to monitor the pressure in the load-lock in the $p \leq 10^{-4}$ mbar range (see section 4.4). The basic principle behind ionization gauge operation is as follows: A hot tungsten or oxide-coated iridium filament emits electrons, which are accelerated by a voltage of approx. 150 V towards a cage-like grid structure around the central ion collector. While moving towards the grid the electrons collide with residual gas atoms and ionize them. Afterwards the ions are collected by a thin wire in the center of the grid structure. The ion current I_c is related to the residual gas pressure P by the following equation:

$$I_c = S \cdot P \cdot I_e \tag{5.1}$$

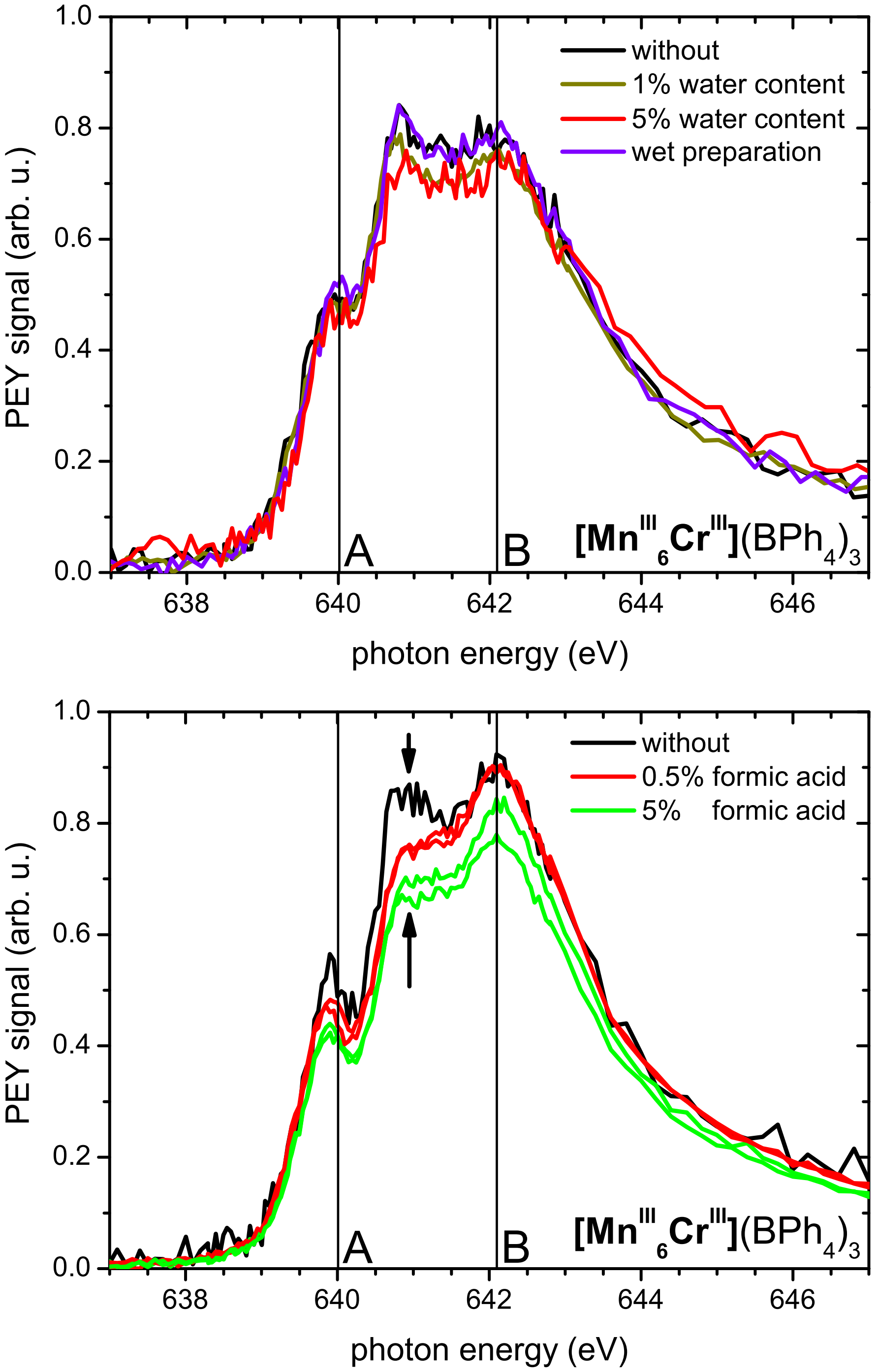

Figure 5.4. Influence of solvent contamination and aging on the $[\mathbf{Mn_6^{III}Cr^{III}}]^{3+}$ condition. Top panel: XAS spectra of $[\mathbf{Mn_6^{III}Cr^{III}}](\mathrm{BPh_4})_3$ obtained at the Mn-L_3 edge for different water concentrations in the solvent. The violet spectrum was obtained from a sample with a water film present during SMM deposition. The vertical lines mark absorption features characteristical for $\mathrm{Mn^{III}}$ (**B**) and $\mathrm{Mn^{II}}$ (**A**). Bottom panel: XAS characterization of samples prepared with different concentrations of formic acid present in the solvent. Meaning of vertical lines as before.

with S being a gauge-dependent calibration factor and I_e the electron emission current [204]. Due to this operation principle, an ionization gauge within the vacuum system represents a possible source of electrons, ions and excited metastable residual gas molecules [205, 206].

The influence of ionization gauge operation on $\mathbf{[Mn^{III}_6Cr^{III}]}^{3+}$ samples has been studied by placing samples into the load-lock of the UHV apparatus and exposing them to the active ionization gauge during pump-down. XAS measurements at the Mn L_3-edge have been performed on samples without operation of the ionization gauge and after one and two pump-down cycles with the gauge active (see figure 5.5). The chamber was vented using dry nitrogen (evaporated from a LN_2 dewar vessel) between the pump-down cycles.

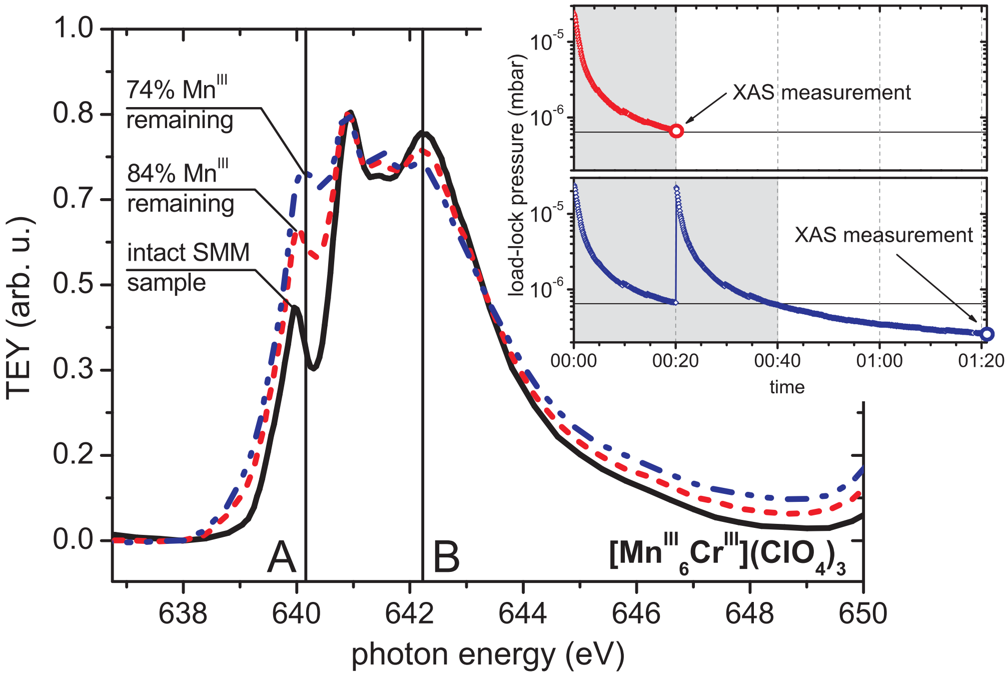

Figure 5.5. Influence of ionization vacuum gauge operation during load-lock pump-down on the $\mathbf{[Mn^{III}_6Cr^{III}]}(ClO_4)_3$ sample condition. Shown are Mn L_3-edge XAS characterizations of samples after one and two pump-down cycles compared to a reference sample without gauge operation. Meaning of vertical lines as in figure 5.4. Inset: Temporal evolution of load-lock pressure during pump-down. The time scale is given in 'hh:mm' format code. XAS measuring times are marked.

The XAS characterization of these samples shows distinct changes in the Mn L_3-edge absorption, which are similar to the changes caused by radiation exposure (see figure 5.6). Exposure of $\mathbf{[Mn^{III}_6Cr^{III}]}^{3+}$ SMM to the operating ionization gauge seems to cause a reduction of the Mn^{III} ions in the SMM to the Mn^{II} oxidation state. Approximately 84% of the Mn ions remain in the Mn^{III} oxidation state after one pump-down cycle of about 20 minutes with $p \geq 6 \cdot 10^{-7}$ mbar.

Performing a second cycle reduces this number to 74%. However, no influence of ionization gauge operation on the $[\mathbf{Mn_6^{III}Cr^{III}}]^{3+}$ sample condition was found in the UHV pressure range below 10^{-9} mbar, even for samples that had been stored in the preparation chamber for several days.

Due to the load-lock geometry, no direct, straight path existed between the ionization gauge and the samples, instead the gauge was connected to the load-lock via CF35 tubing including several 90° angles. Thus it is improbable that ions or electrons emitted by the gauge are the reason for the observed $[\mathbf{Mn_6^{III}Cr^{III}}]^{3+}$ reduction. Metastable residual gas molecules excited by electron collision [206] may play the leading role in the observed effect.

5.2. Stability of $[\mathbf{Mn_6^{III}Cr^{III}}]^{3+}$ SMM against soft X-ray exposure

The investigation of $[\mathbf{Mn_6^{III}Cr^{III}}]^{3+}$ single-molecule magnets by experimental methods involving soft X-rays is complicated by the occurrence of radiation damage effects – a well-known phenomenon in metal-organic compounds consisting of metal centers within an organic ligand structure [207, 208]. In hard X-ray protein crystallography [209], this severely limits integration time and signal quality. To a large extent, the radiation damage is not a direct consequence of irradiation; it is caused by the large number of secondary electrons that are created by photoexcitation within the sample and the underlying substrate instead [210]. The basic results and conclusions presented in this section have been already published in 2012, see [61].

Radiation damage occurring in $[\mathbf{Mn_6^{III}Cr^{III}}]^{3+}$ SMM is indicated by a noticeable change in the spectral shape of the manganese L_3-edge absorption: With increasing X-ray exposure, the broad multiplet structure at 642.2 eV (labeled **B** in figure 5.6) decreases while a sharp absorption peak rises at 640.1 eV (labeled **A** in figure 5.6) and later dominates the L_3-edge region. The initial presence of the broad absorption feature at 642.2 eV indicates the presence of manganese in the Mn^{III} oxidation state not only for bulk oxides, but also for manganese ions in a molecular environment [61, 121, 125, 196].

A comparison of the XAS results obtained from $[\mathbf{Mn_6^{III}Cr^{III}}]^{3+}$ SMM (see figure 5.6) with the reference data shown in figure 5.1 indicates that the oxidation state of the manganese constituents in the investigated $[\mathbf{Mn_6^{III}Cr^{III}}]^{3+}$ single-molecule magnets changes from Mn^{III} being present in the intact molecule [38] to Mn^{II} upon soft X-ray irradiation.

The exposure-dependent change in the L_3-edge absorption of the Mn centers in $[\mathbf{Mn_6^{III}Cr^{III}}]^{3+}$ SMM was monitored by series of consecutive XAS scans, each single measurement taking approx 4-5 minutes. As each sequence was measured at a single sample position, the investigation of the radiation effect on the sample condition was not influenced by possible

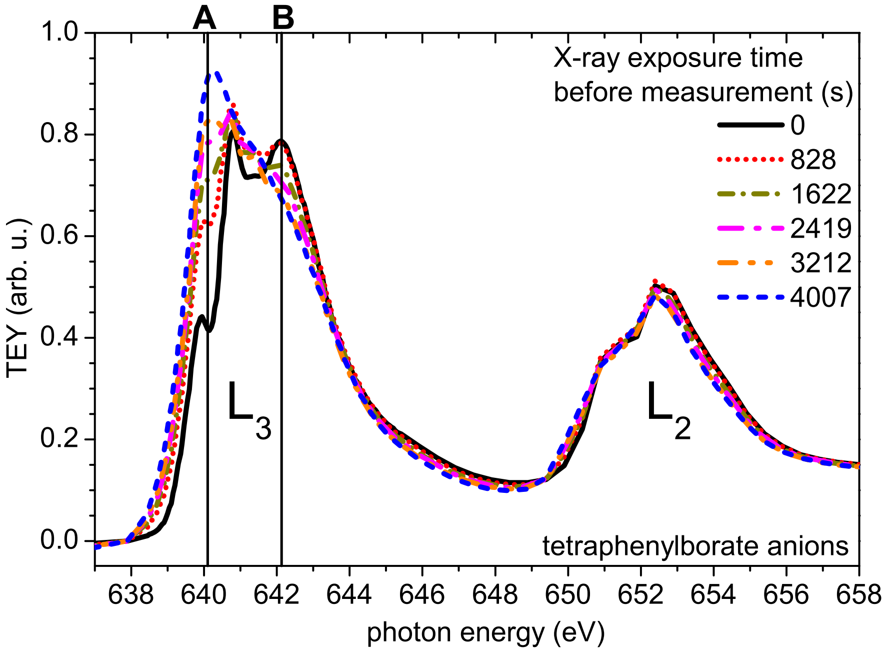

Figure 5.6. Mn $L_{2,3}$-edge XAS of $[\mathbf{Mn_6^{III}Cr^{III}}]^{3+}$ SMM with tetraphenylborate (BPh_4^-) anions. Selected spectra from a series of consecutive scans are shown to illustrate the radiation-induced changes occuring in $[\mathbf{Mn_6^{III}Cr^{III}}]^{3+}$ SMM. Meaning of markings **A** (**B**) as in figure 5.1.

differences in sample morphology or varying amounts of $[\mathbf{Mn_6^{III}Cr^{III}}]^{3+}$ present at different sample positions. The photon flux was controlled by changing the monochromator exit slit width.

With the spectral features at photon energies 640.1 eV (**A**) and 642.2 eV (**B**) being characteristic for the Mn^{II} and Mn^{III} oxidation state, respectively, the peak absorption ratio **B**/**A** is a useful qualitative indicator of the SMM sample condition with respect to radiation damage. However, the peak ratio does not directly represent the Mn^{III}/Mn^{II} ratio present in the sample, as both oxidation states contribute to the absorption at **A** and **B**.

The procedure described in [61] was applied to give an estimate of this ratio, and thereby quantifying the effects of radiation damage: Reference data obtained from manganese oxides (see figure 5.1) were corrected for the different photoionization cross section and then added up for a Mn^{III} content between 1 and zero. The **B**/**A** ratio as a function of the amount of Mn^{III} present was derived from the resulting 'artificial' spectra. The function $f(B/A) = Mn^{III}/(Mn^{III} + Mn^{II})$ allows the determination of the Mn^{III} content in $[\mathbf{Mn_6^{III}Cr^{III}}]^{3+}$ samples via the measured **B**/**A** peak ratio (see figure 5.7).

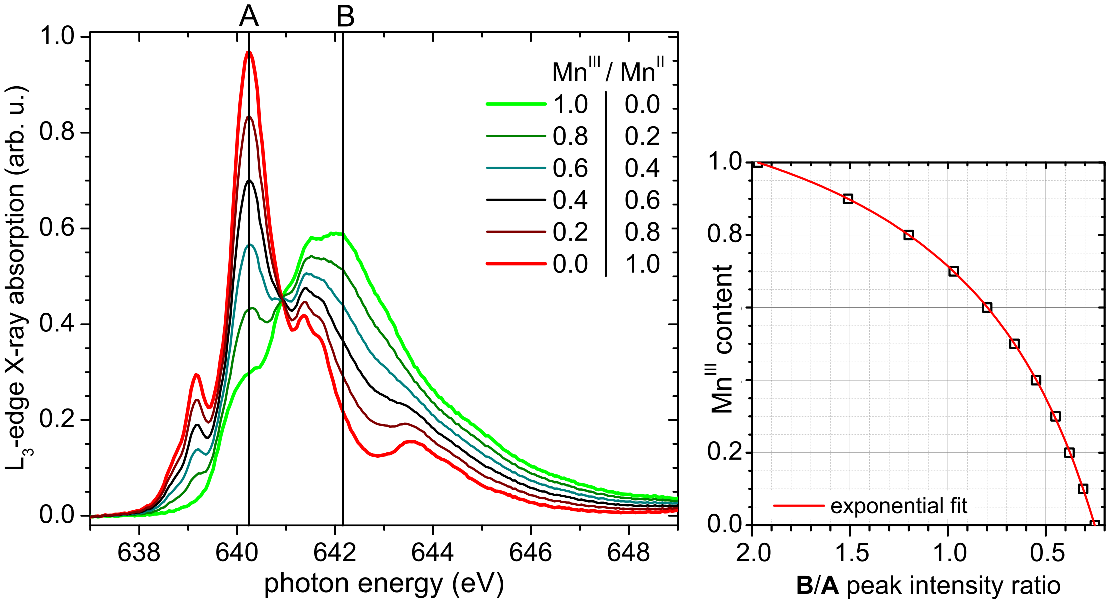

Figure 5.7. Left: Based on reference data obtained from manganese oxides, artificial absorption spectra for different $\mathrm{Mn^{III}}$ contents have been calculated. Right: The functional dependence between **B**/**A** peak ratio and $\mathrm{Mn^{III}}$ content obtained from the artificial spectra was used to determine the remaining fraction of $\mathrm{Mn^{III}}$ in the $[\mathbf{Mn_6^{III}Cr^{III}}]^{3+}$ samples.

5.2.1. Effect of anion choice

Sequences of XAS scans as described above have been recorded for all three SMM salts to detect a possible influence of the anion choice on the sensitivity of the $[\mathbf{Mn_6^{III}Cr^{III}}]^{3+}$ complex against soft X-ray exposure. The results obtained from $[\mathbf{Mn_6^{III}Cr^{III}}](C_3H_5O_3)_3$ (lactate anions) and $[\mathbf{Mn_6^{III}Cr^{III}}](ClO_4)_3$ (perchlorate anions) SMM are shown in figure 5.8. Correspondent XAS data for the $[\mathbf{Mn_6^{III}Cr^{III}}](BPh_4)_3$ SMM (tetraphenylborate anions) are given in figure 5.6 for comparison.

Due to the principles involved with synchrotron radiation generation, the intensity of the radiation cannot be regarded as constant during a whole sequence of XAS scans. The decreasing ring current as well as instrumental parameters like the selected exit slit width have an influence on the light intensity at the sample position. Therefore the exposure times given in figures 5.6 and 5.8 need to be converted to photon numbers, based on the beamline-specific relation between photon energy, ring current, exit slit setting and the resulting photon flux (see figure 3.4). The photon numbers given in figure 5.9 represent the total exposure until the manganese L_3 peak is reached, ensuring that not only the radiation exposure of the sample resulting from previous measurements is taken into account, but also the photons accumulated within the current scan up to the L_3 peak.

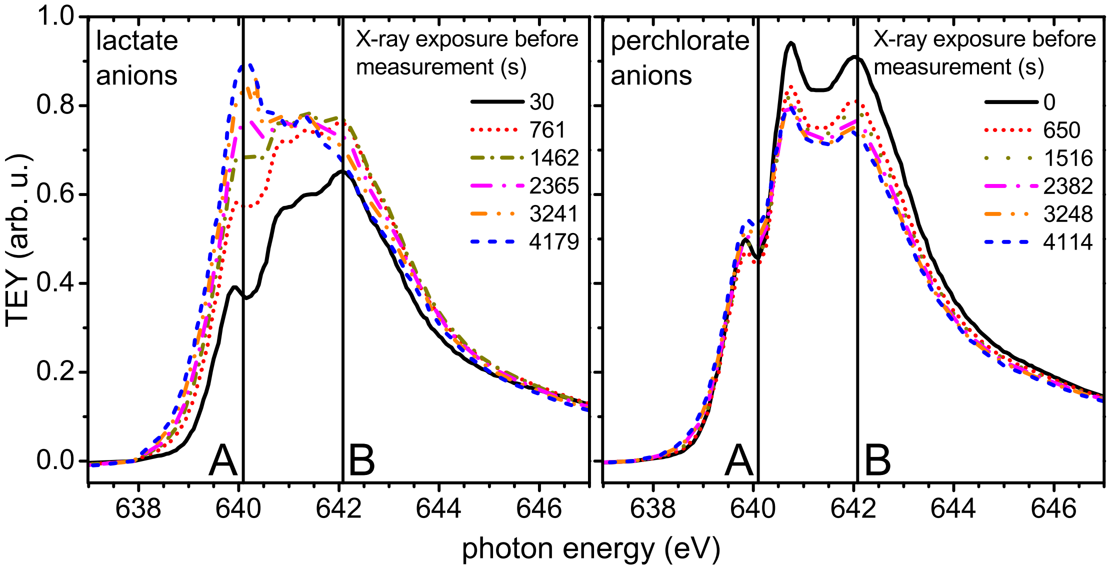

Figure 5.8. Selected Mn L_3-edge XAS spectra from a series of consecutive scans performed on a $[\mathbf{Mn}_6^{\mathbf{III}}\mathbf{Cr}^{\mathbf{III}}](C_3H_5O_3)_3$ sample (left) in comparison to results from $[\mathbf{Mn}_6^{\mathbf{III}}\mathbf{Cr}^{\mathbf{III}}](ClO_4)_3$ (right). Note the difference in the exposure-dependent changes of the L_3-edge absorption.

The three $[\mathbf{Mn}_6^{\mathbf{III}}\mathbf{Cr}^{\mathbf{III}}]^{3+}$ salts exhibit quite different properties with regard to their radiation sensitivity: While the rate of the radiation-induced reduction of the Mn^{III} centers to Mn^{II} in the SMM with lactate anions is comparable to the behavior found for $[\mathbf{Mn}_6^{\mathbf{III}}\mathbf{Cr}^{\mathbf{III}}]^{3+}$ with tetraphenylborate anions, the process happens significantly slower when perchlorate anions are used. This behavior is shown for all three salts in figure 5.9. The Mn^{III} content in $[\mathbf{Mn}_6^{\mathbf{III}}\mathbf{Cr}^{\mathbf{III}}](BPh_4)_3$ and $[\mathbf{Mn}_6^{\mathbf{III}}\mathbf{Cr}^{\mathbf{III}}](C_3H_5O_3)_3$ is reduced to 0.75 by a radiation exposure of $2.2 \cdot 10^{13}$ photons/mm^2 and $3.2 \cdot 10^{13}$ photons/mm^2, respectively. A comparable degree of reduction requires a radiation dose of $1.8 \cdot 10^{14}$ photons/mm^2 in the case of $[\mathbf{Mn}_6^{\mathbf{III}}\mathbf{Cr}^{\mathbf{III}}](ClO_4)_3$. This is equivalent to the acquistion of 7 (10) absorption spectra for $[\mathbf{Mn}_6^{\mathbf{III}}\mathbf{Cr}^{\mathbf{III}}]^{3+}$ with tetraphenylborate (lactate) anions, assuming that a single XAS measurement involves a radiation dose of approx. $3 \cdot 10^{12}$ photons/mm^2. A comparable degree of reduction will arise after approx. 60 XAS scans for $[\mathbf{Mn}_6^{\mathbf{III}}\mathbf{Cr}^{\mathbf{III}}](ClO_4)_3$ SMM.

The functional dependence between the accumulated soft X-ray exposure and the Mn^{III} fraction remaining in the SMM samples can be described by a fit function containing the sum of two exponential decays (blue lines in figure 5.9) with decay constants t_1 and t_2. The component described by t_1 is only present for low photon exposure, while t_2 governs the behavior for larger radiation exposure [61]. For the fit function used and the full set of fit parameters, see table 5.1.

It is striking that the differences in the radiation sensitivity of the investigated $[\mathbf{Mn}_6^{\mathbf{III}}\mathbf{Cr}^{\mathbf{III}}]^{3+}$ salts correlate with the redox properties of the different anions present in the $[\mathbf{Mn}_6^{\mathbf{III}}\mathbf{Cr}^{\mathbf{III}}]^{3+}$ SMM. Lactate [211] and tetraphenylborate [212] are known reducing agents, easily releasing

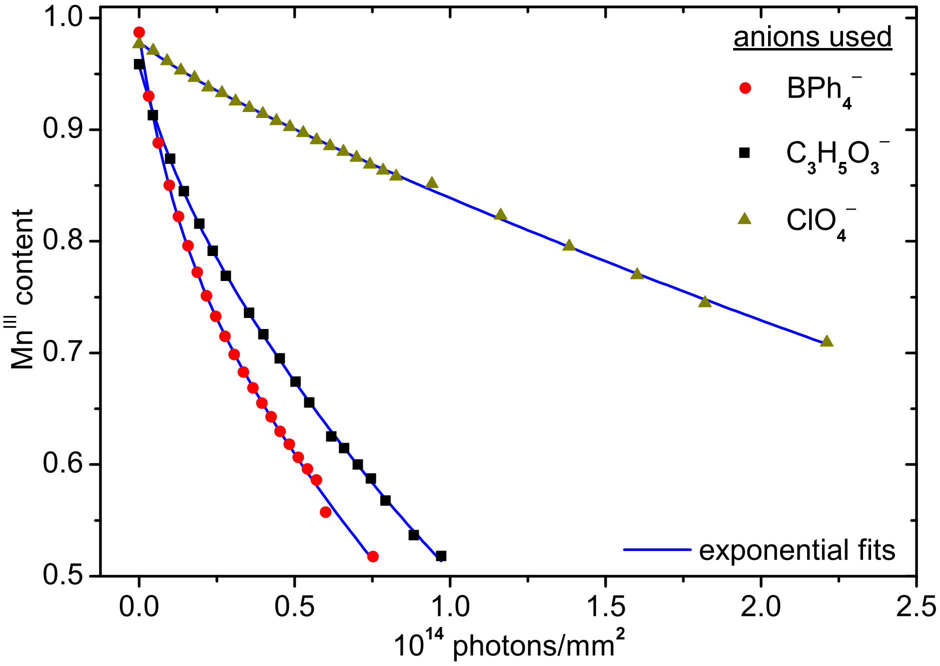

Figure 5.9. Decrease of the $\mathrm{Mn^{III}}$ fraction present in $\mathbf{[Mn_6^{III}Cr^{III}]^{3+}}$ SMM with radiation exposure for the three different anions (red: BPh_4^-, black: $C_3H_5O_3^-$, dark yellow: ClO_4^-) investigated [61]. Photon numbers have been calculated from the exposure times as described in the text. Blue lines represent exponential fits to the data, see table 5.1. Figure already published in [61].

	fit function: $y = A_1 \cdot \exp(\frac{-x}{t_1}) + A_2 \cdot \exp(\frac{-x}{t_2})$							
	fit parameter							
anion	A_1	ΔA_1	$t_1/10^{13}$	$\Delta t_1/10^{13}$	A_2	ΔA_2	$t_2/10^{13}$	$\Delta t_2/10^{13}$
BPh_4^-	0.13	0.01	1.02	0.10	0.85	0.01	15	0.44
$C_3H_5O_3^-$	0.06	0.005	1.15	0.17	0.90	0.005	17.4	0.24
ClO_4^-	0.01	0.002	1.74	0.53	0.96	0.002	71.4	0.71

Table 5.1. Fit function and resulting parameters describing the decrease of the $\mathrm{Mn^{III}}$ content in $\mathbf{[Mn_6^{III}Cr^{III}]^{3+}}$ SMM due to soft X-ray exposure [61].

electrons upon irradiation. This behavior mediates the reduction of $\mathrm{Mn}^{\mathrm{III}}$ to $\mathrm{Mn}^{\mathrm{II}}$ observed in the SMM samples. By contrast, perchlorate is a strong oxidant [213]. The reduction of metal centers in proteins, a common issue in protein crystallography [207, 209], can be attributed to the influence of a vast number of electrons released in the sample as well as in the underlying substrate either upon photon absorption (photoionization) or during secondary processes such as thermalization of higher energy Auger electrons [210]. It is assumed that these processes also play an important role in the radiation-induced reduction of the manganese centers in $\mathbf{[Mn_6^{III}Cr^{III}]^{3+}}$ SMM.

Radiation damage and photoreduction effects have been found for other types of single-molecule magnets as well – in the case of the widely known $\mathbf{Mn_{12}ac}$ [35, 50] the $\mathrm{Mn}^{\mathrm{III}}$ and $\mathrm{Mn}^{\mathrm{IV}}$ constituents are reduced to the $\mathrm{Mn}^{\mathrm{III}}$ and $\mathrm{Mn}^{\mathrm{II}}$ oxidation state upon soft X-ray exposure [125]. A comparable radiation-induced reduction of the metal centers is reported [214] for molecules like the 'ferric wheel' $\mathbf{NaFe_6}$ [215], the 'ferric star' $\mathbf{Fe_4}$ [216] and the 'manganese wheel' $\mathbf{Mn_7}$ [217, 218].

The solutions of the three different $\mathbf{[Mn_6^{III}Cr^{III}]^{3+}}$ salts exhibit significant differences in their deposition behavior (see section 3.2.1). Therefore the influence of the different sample morphology on the radiation stability has to be considered before attributing the observed effect solely to the anion choice.

The $\mathbf{[Mn_6^{III}Cr^{III}]}(\mathrm{ClO_4})_3$ salt (perchlorate anions) exhibits the highest stability against radiation exposure. It forms a dense layer of microcrystallites on the substrate surface upon preparation (see figure 3.6). The morphology of the samples obtained by drop-casting is quite different when a methanolic solution of $\mathbf{[Mn_6^{III}Cr^{III}]}(\mathrm{ClO_4})_3$ with a 5 times lower concentration of $9 \cdot 10^{-5}$ mol/l is used: The plain deposit layer with small scattered microcrystallite aggregations that now forms closely resembles the deposition behavior of the $\mathbf{[Mn_6^{III}Cr^{III}]^{3+}}$ salt with tetraphenylborate anions (see section 3.2.1). The radiation-induced decay of the $\mathrm{Mn}^{\mathrm{III}}$ content of two samples prepared and measured under comparable conditions, but using different $\mathbf{[Mn_6^{III}Cr^{III}]}(\mathrm{ClO_4})_3$ solution concentrations was investigated by XAS. An exponential fit of the data yields a decay constant of $(86 \pm 4) \cdot 10^{13}$ for the microcrystallite sample and a decay constant of $(89 \pm 2) \cdot 10^{13}$ for the thin deposit layer (see figure 5.10). No significant influence of the deposition behavior and the resulting sample morphology on the radiation stability could be observed, confirming the predominant role of the anion choice [61].

It has to be noted that both decay curves shown in figure 5.10 start considerably below the expected $\mathrm{Mn}^{\mathrm{III}}$ fraction of 1 at zero photon exposure. This is due to the detrimental effect of an ionization gauge that was operated in the load-lock of the UHV apparatus while handling these two samples, see section 5.1.3 for a more detailed explanation.

5.2.2. Substrate influence

The XAS exposure series described in section 5.2 have been repeated on different substrates in order to investigate a possible influence of the substrate on the radiation sensitivity of the

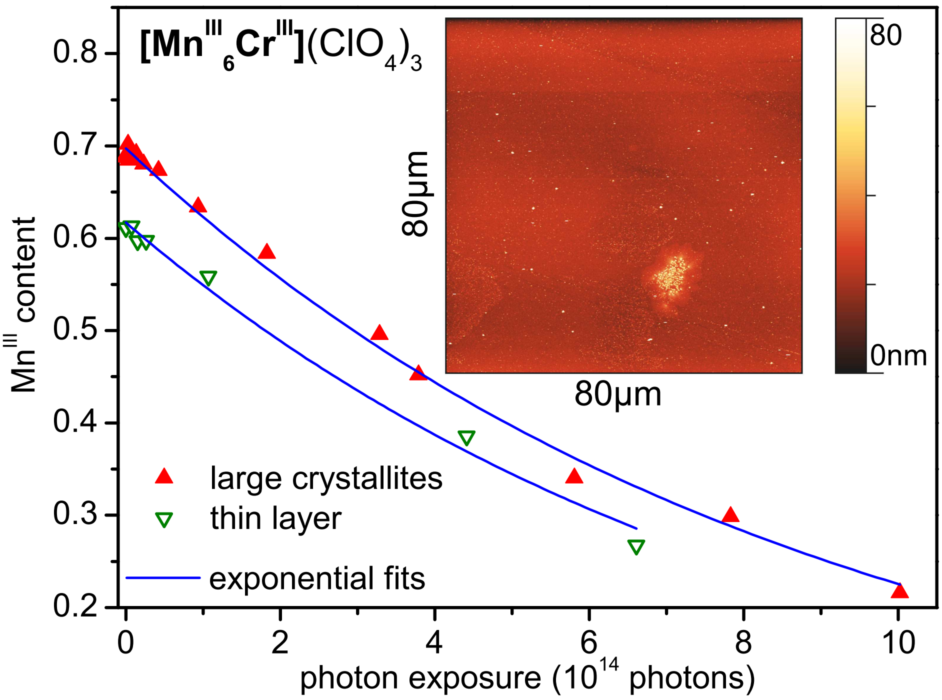

Figure 5.10. Comparison of the radiation-induced decrease of the Mn^{III} content in **[Mn$^{III}_6$Cr^{III}]**(ClO$_4$)$_3$ samples with different sample morphologies. Blue lines represent exponential fits to the data. Inset: AFM micrograph of a **[Mn$^{III}_6$Cr^{III}]**(ClO$_4$)$_3$ sample prepared using SMM solution with a very low concentration of $9 \cdot 10^{-5}$ mol/l, see figure 3.6 for comparison. Figure published in [61].

[Mn$^{III}_6$Cr^{III}]$^{3+}$ SMM. The **[Mn$^{III}_6$Cr^{III}]**(ClO$_4$)$_3$ salt was chosen and samples using gold, HOPG and silicon as substrate (see figure 3.5 right) were prepared by the drop-casting preparation method described in section 3.2.1.

The analysis of the subsequent XAS measurements performed on these samples (see figure 5.11) shows no discernible difference in the observed reduction process: No measurable influence of the substrate on the radiation sensitivity of **[Mn$^{III}_6$Cr^{III}]**(ClO$_4$)$_3$ could be observed for the choice of substrates investigated and the radiation doses applied [61].

However, although the results obtained are valid for different layer thicknesses of **[Mn$^{III}_6$Cr^{III}]**$^{3+}$ microcrystallite layers (see figures 3.6 and 5.10 for comparison), a different behavior might be expected for thin adsorbate layers down to the (sub)monolayer regime. Under these circumstances, the increasing importance of the molecule-substrate interaction which leads to reduction effects even without radiation exposure for **Mn$_{12}$ac** SMM [125, 199] has to be considered.

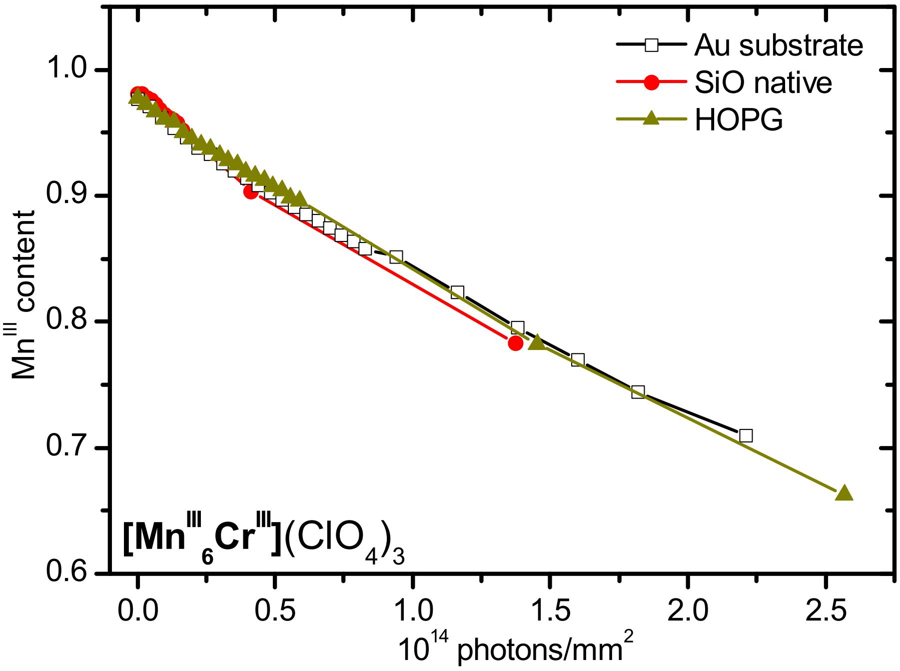

Figure 5.11. Exposure-dependent reduction of the Mn^{III} constituents in the $[\mathbf{Mn}^{\mathbf{III}}_{\mathbf{6}}\mathbf{Cr}^{\mathbf{III}}](ClO_4)_3$ SMM prepared on different substrates (see figure 3.5). No influence of the underlying substrate on the rate of the reduction process is found for the radiation doses used within the experiments presented here. Figure published in [61].

5.3. Electron spectroscopy of $[\mathbf{Mn}^{\mathbf{III}}_{\mathbf{6}}\mathbf{Cr}^{\mathbf{III}}]^{3+}$

Electron spectra of $[\mathbf{Mn}^{\mathbf{III}}_{\mathbf{6}}\mathbf{Cr}^{\mathbf{III}}](ClO_4)_3$ SMM after resonant Mn L_3-edge excitation have been obtained using the high resolution electron spectrometer (Scienta SES-200) installed in the front experimental chamber of the D1011 beamline at MAX-lab (see section 3.1.2). The $[\mathbf{Mn}^{\mathbf{III}}_{\mathbf{6}}\mathbf{Cr}^{\mathbf{III}}](ClO_4)_3$ salt was chosen for these measurements due to its higher stability against soft X-ray exposure. The XPS results shown here have been published in 2011, see ref. [186].

The left panel of figure 5.12 depicts the results obtained for the excitation energies 640.1 eV and 642 eV corresponding to the peak resonance for $2p \to 3d$ transitions in Mn^{II} and Mn^{III} ions [186], respectively. The right panel of the figure shows XAS data of the $[\mathbf{Mn}^{\mathbf{III}}_{\mathbf{6}}\mathbf{Cr}^{\mathbf{III}}](ClO_4)_3$ sample taken before the electron spectroscopy measurements for sample characterization purposes. Vertical lines labeled **A** and **B** mark the excitation energies mentioned before. The XAS multiplet structure of the Mn L_3 absorption edge clearly exhibits the characteristic features of Mn^{III} ions (see figure 5.1 for comparison), thereby confirming the predominance of the Mn oxidation state expected for non-reduced $[\mathbf{Mn}^{\mathbf{III}}_{\mathbf{6}}\mathbf{Cr}^{\mathbf{III}}]^{3+}$ SMM [38].

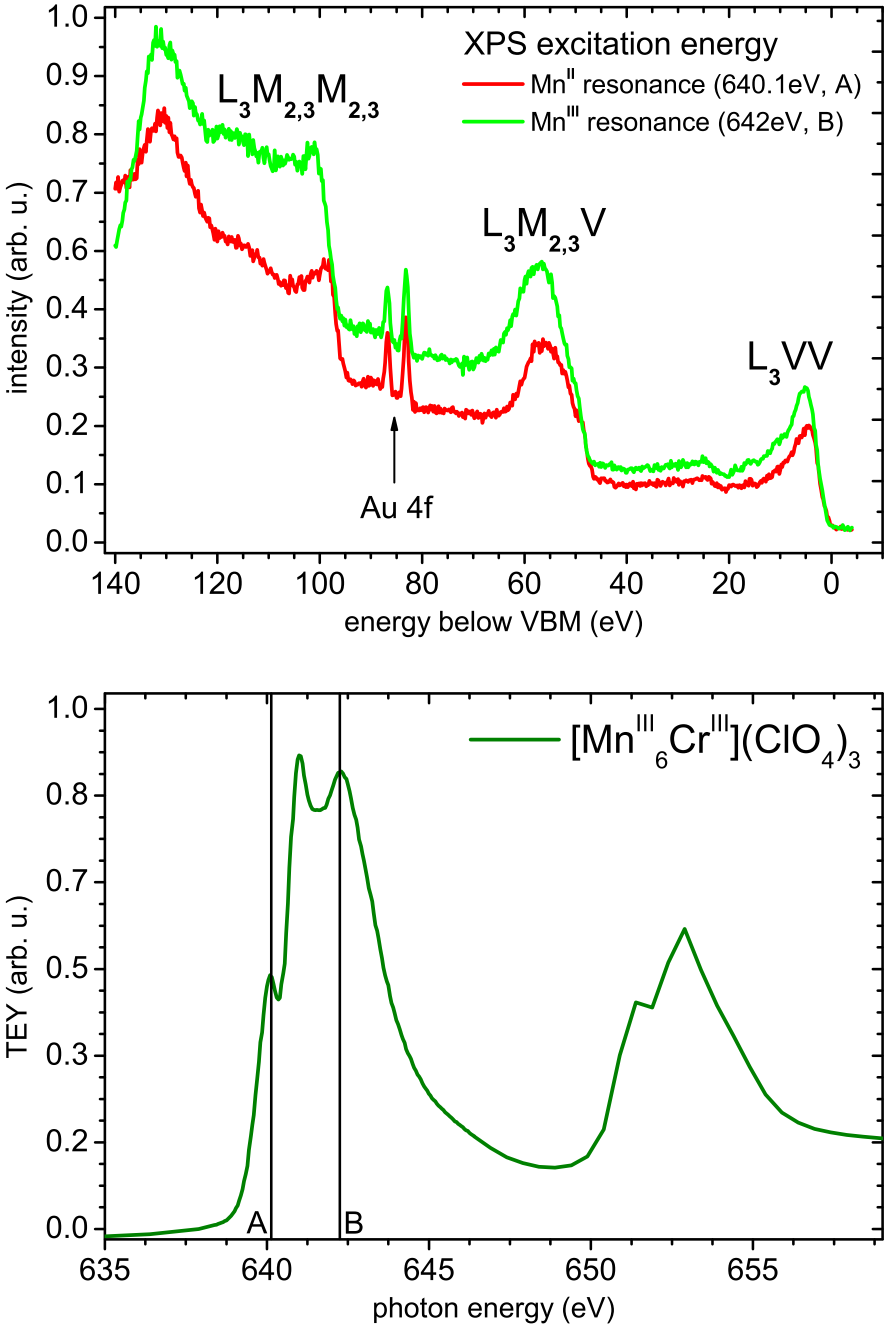

Figure 5.12. XPS results of a non-reduced $[\mathbf{Mn}_6^{\mathbf{III}}\mathbf{Cr}^{\mathbf{III}}](ClO_4)_3$ sample, already published in [186]. Top panel: XPS spectra after resonant excitation at the Mn^{II} and Mn^{III} L_3 main lines, respectively. For the identification of the different Auger groups shown, see text. The double line feature at a binding energy of 80-90 eV is caused by electrons emitted from the gold substrate. Bottom panel: X-ray absorption spectrum taken for sample characterization purposes before the XPS measurement. The characteristic spectral shape of Mn in the Mn^{III} oxidation state is clearly visible. Vertical lines mark the excitation energies used for the XPS measurement shown left.

The XPS data show three distinct features caused by resonant Auger decay of the primary $2p_{3/2}$ core hole: The spectral features related to the $L_3M_{2,3}M_{2,3}$, the $L_3M_{2,3}V$ and the L_3VV decay channels are identified following [219, 220]. The sharp double line feature in the 80-90 eV range is caused by photoemission from the spin-orbit split $4f$ core levels of the gold substrate used for the $[\mathbf{Mn_6^{III}Cr^{III}}](ClO_4)_3$ sample.

XPS results of a $[\mathbf{Mn_6^{III}Cr^{III}}](ClO_4)_3$ sample reduced due to X-ray exposure are shown in figure 5.13, along with a Mn L_3-edge XAS spectrum for characterization. Data obtained from iron [221] have been used for the assignment of the different Auger contributions in figure 5.13, as iron and manganese share the same Ar-like electron configuration with respect to their core levels involved in the transitions observed here. This composition of the $L_3M_{2,3}M_{2,3}$ Auger group is also found for arsenic [222] and selenium [223], again due to the same [Ar] core configuration.

The intensity difference found for the two electron spectra resonantly excited at the Mn^{II} (640.1 eV) and the Mn^{III} (642 eV) L_3-edges corresponds to the different absorption yield at the two photon energies obtained from XAS data (see bottom panel of figure 5.12, markings **A** and **B**).

The predominance of Mn^{II} in the reduced SMM sample is indicated by the distinct shape of the Mn L_3-edge with significantly increased absorption at 640.1 eV due to the sharp, prominent absorption maximum of Mn^{II} (see figure 5.1 for comparison). The shape of the two resonant XPS spectra corresponds to the changes observed in the absorption data: All three Auger groups are reduced in intensity for excitation at the Mn^{III} resonance. Especially the $^3P_{0,1,2}$ component of the $L_3M_{2,3}M_{2,3}$ Auger group is significantly diminished in comparison to the $^1S_0$ and $^1D_2$ contributions. In the case of resonant Mn^{II} excitation, all three Auger groups are present and appear more pronounced than before (see top panel of figure 5.12 for comparison).

5.4. SPES of reference materials

The application of spin-resolved electron spetroscopy necessitates long integration times and consequently an extended exposure of the sample to X-rays due to the limited detection efficiency of the Mott polarimeter: The count rate is reduced by approx. two orders of magnitude for the detectors in the Mott polarimeter compared to the auxiliary electron detector directly behind the spectrometer exit slit (see figure 4.3).

Therefore spin-resolved electron spectra have been obtained from Mn^{II} and Mn^{III} ions in radiation-stable reference materials to demonstrate their characteristic properties. Commercially available manganese oxides MnO (Mn^{II}) and Mn_2O_3 (Mn^{III}) were chosen due to their good availability and the simplicity of their preparation: The oxide powders were pressed into adhesive carbon tape. While Mn_2O_3 requires no further preparation steps, the MnO sample

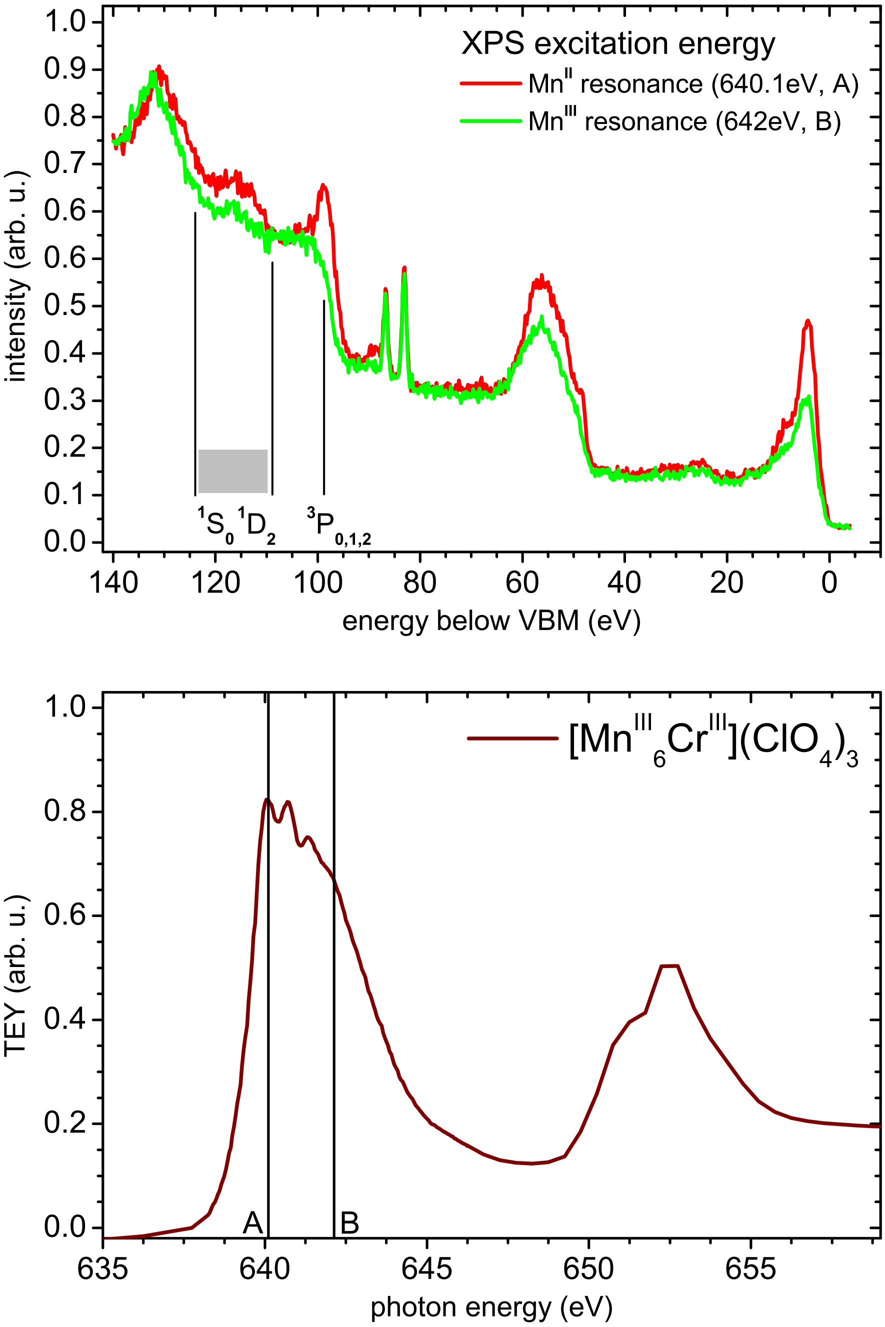

Figure 5.13. XPS and XAS results of a **[$\mathbf{Mn_6^{III}Cr^{III}}$]**$(ClO_4)_3$ sample with extensive reduction of the Mn centers due to X-ray exposure, already published in [186]. Top panel: XPS spectra after resonant excitation at the Mn^{II} and Mn^{III} L_3 absorption maxima. Identification of the given Auger line components is described in the text. Bottom panel: Corresponding XAS spectrum of the reduced **[$\mathbf{Mn_6^{III}Cr^{III}}$]**$(ClO_4)_3$ sample. The spectral shape of the Mn L_3 absorption clearly shows the presence of Mn^{II} (see figure 5.1 for comparison). Vertical lines show the XPS excitation energies as before.

has to be sputtered after transfer into vacuum, as the MnO particles get partly oxidized to $\mathrm{Mn^{III}}$ at their surface when exposed to atmospheric conditions [224]. Manganese$^{\mathrm{II}}$acetate as another reference material provides Mn ions in a molecular environment resembling the $\mathbf{[Mn_6^{III}Cr^{III}]^{3+}}$ SMM closer than bulk manganese oxides. The drop-casting technique described in detail within section 3.2.1 was used for the preparation of Manganese$^{\mathrm{II}}$acetate samples. Part of the presented results obtained from the Mn reference substances have been published already, see ref. [186].

5.4.1. Spin-resolved electron spectra

Resonant excitation by circularly polarized light in the corresponding absorption maxima (see markings **A**, **B** in figure 5.1) was used to record spin-resolved spectra from MnO and $\mathrm{Mn_2O_3}$. The *partial intensities* $I_\pm$ representing the number of electrons with spin parallel and antiparallel to the photon spin, respectively, are shown in figure 5.14. The partial intensities are calculated from the measured spin polarization P and the total intensity I according to the following relation:

$$I_\pm = \frac{1}{2} \cdot I(1 \pm P) \tag{5.2}$$

The background intensity resulting from inelastic scattering of electrons has been removed by applying a background subtraction to all partial intensity spectra shown within this work following the Tougaard formalism [225].

The use of circularly polarized synchrotron radiation leads to the creation of oriented $2p_{3/2}$ core hole states in the primary excitation process due to the spin-orbit interaction [147, 148]. This core hole orientation is reflected in the spin polarization of the emitted Auger electron due to spin-spin coupling [148, 226–228]. A singlet configuration of the resulting two-hole final state leads to a preferential spin direction of the emitted electrons antiparallel to the orientation of the primary $2p_{3/2}$ core hole.

One striking feature of both spectra in figure 5.14 is the sharp peak at the leading edge of the $\mathrm{L_3M_{2,3}M_{2,3}}$ Auger group at approx. 100 eV below VBM, exhibiting the opposite sign of the spin polarization with respect to the other lines shown. Being present for all $3d$ transition metals [229], it is connected to the $^3\mathrm{P}_{0,1,2}$ triplet configuration of the two-hole final state of the $\mathrm{L_3M_{2,3}M_{2,3}}$ Auger transition [221, 230].

The different sign of the spin polarization of the $^3\mathrm{P}_{0,1,2}$ contribution to the $\mathrm{L_3M_{2,3}M_{2,3}}$ Auger group with respect to the $\mathrm{L_3M_{2,3}V}$ and $\mathrm{L_3VV}$ Auger lines confirms the predominance of singlet coupling within the $\mathrm{L_3M_{2,3}V}$ Auger transition used for the investigation of the magnetic properties of $\mathbf{[Mn_6^{III}Cr^{III}]^{3+}}$. Although triplet contributions to these Auger lines exist, they have

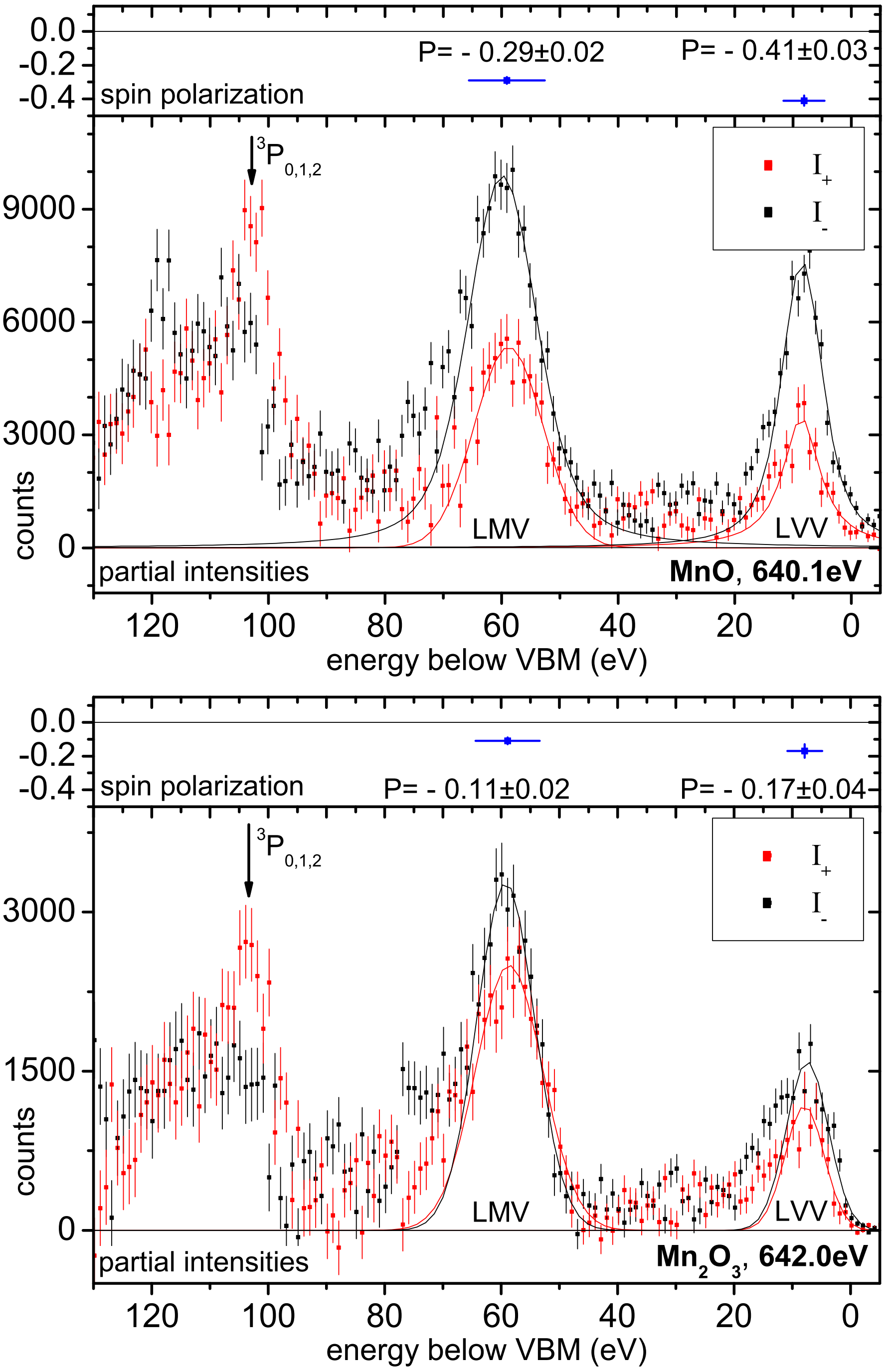

Figure 5.14. Spin-resolved electron spectra of MnO (top panel) and Mn_2O_3 (bottom panel) after resonant excitation in the respective absorption maximum (see markings **A** and **B** in figure 5.1). Shown are the partial intensities $I_\pm$ with the spin parallel and antiparallel to the light helicity, calculated as described in the text. The error bars represent the statistical error of the measurements. The spin polarization results have been averaged over the peak region as indicated by the horizontal error bars.

very low intensity [221] and are energetically separated from the dominating singlet part due to a different correlation energy of the two-hole state [221, 231, 232].

The I_- part is always preferred for the partial intensity spectra shown in figure 5.14, indicating an orientation of the primary $2p_{3/2}$ core hole parallel to the light helicity [186]. Spin-resolved Auger spectroscopy data obtained from Cr following resonant excitation with circularly polarized radiation [151] confirm this result. A detailed pointwise analysis shows that the measured spin polarization of the $L_3M_{2,3}V$ and L_3VV Auger lines scatters statistically around a mean value, indicating that no discernible triplet contributions with an opposite sign of the spin polarization are present. The spin polarization values indicated in figure 5.14 have been obtained by integrating the raw data over the full width half maximum (FWHM) of the Auger peaks. They have been corrected for the degree of circular polarization of the synchrotron radiation: The results shown in figure 5.14 correspond to a complete circular polarization of the incident light.

A remarkable difference is found between the spin polarizations obtained from the two different manganese oxides: For MnO the evaluated spin polarizations are $P = -0.29 \pm 0.02$ (LMV) and $P = -0.41 \pm 0.03$ (LVV). In the case of Mn_2O_3 the significantly lower values $P = -0.11 \pm 0.02$ (LMV) and $P = -0.17 \pm 0.04$ (LVV) occur.

If crystal field effects are neglected and approximately free ion behavior of the Mn centers is assumed, the differences in the spin polarization can be explained by the differences in the empty $3d$ valence states between Mn^{III} and Mn^{II}: The five valence electrons of Mn^{II} (term symbol $^6S_0$) represent a half-filled shell, resulting in a total spin of $S = 5/2$ due to Hund's rule. Therefore all empty $3d$ states available as final states in electronic transitions have identical spin orientation. The remaining four electrons of the $3d$ shell in the case of Mn^{III} add up to a total spin of $S = 4/2$ (term symbol ^5D_J, $J = 0, 1 \ldots 4$). Six empty $3d$ states are available, with one of them having a spin orientation antiparallel to the others.

Molecular orbital calculations performed for MnO and Mn_2O_3 (see [233]) reveal values of 1.4 eV and 2.4 eV, respectively for the crystal field splitting between the $3e_g$ and $2t_{2g}$ states. An exchange splitting of 4.5 eV (MnO) and 3.4 eV (Mn_2O_3) between spin up and spin down states has been calculated [234]. It has to be noted that Mn_2O_3 exhibits a measurable Jahn-Teller distortion, see [235].

Nevertheless MnO as well as Mn_2O_3 reveal a so-called high-spin configuration: Only $3e_g$ and $2t_{2g}$ states with identical spin orientation are occupied, leading to a good agreement of the experimental results with the simplified picture above assuming free Mn ions. The differences in the measured spin polarization can therefore be attributed to the differences in the empty $3d$ states of MnO and Mn_2O_3. The energy separation between the lowest unoccupied spin up and spin down states is approx. 1 eV for Mn_2O_3 [234], which is not resolved either in the primary excitation step or in the resulting Auger electron spectra.

Changing the photon energy of the primary excitation causes a remarkable change in the measured spin polarization for Manganese^{II}acetate: Instead of $P = -0.35 \pm 0.02$ (LMV) and

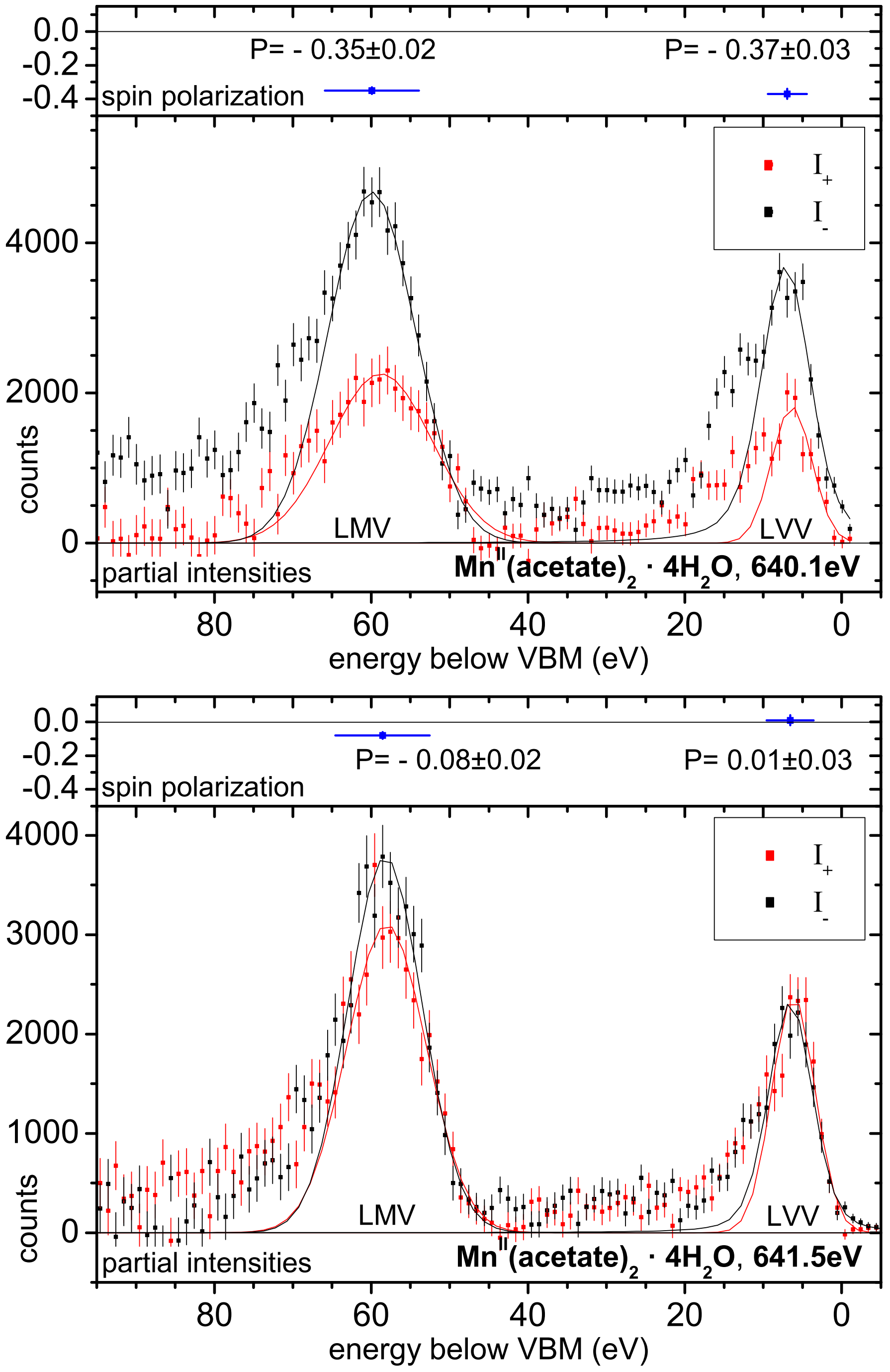

Figure 5.15. Spin-resolved electron spectra of Manganese^{II}acetate, shown are the partial intensities $I\pm$ calculated as described in the text. Top panel: A photon energy corresponding to the main Mn^{II} absorption peak at 640.1 eV (see figure 5.16, lower panel) was chosen for the primary excitation step. Bottom panel: Changing the excitation energy to the satellite absorption peak at 641.5 eV (see figure 5.16, lower panel) leads to a remarkable decrease in the measured spin polarization. The error bars and the calculation of the spin polarization values are described in figure 5.14.

$P = -0.37 \pm 0.03$ (LVV) obtained at an excitation energy of 640.1 eV, the values are decreased to $P = -0.08 \pm 0.02$ (LMV) and $P = 0.01 \pm 0.03$ (LVV) using an excitation energy of 641.5 eV (see figure 5.15). A corresponding change is found in XMCD asymmetry data obtained from $\mathrm{Mn^{II}}$ ions in a star-shaped $\mathrm{Mn_4^{II}O_6}$ molecule by Khanra *et al.* [186, 236]. The $\mathrm{Mn_4^{II}O_6}$ sample was magnetically aligned in an external field of 5 T and cooled down to approx. 5 K to obtain the helicity-dependent absorption data. While the XMCD data obtained by Khanra *et al.* [236] indicate a sign change of the XMCD asymmetry between the two photon energies, the spin polarization calculated from the spin-resolved electron spectra merely decreases to a small negative value. This is an effect of the large excitation bandwidth of 800 meV chosen for the measurements at 641.5 eV due to intensity reasons, see page 87 for a more detailed explanation.

The existence of a close connection between MCD effects in photoabsorption as well as in photoelectron angular distribution and the spin polarization of electrons emitted from unpolarized, paramagnetic atoms due to excitation with circularly polarized radiation has been described theoretically within an atomic theory in the electric dipole approximation [237]. Experimental proof has been given by Müller *et al.* in 2001, investigating the $4d \rightarrow 4f$ resonance in paramagnetic Gd [44] and comparing the spin-resolved photoemission results to MCD data obtained from magnetically oriented Gd below the Curie temperature [238].

Photoexcitation processes involving circularly polarized radiation are governed by the relativistic dipole selection rules [147, 188] for paramagnetic, magnetically non-ordered materials as well as for magnetically oriented samples [46]. Therefore the primary excitation step in both cases leads to the creation of oriented core holes. The core hole orientation can be retrieved by analyzing the spin polarization of Auger electrons resulting from the decay of the primary core hole as described above.

Performing an XMCD experiment with the light helicity set parallel or antiparallel to the sample magnetization M results in two different absorption yields [156] $Y^{\pm}$, with the positive sign denoting the case where the coupled spin and angular momentum is oriented parallel to M. The majority spin orientation of a magnetized sample is antiparallel to the magnetization M, therefore the empty $3d$ valence states available as final states are predominantly oriented parallel to M, leading to a situation where $Y^+ > Y^-$. The value of the so-called XMCD *asymmetry* (see section 3.3.2)

$$A_{\mathrm{XMCD}} = \frac{Y^+ - Y^-}{Y^+ + Y^-} \tag{5.3}$$

is closely related to the orientation of the core hole states created in a magnetically unordered sample by circularly polarized radiation. However, it has to be noted that this equivalency is restricted to experimental situations where the exchange splitting is not resolved spectroscopically in the MCD measurement [47]. Besides that restriction, the shifting of valence states and core level splitting by core-valence interactions occuring in magnetic materials [46] have to be taken into account.

5.4.2. Spin polarization results for Mn^{II}acetate

Each spin polarization measurement performed as described yields merely one single datapoint with respect to the aim of obtaining a complete MCD equivalent dataset, requiring repeated spin polarization measurements for different excitation energies covering the whole manganese $L_{2,3}$-edge region.

Instead of recording full spin-resolved spectra, a different method was applied in order to economize measuring time: A short SPES run was performed to locate the $L_{2,3}M_{2,3}V$ Auger line and the actual spin resolved measurement was done at a single electron energy corresponding to the Auger line. The results obtained from Manganese^{II}acetate are shown in the upper panel of figure 5.16, along with an absorption spectrum showing the selected excitation energies (lower panel).

An integration time of 300 s per helicity and datapoint was used. The energy bandwidth of the synchrotron radiation was chosen as a reasonable compromise between the resolution needed and the available electron yield, depending on the photon energy. The bandwidth is indicated by the horizontal error bars in figure 5.16, while the vertical error bars give the statistical error of the spin polarization measurements.

Mn^{II}acetate reveals a negative spin polarization in the L_3 region, followed by a sign change at the high energy edge of the L_3 multiplet. The highest positive polarization occurs at the 641.5 eV satellite structure being characteristic for Mn^{II} (see figures 5.1, top panel and 5.16, bottom panel). The distinct sign change between the main Mn^{II} absorption peak and the 641.5 eV satellite is also found for other molecular Mn^{II} compounds, see ref. [186, 236] for comparison.

The spin resolved spectra shown in section 5.4.1 do not exhibit this sign change due to the high excitation bandwidth chosen for the second measurement at 641.5 eV. The strong bandwidth dependence of the measured polarization in the vicinity of sharp XMCD asymmetry structures is also shown in figure 5.16: At an excitation energy of 641.6 eV, two different measurements with excitation bandwidths of 250 meV and 750 meV have been performed.

The last bandwidth was chosen to fit the spin-resolved spectra in section 5.4.1 and yields a polarization close to zero, being in reasonable agreement with the results calculated from the spin-resolved spectra. With decreasing excitation bandwidth, the measured spin polarization increases to approx. 12%, reproducing the sign change observed by Khanra *et al.* [236].

No significant spin polarization is measurable beyond the satellite structures at the high energy tail of the Mn L_3 absorption edge, extending up to 645 eV. For the Mn L_2 region between 649.5 eV and 654 eV, only small spin polarizations with an absolute value below 5% are found. It has to be noted that the spin polarization result obtained for an excitation energy of 640.1 eV in the first experiments (see figure 5.15) is noticeably higher than the results from later beamtimes as shown in figure 5.16. The polarization result from figure 5.15 is marked by a red square in figure 5.16 for comparison.

XMCD measurements have been performed in cooperation with the group of E. Goering (MPI für Intelligente Systeme, Stuttgart) on a Manganese^{II}acetate sample for comparison, see figure 5.16, top panel. XMCD and spin polarization results exhibit satisfactory qualitative agreement in and beyond the L_3-edge region up to the onset of the L_2-edge at 649.5 eV.

Within the L_2 absorption edge, the non-zero XMCD asymmetry differs noticeably from the measured spin polarization. Note the opposing sign of the two physical quantities as explained in section 5.4.1, which has been accounted for in the labeling of the vertical axis. Despite the qualitative agreement of both measurements, the absolute values differ by a scaling factor of approx. 3, probably due to incomplete magnetic ordering of the Manganese^{II}acetate sample in the applied external field during the XMCD measurements.

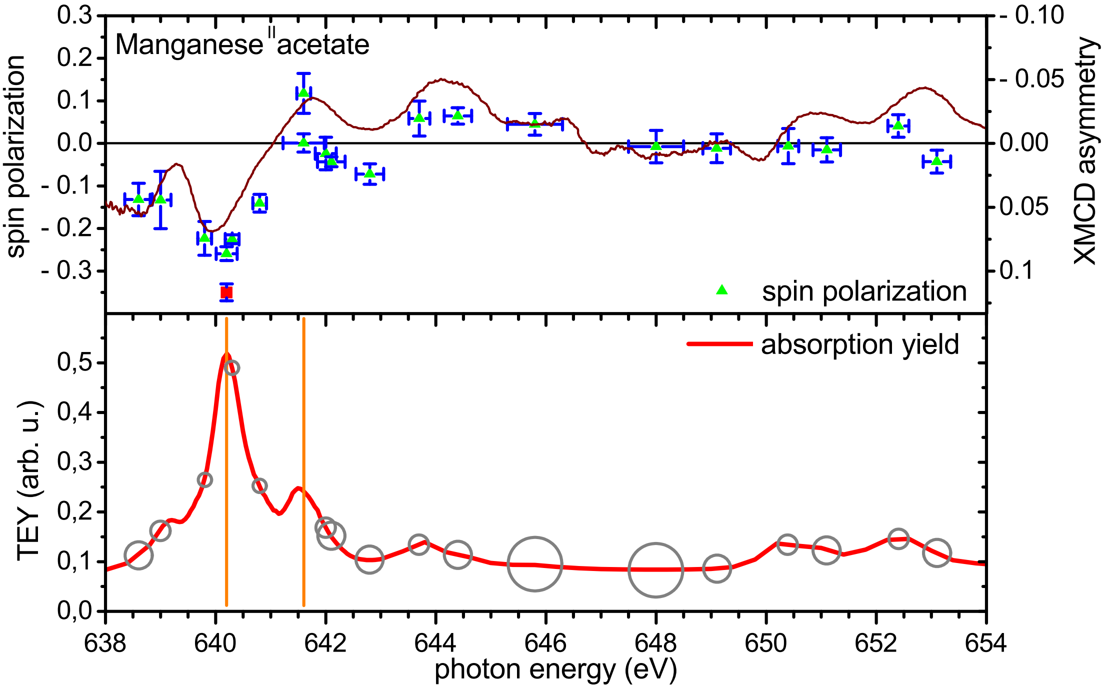

Figure 5.16. Upper panel: Spin polarization results obtained from Manganese^{II}acetate. Horizontal error bars indicate the excitation bandwidth, vertical error bars represent the statistical error of the measurements. XMCD data of Manganese^{II}acetate are shown for comparison (solid line). The red square indicates the polarization result from figure 5.15. Lower panel: Corresponding absorption spectrum of Manganese^{II}acetate, the excitation energies used for the spin polarization measurements in the top panel are marked by grey circles with a diameter corresponding to the excitation bandwidth. The excitation energies that have also been used for the spin-resolved spectra in figure 5.15 are marked by thick vertical lines (orange).

5.5. SPES results of $[\mathbf{Mn_6^{III}Cr^{III}}]^{3+}$ SMM

With respect to the high radiation sensitivity of the $[\mathbf{Mn_6^{III}Cr^{III}}]^{3+}$ SMM, the applicability of spin-resolved electron spectroscopy studies is severely limited by the short measuring times available before a non-acceptable degree of radiation damage occurs: XAS studies showed that a maximum exposure time of approx. 60 s was allowable to keep radiation damage effects within reasonable limits (see figure 5.17). Therefore, the following approach was chosen:

The $[\mathbf{Mn_6^{III}Cr^{III}}]^{3+}$ SMM were homogeneously deposited on large substrates using the method described in section 3.2.2. A new, previously unexposed sample position was selected after each datapoint using the motorized sample stage and the spin polarization result was averaged over a large number of sample positions. Slight differences in signal intensity due to $[\mathbf{Mn_6^{III}Cr^{III}}]^{3+}$ layer thickness variations cancel out, as only the ratio of the count rates of the two detectors is evaluated. Combining measurement runs with different helicity achieves a cancellation of instrument-related asymmetries.

An example of the raw data obtained from four subsequent sample positions is given in the top panel of figure 5.17. On each sample position, three datapoints with an exposure time of 20 s per point were recorded. The helicity of the synchrotron radiation was switched between the 2nd and the 3rd sample position. Despite the large statistical error (see error bars), the change in the count rate asymmetry between the two detection channels CT2 and CT4 due to the switching of the light helicity is visible. A large number of datapoints was taken into account to reduce the statistical error of the final spin polarization data.

A Mn-L_3 absorption spectrum showing the radiation damage caused by the 60 s synchrotron radiation exposure of the last used sample position (right hand side of the dashed vertical line) is given in the bottom panel of figure 5.17. While the $[\mathbf{Mn_6^{III}Cr^{III}}](ClO_4)_3$ sample reveals a Mn^{III}content of 0.93 without radiation exposure (black solid line), the radiation-induced reduction effects lead to a significantly lower Mn^{III} content of 0.78 after 60 s of irradiation (dark yellow solid line).

The SPES acquisition shown in figure 5.17 has been performed at the Mn^{III} absorption maximum at a photon energy of approx. 642 eV, giving a worst-case estimate of the radiation damage due to the large number of photoelectrons and secondary electrons created in the sample. Less radiation damage was observed for off-resonance excitation energies with a lower total absorption.

The spin polarization data obtained from $[\mathbf{Mn_6^{III}Cr^{III}}](ClO_4)_3$ samples for numerous excitation energies distributed over the whole Mn $L_{2,3}$-edge region is shown in figure 5.18, along with an absorption spectrum showing the selected excitation energies. XMCD data obtained from $[\mathbf{Mn_6^{III}Cr^{III}}](ClO_4)_3$ (see section 5.6) are shown for comparison. A predominantly negative spin polarization up to approx. −20% is found at the Mn L_3-edge.

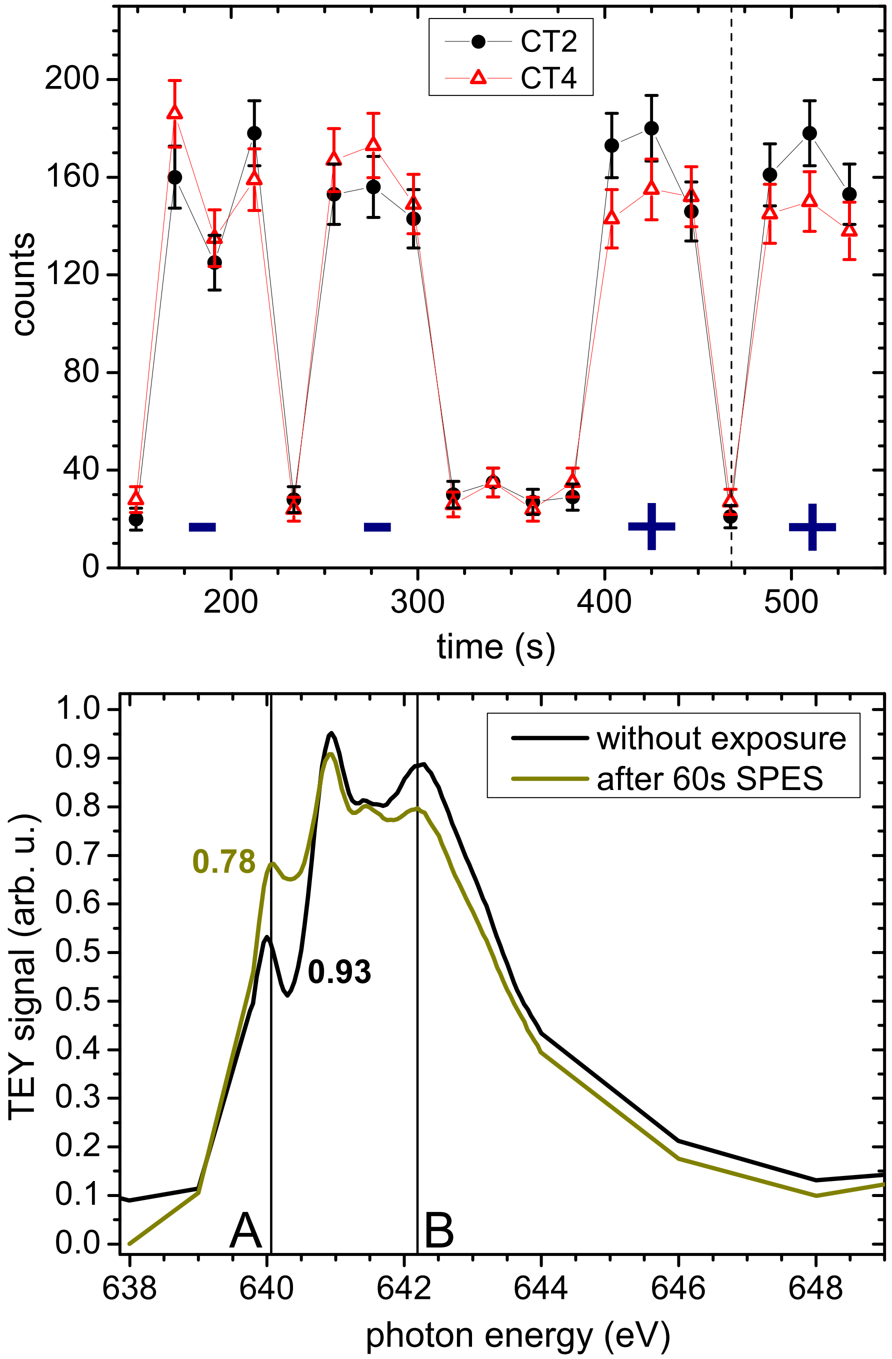

Figure 5.17. Top panel: Accumulated counts in the two detection channels CT2 and CT4 on four subsequent positions of a $[\mathbf{Mn_6^{III}Cr^{III}}](\mathrm{ClO_4})_3$ sample, each point represents 20 s integration time. The light helicity (indicated by the blue signs) is switched between the 2nd and 3rd sample position. Bottom panel: Radiation damage occuring to $[\mathbf{Mn_6^{III}Cr^{III}}](\mathrm{ClO_4})_3$ due to the radiation exposure of the 4th SPES acquisition (right hand side of the dashed vertical line in the left panel). Meaning of the markings **A** and **B** as before. The numbers next to the spectra represent the $\mathrm{Mn^{III}}$ content calculated from the **B**/**A** peak ratio.

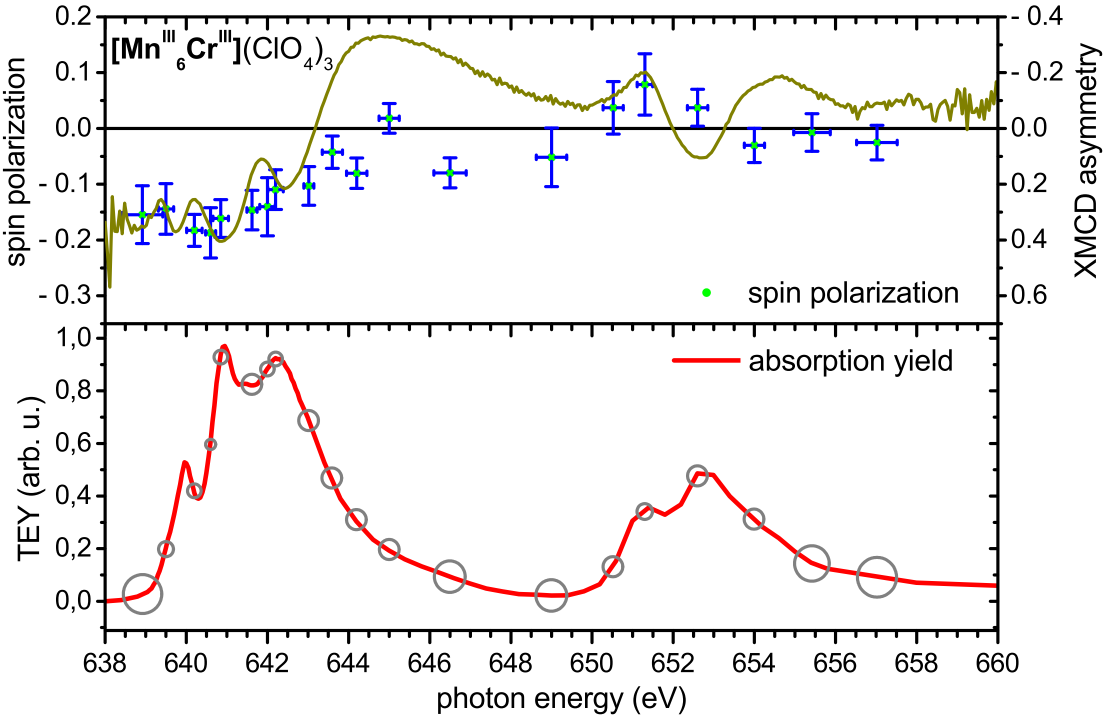

Figure 5.18. Upper panel: Spin polarization data obtained from $[\mathbf{Mn_6^{III}Cr^{III}}](ClO_4)_3$ at excitation energies in the Mn $L_{2,3}$-edge region. Error bars indicate the excitation bandwidth (horizontal) and the statistical error (vertical). The dark yellow curve represents XMCD data obtained from $[\mathbf{Mn_6^{III}Cr^{III}}](ClO_4)_3$ at an external magnetic field of 7 T and a temperature of approx. 2 K. Lower panel: Corresponding absorption spectrum of $[\mathbf{Mn_6^{III}Cr^{III}}](ClO_4)_3$, the excitation energies for the spin polarization measurements are marked by grey circles (diameter corresponding to the excitation bandwidth).

The spin polarization obtained for an excitation energy corresponding to the Mn^{III} absorption maximum at approx. 642 eV is in good agreement with the results obtained from bulk Mn^{III} oxide (see figure 5.14). In contrast to the data obtained from Manganese^{II}acetate (see figure 5.16), the polarization largely remains negative up to the onset of the L_2 multiplet, no distinct change of sign is observed in the high-energy tail of the L_3 multiplet. Positive polarizations up to +8% have been measured for the first peak structure of the L_2-edge.

Noticeable differences occur between these spin polarization results and the corresponding XMCD data: While a qualitative agreement is found for the Mn L_3 region, the sign changes of the XMCD signal at the high-energy edges of both the L_3 and the L_2 multiplet are not reproduced well in the spin polarization results. Besides, the absolute values of the XMCD asymmetry are approx. 3 times higher than the corresponding spin polarizations. This finding is in striking contrast to the results obtained from Manganese^{II}acetate and can not be explained by an incomplete saturation of the sample magnetization as before. Note that the left and right scales in the top panel of figure 5.18 are different to account for this difference. For a more detailed discussion of the observed differences see chapter 5.7.

Sum rule analysis of spin polarization data

Following the theoretical approach described in section 5.4.1, the spin polarization data shown in figure 5.18 contain information about the local magnetic moments of the Mn ions in $[\mathbf{Mn_6^{III}Cr^{III}}](ClO_4)_3$ equivalent to XMCD results. Therefore, a data analysis using the sum rule method (see section 3.3.2) has been performed to determine the spin and orbital magnetic moments μ_{spin} and μ_{orbit}.

A linear interpolation approach was chosen to obtain a full polarization curve from the discrete measurements shown in figure 5.18. The spin polarization was then multiplied pointwise by absorption data taken without external magnetic field to account for the difference between the intensity asymmetry $A = (I^+ - I^-)/(I^+ + I^-)$ obtained by SPES and the simple difference of the absorption yields $(Y^+ - Y^-)$ being used for the sum rule analysis [156–158]. The sign of the result was inverted to account for the effect of the singlet coupling of the Auger transition used to detect the primary core hole orientation, see page 82.

The resulting dataset is shown in the top panel of figure 5.19. Integration of both the obtained data and the spin-independent absorption spectrum according to the sum rule approach (see bottom panel of figure 5.19) leads to the following spin magnetic moment μ_{spin}:

$$\mu_{\text{spin}} = -\frac{(3p-2q)\cdot(10-n_{3\text{d}})}{r\cdot k_{\text{corr.}}} = -\frac{(3\cdot 15.26 - 2\cdot 14.02)\cdot 6}{91.69\cdot 0.6405}$$

$$= \mathbf{-1.8} \pm 0.40\ \mu_{\text{Bohr}}$$

A possible magnetic dipole contribution $<\mathrm{T_z}>$ has been neglected in the calculation of μ_{spin}, as this contribution is expected to be small for $3d$ transition metals (see [164] and section 3.3.2). A correction factor $k_{\text{corr.}}$ as described in section 3.3.3 has been applied to the spin magnetic moment, accounting for the special conditions present in $\mathrm{Mn^{III}}$ in contrast to other $3d$ transition metals [166, 167].

Any uncertainty within the spin polarization values leads to errors in the p and q integrals of the sum rule formalism. The influence of the spin polarization uncertainty on the final spin magnetic moment can not be determined using the common error propagation law (see [184, 185]) due to the integration step. Therefore the following method was applied to obtain the uncertainty of the spin magnetic moment μ_{spin}:

For each spin polarization datapoint, a set of n normal distributed random numbers with mean value 0 and standard deviation 1 was created. For each datapoint a random number from the corresponding set was multiplied with the spin polarization error of this datapoint.

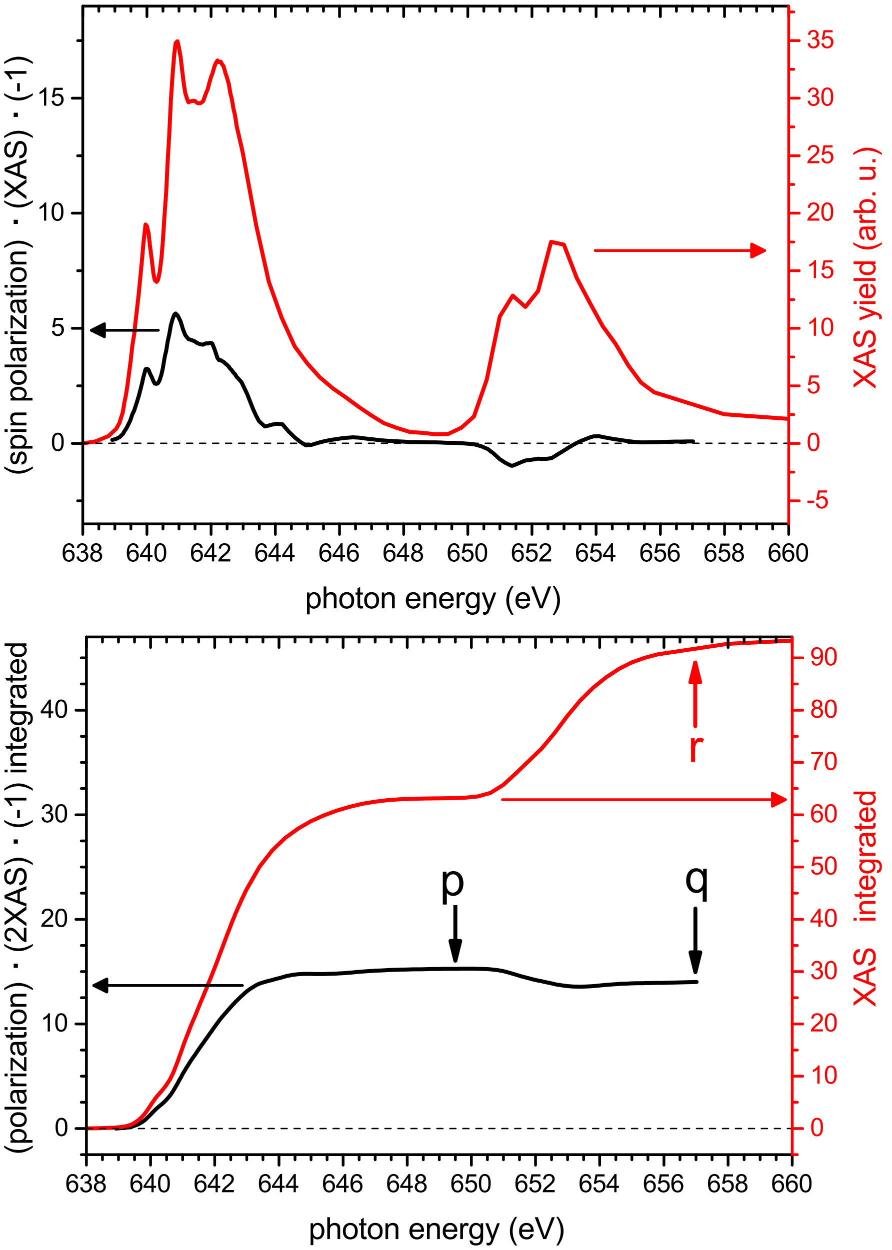

Figure 5.19. Determination of the Mn magnetic moments based on the measured spin polarization data. Top panel: Spin polarization data have been interpolated linearly and multiplied pointwise by absorption data (red) to obtain a curve equivalent to XMCD results (black). Bottom panel: The p, q and r parameters required for the sum rule analysis are obtained from the integrated polarization curve (black) and the integrated XAS spectrum (red). Note the different scale factor for red and black curves. The corresponding y-axis is indicated by the horizontal arrows.

A new spin polarization curve was generated by adding these errors to the original spin polarization data and sum rule evaluation was performed to obtain the spin magnetic moment.

By repeating these steps *n* times a set of *n* results for the spin magnetic moment is obtained, reflecting the influence of spin polarization errors on the final result. Finally the standard deviation of these results was determined to obtain the uncertainty for μ_{spin}. The error shown above was derived from 2000 runs of the described algorithm.

The orbital magnetic moment μ_{orbit} is derived from the full $L_{2,3}$ integral of the XMCD signal via the second sum rule (see [156] and section 3.3.2). Based on the spin polarization measurements, the following result was obtained for μ_{orbit}, with the given uncertainty being derived using the algorithm described above:

$$\mu_{\text{orbit}} = -\frac{2 \cdot q \cdot (10 - n_{3\text{d}})}{3 \cdot r} = -\frac{2 \cdot 14.02 \cdot 6}{3 \cdot 91.69}$$

$$= \mathbf{-0.6} \pm 0.1\ \mu_{\text{Bohr}}$$

A discussion of the spin and orbital magnetic moments μ_{spin} and μ_{orbit} of the Mn centers in $[\mathbf{Mn_6^{III}Cr^{III}}]^{3+}$ derived from the spin polarization measurements will follow in section 5.7, including a comparison with data obtained by XMCD.

5.6. XMCD of $[\mathbf{Mn_6^{III}Cr^{III}}]^{3+}$ SMM

XMCD measurements of $[\mathbf{Mn_6^{III}Cr^{III}}](ClO_4)_3$ have been performed for comparison, using the TBT endstation (7T, 2K, IPCMS Strasbourg) in cooperation with Dr. K. Kuepper (University of Osnabrück). To account for the known radiation sensitivity of the $[\mathbf{Mn_6^{III}Cr^{III}}]^{3+}$ SMM, the PGM monochromator was detuned to a high fix-focus constant $c_{ff} \simeq 20$ and an additional Al filter was introduced into the synchrotron radiation beam to lower the intensity.

A series of consecutive XAS scans was recorded to estimate the influence of radiation damage during the XMCD acquisition. During these scans, the monochromator exit slit was set to 20 μm to give a worst-case estimate while the XMCD measurements have been performed using an exit slit setting of 10 μm. The results of the radiation damage tests are shown in figure 5.20.

XMCD measurements were performed at a magnetic field of 6.9 T and a sample temperature of approx. 2 K. For each helicity, three spectra have been averaged to obtain the final helicity-dependent Mn $L_{2,3}$-edge spectra shown in figure 5.21. At the Cr $L_{2,3}$-edge (see figure 5.22), five spectra were averaged due to the low signal-to-noise ratio present in the Cr measurements.

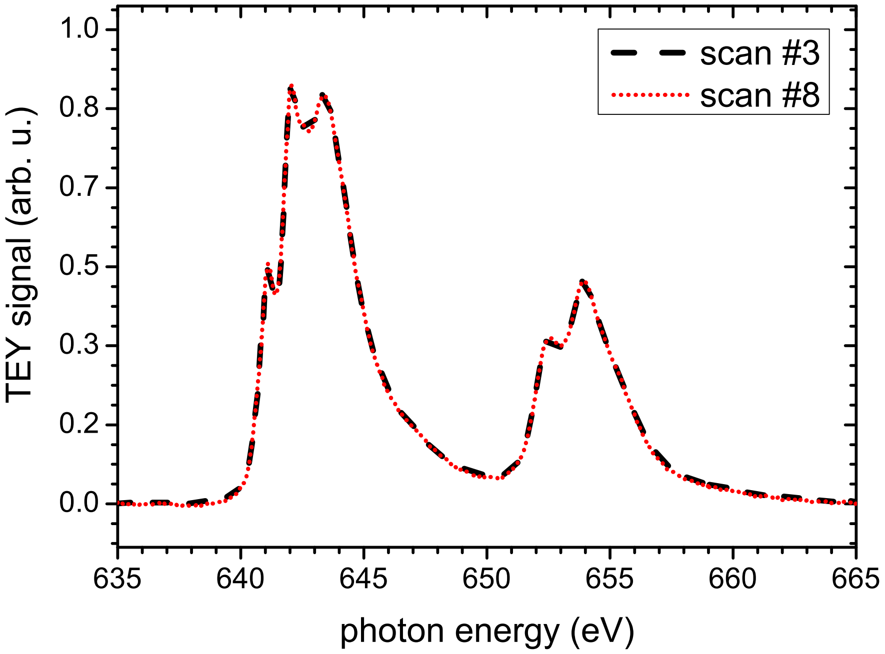

Figure 5.20. XAS spectra of a $[\mathbf{Mn_6^{III}Cr^{III}}](ClO_4)_3$ sample at the Mn $L_{2,3}$-edge showing the effect of radiation exposure in the XMCD measurement setup. Six scans (scan no. 3 to scan n. 8) have been performed on a previously non-irradiated sample position with an exit slit setting of 20 μm. No discernible radiation damage effects were observed for the exposure time and radiation dose corresponding to six XAS scans.

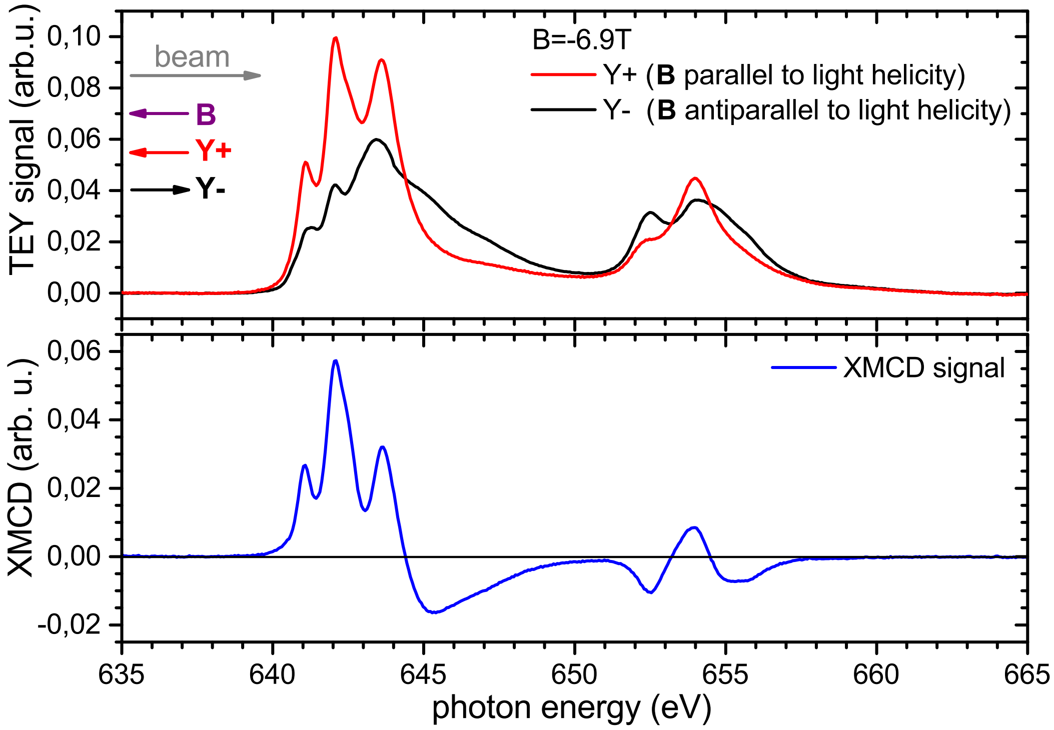

Figure 5.21. XMCD measurements performed at the Mn $L_{2,3}$-edge on a $[\mathbf{Mn_6^{III}Cr^{III}}](ClO_4)_3$ sample at approx. 2 K and a magnetic field of 6.9 T. Top panel: The absorption spectra for circularly polarized light with the helicity parallel (red) and antiparallel (black) to the magnetic field are shown. Bottom panel: XMCD signal calculated from the two absorption spectra. Note the opposite sign of the XMCD signal compared to the spin polarization measurements (see figure 5.18).

A prominent XMCD effect is visible on both the Mn $L_{2,3}$ and the Cr $L_{2,3}$ absorption edge. A comparison of the XMCD difference signals of the Mn and the Cr constituents (see lower panel of figures 5.21 and 5.22) shows opposite signs of the XMCD effect at both absorption edges, confirming the antiparallel orientation of the Mn and Cr magnetic moments expected from the intramolecular coupling scheme for Mn and Cr (see section 2.2).

A quantitative analysis of the XMCD results using the sum rules as described in section 5.5 was performed, the XMCD integrals are shown in figure 5.23. The analysis yields the following spin and orbital magnetic moments μ_{spin} and μ_{orbit}:

$$\mu_{\text{spin}} = -\frac{(3p-2q)\cdot(10-n_{3\text{d}})}{r\cdot k_{\text{corr.}}} = -\frac{(3\cdot 0.053-2\cdot 0.033)\cdot 6}{0.46\cdot 0.6405}$$

$$= \mathbf{-1.9}\pm 0.2\ \mu_{\text{Bohr}}$$

$$\mu_{\text{orbit}} = -\frac{2\cdot q\cdot(10-n_{3\text{d}})}{3\cdot r} = -\frac{2\cdot 0.033\cdot 6}{3\cdot 0.46}$$

$$= -\mathbf{0.3}\pm 0.03\ \mu_{\text{Bohr}}$$

The error of the obtained spin and orbital magnetic moments μ_{spin} and μ_{orbit} were derived following the approach described for the evaluation of the spin polarization measurements: The standard deviation of the three XAS scans performed for each helicity was used to obtain an estimate for the error of the XMCD difference datapoints. These datapoints were then varied as described on page 94 to derive the error of the final results from the XMCD difference error.

As mentioned before, a correction factor has been applied to the spin magnetic moment, see section 3.3.3. Note that the XMCD signal exhibits an opposite sign compared to the

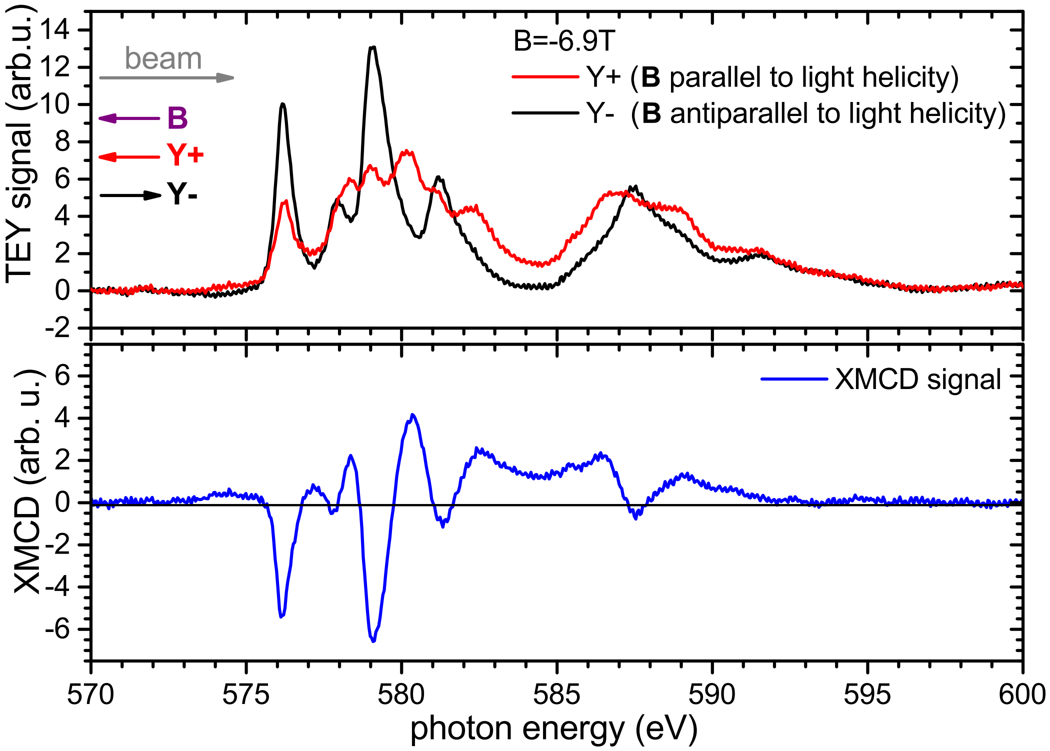

Figure 5.22. XMCD measurements of $[\mathbf{Mn_6^{III}Cr^{III}}](\text{ClO}_4)_3$ at the Cr $L_{2,3}$-edge performed at 2 K and 6.9 T. Top panel: XAS spectra for the two opposite helicities. Bottom panel: XMCD signal calculated from the absorption spectra. Characteristic spectral features within the L_2 edge as well as the prominent peaks of the L_3 edge exhibit a sign of the XMCD effect opposite to the one of the Mn ions (see figure 5.21), confirming the antiparallel orientation of the Mn and Cr magnetic moments, see section 2.2.

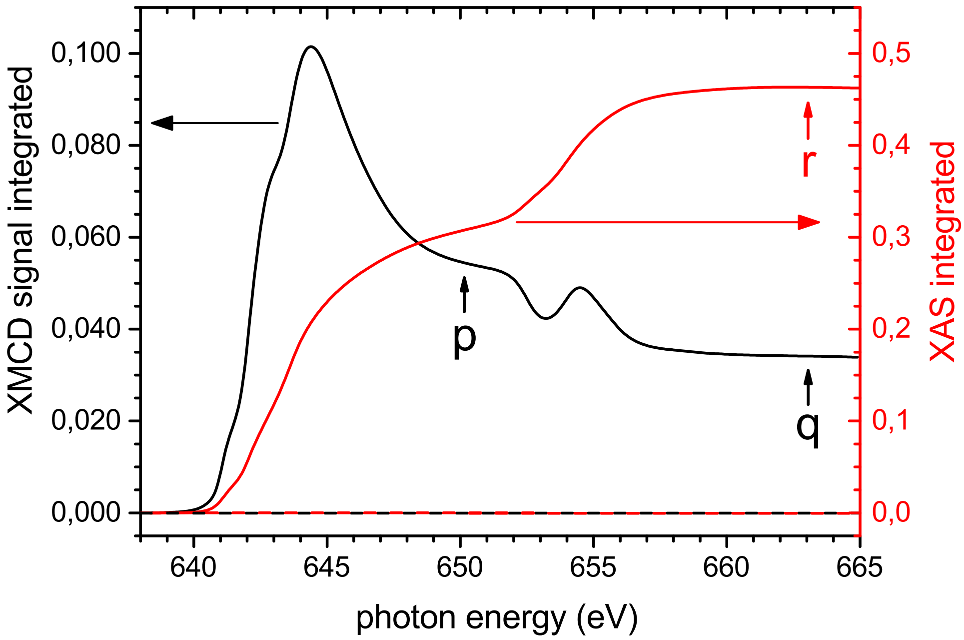

Figure 5.23. Integration of the XMCD difference signal and an averaged XAS spectrum obtained from a $[\mathbf{Mn}_6^{\mathbf{III}}\mathbf{Cr}^{\mathbf{III}}](ClO_4)_3$ SMM sample, yielding the parameters **p**, **q** and **r** needed for the sum rule analysis.

measurement of the spin polarization, as predicted from the singlet coupling of the Auger process involved. For the calculation of the XMCD, the sign convention XMCD=(Y^+ - Y^-) was chosen corresponding to equation 5.3, with Y^+ (Y^-) representing the situation with the light helicity parallel (antiparallel) to the magnetization direction.

A quantitative analysis of the Cr $L_{2,3}$-edge XMCD was not performed due to the limited signal quality: Although the XMCD effect is clearly visible at the Cr $L_{2,3}$-edge (see figure 5.22), a separation of the L_2 and L_3 contributions which is essential for the sum rule evaluation could not be performed due to the overlap between the two edges.

5.7. Discussion of SPES and XMCD results

While there are obvious differences in the orbital magnetic moment μ_{orbit} of the Mn^{III} ions in $[\mathbf{Mn}_6^{\mathbf{III}}\mathbf{Cr}^{\mathbf{III}}]^{3+}$ measured either by SPES or XMCD, the spin magnetic moment μ_{spin} derived from both methods via sum rule analysis is in good agreement. However, comparing the spin polarization results with the XMCD signal yields significant differences that will be discussed in the following section, along with a possible reason for the discrepancy.

5.7.1. Comparison: SPES asymmetry and XMCD difference

As both values for the spin magnetic moment μ_{spin} obtained in sections 5.5 and 5.6 have been determined via the sum rule approach involving integrals over the Mn L-edge, 'local' discrepancies between the two physical quantities spin polarization and XMCD signal can occur without being noticeable in the final result. The XMCD signal at 2 K and 6.9 T and the spin polarization (multiplied by XAS data for normalization) have been plotted for comparison, see figure 5.24.

Around the main features of the Mn-L_3 absorption edge, the XMCD difference gives significantly larger absolute values than the spin polarization measurement, though the overall structure with three peaks at 640 eV, 641 eV and slightly above 642 eV is comparable. At the high energy tail of the L_3 absorption edge, a sign change followed by a large positive swing up to the onset of the L_2 edge is found in the XMCD difference signal. The spin polarization remains negative at much smaller absolute values up to the L_2 edge, resulting in comparable **p** integrals of the sum rule analysis. The XMCD difference signal again shows a larger positive swing than the spin polarization at the Mn-L_2 edge, accompanied by a relatively prominent mininum not found in the spin polarization data. Due to this spectral shape, both methods yield comparable results using the integral-based sum rule analysis despite the differences between the two datasets.

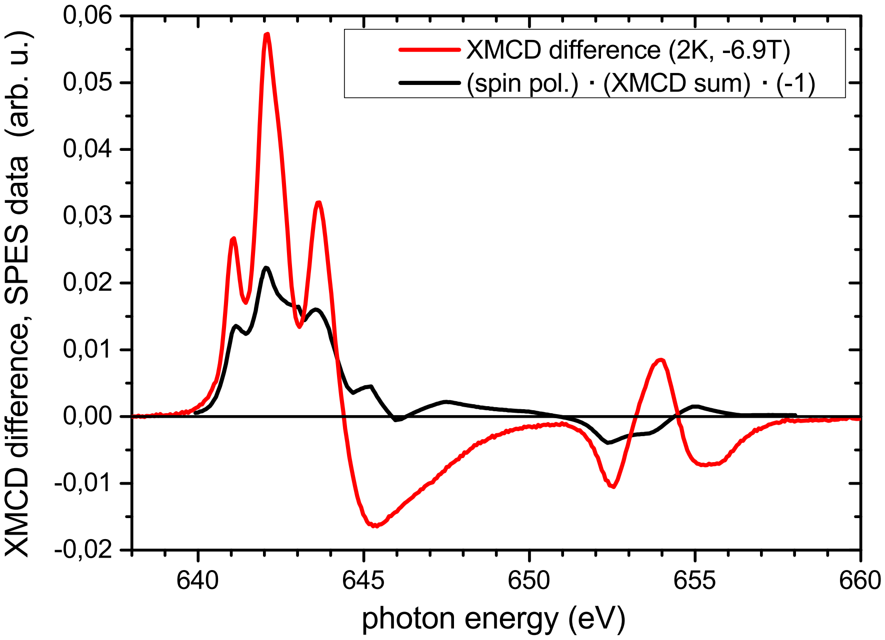

Figure 5.24. Comparison of XMCD difference (red) and spin polarization data multiplied by XAS intensity (black). Note the remarkably higher absolute values of the XMCD difference at the Mn-L_3 edge. In the sum rule analysis, this is compensated by the large positive swing at the high-energy tail of the L_3-edge, leading to similar values for the difference between the **p** (L_3 only) and **q** ($L_{2,3}$) integrals.

Although a good agreement of the spin magnetic moments obtained by either XMCD or spin-resolved electron spectroscopy is found, the result is significantly lower than the value theoretically expected from the coupling scheme and determined by AC and DC magnetometry [40].

It has been shown [39, 40] that the occupation of the 6th coordination site of the $\mathrm{Mn^{III}}$ions in $\mathbf{[Mn_6^{III}Cr^{III}]^{3+}}$ has a strong influence on the magnetic behaviour: This site has a very flat potential [39] for the coordination of a solvent molecule and its occupation influences the Mn–N distance and thereby the effective exchange coupling [39]. Magnetization studies of vacuum dried samples [40] reveal an increase of the effective coupling constant due to the loss of solvent molecules.

However, this mechanism does only influence the magnetic behaviour of the whole system via the the bond lengths and the effective exchange coupling. With the SPES and XMCD methods probing solely the *local* magnetic properties of the $\mathrm{Mn^{III}}$ ions, the occupation of the 6th coordination site of $\mathrm{Mn^{III}}$ in $\mathbf{[Mn_6^{III}Cr^{III}]^{3+}}$ does not explain the observed differences.

The small energetic separation of the $S_t = 21/2$ spin ground state of the $\mathbf{[Mn_6^{III}Cr^{III}]^{3+}}$ SMM [38, 40] is expected to play a significant role instead, as the first excited states corresponding to $S_t = 19/2$ are separated from the spin ground state by only a few wavenumbers (approx 2.6 $\mathrm{cm^{-1}}$, see [38].)

5.7.2. Influence of the external magnetic field

The $\mathbf{[Mn_6^{III}Cr^{III}]^{3+}}$ sample is subjected to various external influences during preparation and measurement (see sections 5.1 and 5.2). With respect to these experimental conditions, two major differences exist between spin polarization and XMCD:

- **Temperature.** While spin polarization measurements were performed at room temperature, the $\mathbf{[Mn_6^{III}Cr^{III}]^{3+}}$ sample was cooled down to approx. 2 K for the XMCD experiment.

- **Magnetic field.** The underlying principle of XMCD measurements (see section 3.3.2) requires the sample to be magnetized to saturation. The $\mathbf{[Mn_6^{III}Cr^{III}]}(\mathrm{ClO_4})_3$ sample under investigation was magnetized by a field of approx. 7 T. The spin polarization measurements were performed without external fields applied.

XAS measurements were performed on $\mathbf{[Mn_6^{III}Cr^{III}]^{3+}}$ with and without external magnetic field and at different sample temperatures (see figure 5.25) to investigate the role of these influences.

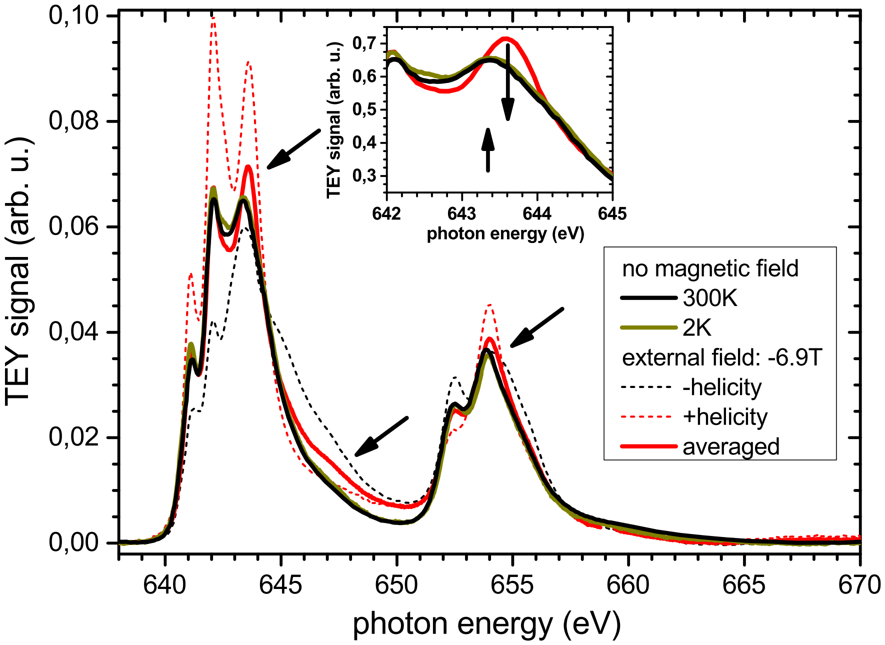

Figure 5.25. Mn $L_{2,3}$-edge XAS spectra of **[$Mn_6^{III}Cr^{III}$]**$(ClO_4)_3$ showing the influence of temperature and magnetic field associated with XMCD measurements. Note the differences due to the magnetic field marked by arrows.

A very good agreement is found between XAS data obtained at MAX-lab (beamline D1011, see section 3.1.2) at room temperature (black) and a corresponding XAS spectrum at the 2 K operating temperature of the XMCD setup at SLS (see section 3.1.2). Two spectra obtained with circularly polarized light of opposite helicity have been averaged to derive XAS data including the influence of the 7 T magnetic field used during the XMCD measurements (red). Distinct differences occur in this case: The absorption maximum associated with the Mn^{III} L_3-edge (leftmost arrow) appears higher with respect to other spectral features and is shifted upwards by approx. 300 meV. A significantly higher absorption is also found in the high-energy tail region of the L_3 multiplet structure, extending right up to the onset of the L_2 peak.

It is notable that the differences occuring in the absorption spectra between the Mn L_3-edge due to the magnetic field correspond with one of the most striking differences found in the comparison between spin polarization data and XMCD, see figure 5.24: The large positive swing of the XMCD signal between the Mn L_2 and L_3 absorption edges is not reproduced by the spin polarization data. A non-negligible modification of the electronic structure of the Mn^{III} ions in **[$Mn_6^{III}Cr^{III}$]**$^{3+}$ due to the strong external magnetic field has to be assumed.

6. Summary and Conclusion

$[\mathbf{Mn_6^{III}Cr^{III}}]^{3+}$ single-molecule magnets deposited on various substrates have been investigated by X-ray absorption spectroscopy, X-ray magnetic circular dichroism and spin-resolved electron spectroscopy.

XAS sample characterization proved that the deposition of $[\mathbf{Mn_6^{III}Cr^{III}}]^{3+}$ SMM on surfaces in the monolayer regime is feasible without the pronounced reduction effects known from $\mathbf{Mn_{12}ac}$. No discernible difference in the manganese oxidation state is observed between $[\mathbf{Mn_6^{III}Cr^{III}}]^{3+}$ deposits with a layer thickness in the μm range and samples with (sub-)monolayer coverage of $[\mathbf{Mn_6^{III}Cr^{III}}]^{3+}$ molecules.

No detrimental impact of atmospheric moisture or oxygen-induced solvent aging on the condition of the $[\mathbf{Mn_6^{III}Cr^{III}}]^{3+}$ SMM could be observed. However, the operation of a ionization vacuum gauge in the load-lock during pump-down leads to a significant reduction of the $\mathrm{Mn^{III}}$ ions in $[\mathbf{Mn_6^{III}Cr^{III}}]^{3+}$. The effect is expected to originate from interaction with excited, metastable neutral gas atoms created by the gauge in the residual gas ionization process.

Radiation-induced reduction effects have been observed upon soft X-ray exposure of all $[\mathbf{Mn_6^{III}Cr^{III}}]^{3+}$ SMM samples. The radiation exposure causes a progressive change in the manganese oxidation state from $\mathrm{Mn^{III}}$ to $\mathrm{Mn^{II}}$, indicated by distinct changes in the X-ray absorption at the manganese L_3 edge. A quantitative analysis of the reduction process has been performed using the manganese oxides $\mathrm{Mn_2O_3}$ ($\mathrm{Mn^{III}}$) and MnO ($\mathrm{Mn^{II}}$) as reference samples.

The rate of the reduction process strongly depends on the anion choice. The $[\mathbf{Mn_6^{III}Cr^{III}}]^{3+}$ SMM using perchlorate anions exhibits the highest stability against soft X-ray exposure: While the fraction of non-reduced $\mathrm{Mn^{III}}$ in $[\mathbf{Mn_6^{III}Cr^{III}}](\mathrm{BPh_4})_3$ and $[\mathbf{Mn_6^{III}Cr^{III}}](\mathrm{C_3H_5O_3})_3$ is reduced to 0.75 by a radiation exposure of $2.2 \cdot 10^{13}$ photons/mm^2 and $3.2 \cdot 10^{13}$ photons/mm^2, respectively, a significantly higher exposure of $1.8 \cdot 10^{14}$ photons/mm^2 leads to the same condition in the case of $[\mathbf{Mn_6^{III}Cr^{III}}](\mathrm{ClO_4})_3$. A correlation between the redox properties of the anions and the radiation stability of the SMM complex has been observed: The perchlorate anion of the more radiation-stable $[\mathbf{Mn_6^{III}Cr^{III}}](\mathrm{ClO_4})_3$ complex is a strong oxidant, while the tetraphenylborate and lactate anions of $[\mathbf{Mn_6^{III}Cr^{III}}](\mathrm{BPh_4})_3$ and $[\mathbf{Mn_6^{III}Cr^{III}}](\mathrm{C_3H_5O_3})_3$ exhibit reducing properties.

Insight into the structure of the manganese LMV and LVV Auger groups was obtained by investigating $[\mathbf{Mn_6^{III}Cr^{III}}]^{3+}$ samples using electron spectroscopy without resolving the electron spin. Changes in the PES spectra related to the radiation-induced reduction process have been observed.

Estimates for the local spin and orbital magnetic moments have been derived from spin-resolved electron spectroscopy results of $[\mathbf{Mn_6^{III}Cr^{III}}]^{3+}$ obtained for various excitation energies covering the whole Mn $L_{2,3}$ edge region. The sum rule formalism described in section 3.3.2 was used. Though this approach was originally developed for the evaluation of XMCD data measured on magnetized samples, the equivalence of the primary excitation step in both methods allows the extraction of comparable information from magnetically non-oriented samples at room temperature and without the application of external fields. A local spin magnetic moment of $\mu_{\text{spin}} = -1.8 \pm 0.4\ \mu_{\text{Bohr}}$ and an orbital contribution of $\mu_{\text{orbit}} = -0.6 \pm 0.12\ \mu_{\text{Bohr}}$ was obtained for the Mn constituents in $[\mathbf{Mn_6^{III}Cr^{III}}]^{3+}$ SMM. Mn_2O_3 and Mn^{II}acetate were investigated by electron spectroscopy with and without resolving the electron spin to obtain reference data.

XMCD measurements at a temperature of approx. 2 K and in an external magnetic field of approx. 7 T have been performed for comparison. The expected antiferromagnetic orientation of the manganese and chromium magnetic moments indicated by a different sign of the XMCD effect at the L_3 edge has been observed. The manganese local spin magnetic moment $\mu_{\text{spin}} = -1.9 \pm 0.2\ \mu_{\text{Bohr}}$ derived from XMCD is in good agreement with the value obtained from spin polarization measurements. However, significant differences are observed regarding the orbital magnetic moment: A value of $\mu_{\text{orbit}} = -0.3 \pm 0.03\ \mu_{\text{Bohr}}$ was obtained for $[\mathbf{Mn_6^{III}Cr^{III}}]^{3+}$ based on XMCD.

A comparison of Mn $L_{2,3}$ absorption spectra of $[\mathbf{Mn_6^{III}Cr^{III}}](ClO_4)_3$ obtained with and without an applied external magnetic field reveals discernible differences in the absorption at the high energy tail of the Mn L_3 edge as well as in the energetic position of the peak structure characteristic for Mn^{III}. These differences hint to a possible influence of the strong external magnetic field on the electronic state of the $[\mathbf{Mn_6^{III}Cr^{III}}]^{3+}$ SMM.

The differences found between the magnetic moments determined by AC and DC magnetometry [40] and the results obtained from SPES and XMCD are expected to arise from the notably small energetic separation between the $S_t = 21/2$ spin ground state and the first excited spin states of only 2.6 cm^{-1} [38].

Further investigations are needed to reveal the mechanism behind the observed differences: A determination of the Cr contribution to the total magnetic moment is required, as the comparative magnetization studies described in [40] probe the total sample magnetization without elemental resolution. Furthermore, the influence of the preparation-related recrystallization on the $[\mathbf{Mn_6^{III}Cr^{III}}]^{3+}$ magnetic properties needs to be investigated. Spin-resolved electron spectroscopy measurements with lower statistical error are required in the Mn L_2-L_3 inter-edge region as well as around the L_2 edge to reduce the overall statistical error of the determined magnetic moments. Besides, the correction factor applied to the sum rule formalism results should be refined and optimized for the investigated $[\mathbf{Mn_6^{III}Cr^{III}}]^{3+}$ by simulations of the obtained XMCD asymmetries via the charge transfer multiplet formalism [166].

A. Mixed $2p$ and $3d$ m_j-states

The angular parts of the mixed $2p$ ($m_j = \pm 1/2$) and $3d$ ($m_j = \pm 1/2, \pm 3/2$) m_j-states shown in figure 3.12 (thick bars) and their corresponding Clebsch-Gordan coefficients are summarized in the following table (adapted from [150]). The notation $|m_s, m_l\rangle$ was used for the contributing m_s, m_l states.

m_j	$2p_{1/2}$	$2p_{3/2}$
$-1/2$	$-\sqrt{\frac{2}{3}}\left|\frac{1}{2},-1\right\rangle + \sqrt{\frac{1}{3}}\left|-\frac{1}{2},0\right\rangle$	$\sqrt{\frac{1}{3}}\left|\frac{1}{2},-1\right\rangle + \sqrt{\frac{2}{3}}\left|-\frac{1}{2},0\right\rangle$
$+1/2$	$-\sqrt{\frac{1}{3}}\left|\frac{1}{2},0\right\rangle + \sqrt{\frac{2}{3}}\left|-\frac{1}{2},+1\right\rangle$	$\sqrt{\frac{2}{3}}\left|\frac{1}{2},0\right\rangle + \sqrt{\frac{1}{3}}\left|-\frac{1}{2},+1\right\rangle$
m_j	$3d_{3/2}$	$3d_{5/2}$
$-3/2$	$-\sqrt{\frac{4}{5}}\left|\frac{1}{2},-2\right\rangle + \sqrt{\frac{1}{5}}\left|-\frac{1}{2},-1\right\rangle$	$\sqrt{\frac{1}{5}}\left|\frac{1}{2},-2\right\rangle + \sqrt{\frac{4}{5}}\left|-\frac{1}{2},-1\right\rangle$
$-1/2$	$-\sqrt{\frac{3}{5}}\left|\frac{1}{2},-1\right\rangle + \sqrt{\frac{2}{5}}\left|-\frac{1}{2},0\right\rangle$	$\sqrt{\frac{2}{5}}\left|\frac{1}{2},-1\right\rangle + \sqrt{\frac{3}{5}}\left|-\frac{1}{2},0\right\rangle$
$+1/2$	$-\sqrt{\frac{2}{5}}\left|\frac{1}{2},0\right\rangle + \sqrt{\frac{3}{5}}\left|-\frac{1}{2},+1\right\rangle$	$\sqrt{\frac{3}{5}}\left|\frac{1}{2},0\right\rangle + \sqrt{\frac{2}{5}}\left|-\frac{1}{2},+1\right\rangle$
$+3/2$	$-\sqrt{\frac{1}{5}}\left|\frac{1}{2},+1\right\rangle + \sqrt{\frac{4}{5}}\left|-\frac{1}{2},+2\right\rangle$	$\sqrt{\frac{4}{5}}\left|\frac{1}{2},+1\right\rangle + \sqrt{\frac{1}{5}}\left|-\frac{1}{2},+2\right\rangle$

B. The UHV apparatus at BESSY II

The following images show the UHV apparatus used for the spin-resolved electron spectroscopy experiments in the fully operational state installed at the BESSY-II beamline UE52-SGM. While figure B.1 gives a side view of the setup (viewing direction perpendicular to the beam axis), figure B.2 shows the apparatus viewed in upstream direction from an elevated point of view.

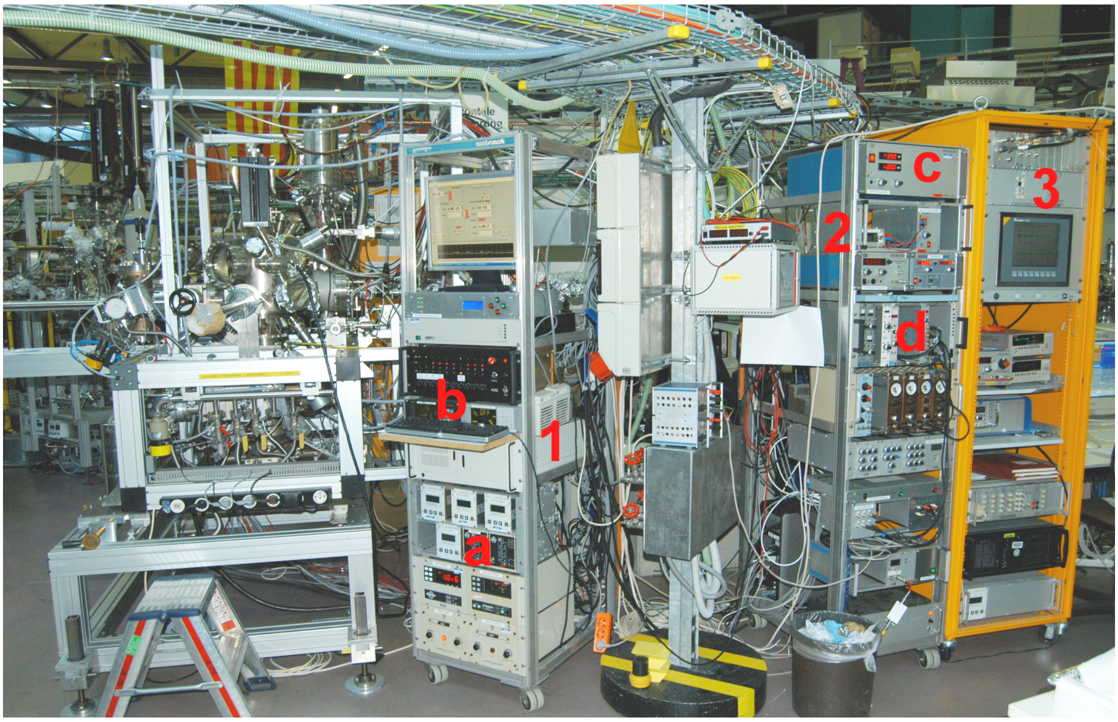

Figure B.1. Side view of the UHV apparatus (left). The machine control rack **1**, with the pump controllers **a** and the valve control panel **b** is shown. The data acquisition rack **2** with the Mott polarimeter HV supply **c** and the signal processing electronics **d** is visible next to the beamline control rack **3**.

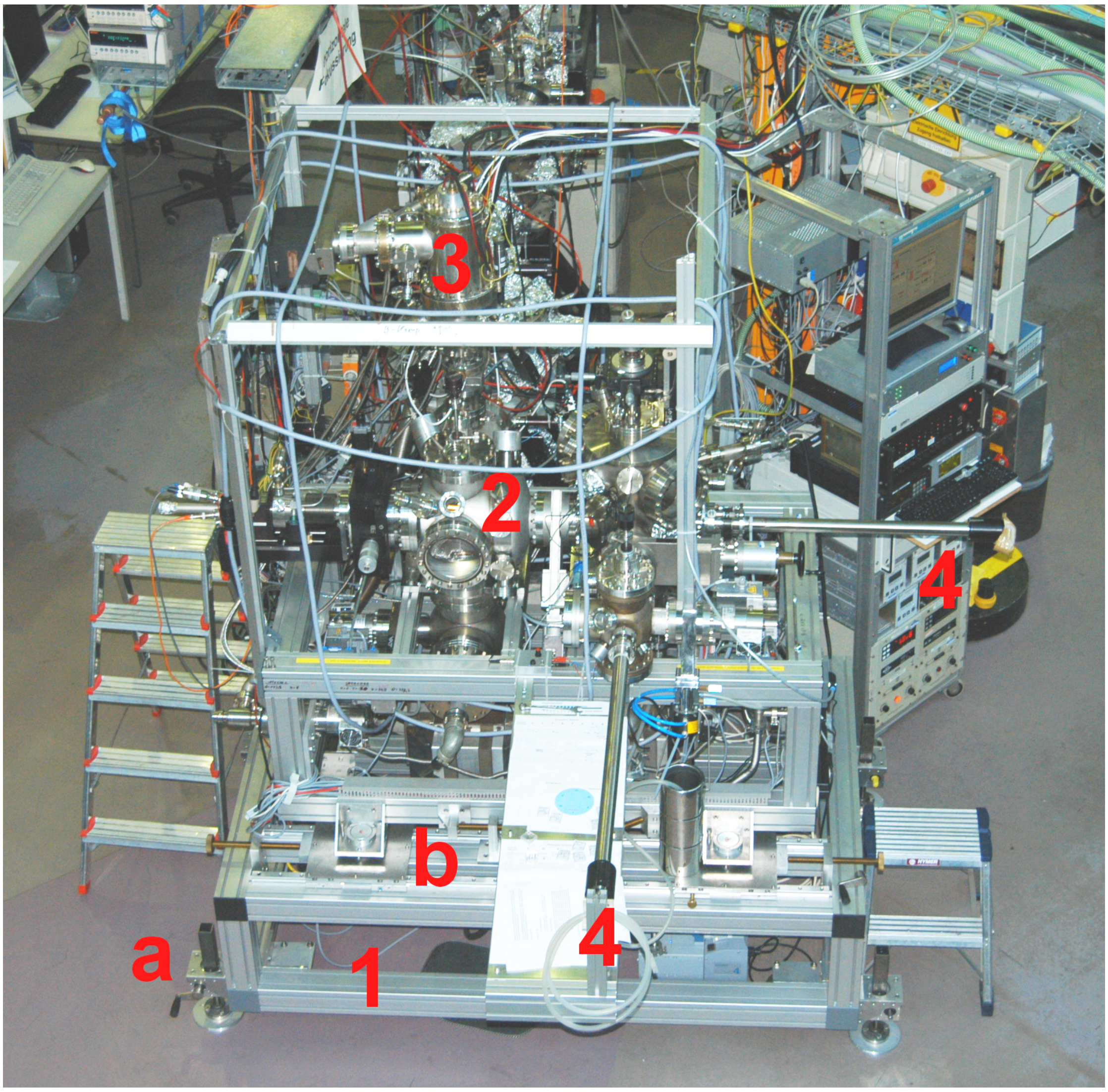

Figure B.2. Overview of the UHV apparatus with the aluminium base frame **1**, the adjustable posts **a** and the ball-casters of the upper frame adjustment mechanism **b**. The measurement chamber **2** and the Mott polarimeter **3** are visible within the cubic frame carrying the Helmholtz coils for the compensation of the terrestrial magnetic field. Also note the magnetic transfer rods **4** used for the sample transfer between vacuum chambers.

C. Error calculation algorithm for sum rule evaluation of SPES data

The following Origin Labtalk program code was used to calculate the error of the sum rule evaluation of the SPES measurements. Each spin polarization datapoint is varied within its uncertainty using normally distributed random numbers. Spin and orbital magnetic moments are then calculated for these varied spin polarisation datasets to derive the total error of the magnetic moments. The method has been described in detail on page 94.

```
// Filename:    scripts_AH.OGS
///////////////////////////////////////////////////////////////////////////////////////////

[errorcalc]
// calculate the error in sum rule result from spin polarization errors

// set parameters
r=500;              //number of runs
s=20;               //number of spin polarization datapoints

// declare range variables

    // sp=spin polarization, dp=polarization error bars, dpol=SPES dataset with errors
    range [book16]Sheet1 sp=B, dp=C, dpol=E;
    // xdata= XAS and SPES common energy range, xas=XAS data, spin=interpolated SPES data
    // with errors, spinXMCD=(XAS+XAS)*spin
    range [book10]Sheet1 xdata=G, xas=H, spin=A, spinXMCD=B, spinXMCDint=C, XASint=D;

    range [book17]Sheet1 run=A, psum=B, qsum=C, rsum=D, muspin=E, muorbit=F;


// generate as many random number vectors as spin polarization datapoints,
// vector length equals number of runs
loop(a,1,s){

    rand$(a)=normal(r);

};

// integrate XAS data
integ1 iy:=xas type:=math oy:=XASint;
```

```
// begin main loop
loop (z,1,r){

    // generate new spin polarization dataset with error
    loop(b,1,s){

        dpol[b]=sp[b]+(rand$(b)[z]*dp[b]);

    };

    // interpolate spin polarization values onto XAS energy range
    interp1 ix:=xdata iy:=dpol method:=linear ox:=spin;

    // Multiply interpolated spin polarization data and XAS data
    spinXMCD=spin*(xas+xas);

    // Integrate generated XMCD
    integ1 iy:=spinXMCD type:=math oy:=spinXMCDint;

    // Write to result sheet: number of run, p, q, r of sum rules
    run[z]=z;
    psum[z]=spinXMCDint[203];
    qsum[z]=spinXMCDint[363];
    rsum[z]=XASint[363];

    // calculate spin magnetic moment
    muspin[z]=((3*psum[z]-2*qsum[z])*6)/(rsum[z]*0.6405);

    // calculate orbital magnetic moment
    muorbit[z]=(2*qsum[z]*6)/(3*rsum[z])

// end of main loop
};

////////////////////////////////////////////////////////////////////////////////////////////
```

D. Acknowledgements

I would like to thank many people, colleagues and friends who had their share in the work behind this dissertation. Without their constant support, this would have been impossible.

First, I want to express my sincere gratitude to Prof. Ulrich Heinzmann, who gave me the opportunity to complete my dissertation in this interesting field. Fruitful discussions concerning the interpretation of the results as well as his numerous supporting visits on many beamtimes have immensely improved my understanding of the matter and resolved many difficulties. His profound knowledge and extensive experience concerning synchrotron radiation physics and spin-resolved measurement methods was one of the key contributions to the successful work of our SMM project.

All these thanks apply no less to Dr. Norbert Müller, who has been my closest advisor since the beginning of my diploma thesis. I hope that during these years I managed to adopt at least parts of his incredibly wide knowledge in the fields of UHV technology, apparatus design and spin polarization measurement. Upon completion of my diploma thesis, it was him again who introduced me to the field of spin polarization measurements. I am indebted for countless fruitful discussions, helpful remarks and amendments to beamtime proposals, publications and this thesis. During the past five years, he participated in almost every beamtime we had across Europe, always being an essential team member and fellow researcher who had a great part in the success of our measurements.

I would like to thank Dr. Armin Brechling, Aaron Gryzia, Dr. Marc Sacher, Niklas Dohmeier and Sebastian Steppeler for their support during our numerous beamtimes, although this often meant laborious preparations and long working hours at the beamline.

I am also indebted to all other colleagues and members of my workgroup that are not named explicitly here. Things would have been much more difficult without their support during beamtime preparation or their various contributions concerning the interpretation of the results.

I would like to thank Wolfgang Gronemeyer and Herbert Bergmeier as representatives for the whole staff of the mechanical and electronic workshops belonging to the Faculty of Physics of Bielefeld University. Without their constant efforts, often under the pressure of tight deadlines due to an upcoming beamtime, this work would not have been possible. Many helpful amendments to the design of intricate mechanical parts have originated from Edmund Frydrychowicz, who is still remembered and missed.

I am indebted to Prof. Thorsten Glaser and his workgroup at the Faculty of Chemistry of Bielefeld University, for providing the $[\mathbf{Mn}^{\mathbf{III}}_{\mathbf{6}}\mathbf{Cr}^{\mathbf{III}}]^{3+}$ molecules that were the main interest of my work as well as for many helpful comments, explanations and discussions concerning the complex chemistry behind these molecules.

Important findings have originated from collaborative beamtimes with the group of Prof. Ulrich Rüdiger at the University of Konstanz. I would like to thank Dr. Mikhail Fonin, Philipp Leicht and Samuel Bouvron for making some precious beamtime available for our experiments, leading to very insightful results concerning radiation effects.

A collaborative beamtime with Dr. Karsten Küpper from the Osnabrück University at the PSI in Villigen gave me the chance to perform high-quality XMCD measurements of $[\mathbf{Mn}^{\mathbf{III}}_{\mathbf{6}}\mathbf{Cr}^{\mathbf{III}}]^{3+}$ using a very sophisticated setup. Without the share of beamtime he provided, these measurements would not have been possible.

I would like to thank Thomas Tietze from the group of E. Göring at the Max-Planck-Institut für Intelligente Systeme Stuttgart for performing XMCD measurements of $\mathrm{Mn}^{\mathrm{II}}$acetate reference samples. The resulting data were very helpful with respect to the interpretation of the SPES measurements.

The continuous support of the whole BESSY-II (HZB) staff during our beamtimes was an important prerequisite for the successful completion of this work. I would like to mention Dr. Willy Mahler, Dr. Birgitt Zada and Dr. Patrick Hoffmann as representatives for the beamline scientists that supported the experiments at the BESSY-II storage ring. I am specially indebted to H. Pfau for his highly committed user support and his competent solutions to all technical and logistical problems that occurred.

I am no less indebted to the staff of the MAX-lab facility in Lund, Sweden, for their comprehensive support of our beamtimes at the MAX-II storage ring. I would like to express my gratitude to the beamline scientist of the D1011 beamline, Dr. Alexei B. Preobrajenski – his collegial support during numerous beamtimes and preparative measurements at D1011 represents an essential contribution to the work presented here. I want to mention Nikolay Vinogradov for his support at the beamline and Carolina Ingvander for commitedly solving all administrative problems during our MAX-lab beamtimes.

I would also like to thank the staff of the X11MA/SIM beamline at the Swiss Light Source (PSI), mentioning Loïc Joly as representative for the very competent user support at the beamline.

The tedious work of proofreading was done by Norbert Müller, Julia Bader and Johanna Helmstedt – I am sincerely thankful for all the comments and corrections that helped to improve my writing and to present the obtained results in an appropriate manner.

Finally, I want to express my deepest gratitude to my wife Johanna Helmstedt and my parents – without your continuous, loving support and your patience, the work of the last five years leading to the successful completion of this thesis would have been immensely more difficult, if not impossible. I am deeply indebted for all that you did for me during these years and beyond.

E. Publications

A. Helmstedt, M. D. Sacher, A. Gryzia, A. Harder, A. Brechling, N. Müller, U. Heinzmann, V. Hoeke, E. Krickemeyer, T. Glaser, S. Bouvron and M. Fonin, **Exposure of** $[\mathrm{Mn}_6^{\mathrm{III}}\mathrm{Cr}^{\mathrm{III}}]^{3+}$ **single-molecule magnets to soft X-rays: The effect of the counterions on radiation stability**, J. Electr. Spectrosc. Relat. Phenom. 184 (2012), 583-588

A. Helmstedt, N. Müller, A. Gryzia, N. Dohmeier, A. Brechling, M. D. Sacher, U. Heinzmann, V. Hoeke, E. Krickemeyer, T. Glaser, S. Bouvron, M. Fonin and M. Neumann, **Spin resolved photoelectron spectroscopy of** $[\mathrm{Mn}_6^{\mathrm{III}}\mathrm{Cr}^{\mathrm{III}}]^{3+}$ **single-molecule magnets and of manganese compounds as reference layers**, J. Phys.: Cond. Matter 23 (2011), 266001

H. Dachraoui, T. Auguste, A. Helmstedt, P. Bartz, M. Michelswirth, N. Müller, W. Pfeiffer, P. Salieres and U. Heinzmann, **Interplay between absorption, dispersion and refraction in high-order harmonic generation**, J. Phys. B: At. Mol. Opt. Phys. 42 (2009), 175402

F. Statement of Authorship

I hereby declare that this dissertation has been composed solely by me and, except where reference is made in the text, it contains no material extracted in whole or in part from any other persons work. Its contents have not been presented by me for the award of any other degree at Bielefeld University or in any tertiary institution.

Any information quoted or derived from other sources has been acknowledged by referencing to the original author and his work. Illustrations that were not composed by me have been used with the explicit permission of the publisher and the original author and are specifically acknowledged.

No third person has received any benefits with monetary value from me for any work related to this dissertation and its contents.

Ich erkläre hiermit, dass diese Dissertation ausschließlich durch mich verfasst wurde und mit Ausnahme von gekennzeichneten und mit Verweisen auf die Quelle versehenen Zitaten und Entlehnungen keine komplett oder in Teilen aus anderen Arbeiten entnommenen Informationen enthält. Der Inhalt wurde von mir nicht im Rahmen einer weiteren Prüfungsarbeit an der Universität Bielefeld oder einer anderen Institution eingereicht.

Alle aus anderen Quellen entnommenen Informationen sind mit entsprechenden Verweisen auf den Originalautor sowie dessen Arbeit gekennzeichnet. Abbildungen, die nicht durch mich erstellt wurden, sind mit ausdrücklicher Erlaubnis des Verlages sowie des Originalautors verwendet worden und entsprechend gekennzeichnet.

Keine dritten Personen haben mittelbar oder unmittelbar geldwerte Leistungen von mir erhalten, die in Zusammenhang mit der Fertigstellung dieser Dissertation oder ihrem Inhalt stehen.

Name: Andreas Helmstedt

Signature:

Date:

Bibliography

[1] R. Wood. Future hard disk drive systems. *J. Magn. Magn. Mater.*, 321:555–561, 2009.

[2] S.B. Luitjens and A.M.A. Rijckaert. The history of consumer magnetic video tape recording, from a rarity to a mass product. *J. Magn. Magn. Mater.*, 193:17–23, 1999.

[3] I.R. McFadyen, E.E. Fullerton, and M.J. Carey. State-of-the-Art Magnetic Hard Disk Drives. *MRS Bull.*, 31:379, 2006.

[4] R. Wood. The feasibility of Magnetic Recording at 1 Terabit per Square Inch. *IEEE Trans. Magn.*, 36:36, 2000.

[5] H.J. Richter. Density limits imposed by the microstructure of magnetic recording media. *J. Magn. Magn. Mater.*, 321:467–476, 2009.

[6] J.C. Mallinson. Scaling in Magnetic Recording. *IEEE Trans. Magn.*, 32:599, 1996.

[7] D.L.A. Tjaden and J. Leyten. A 5000:1 Scale Model of the Magnetic Recording Process. *Philips Tech. Rev.*, 25:319–329, 1964.

[8] G.W. Qin, Y.P. Ren, N. Xiao, B. Yang, L. Zuo, and K. Oikawa. Development of high density magnetic recording media for hard disk drives: materials science issues and challenges. *Intern. Materials Review*, 54:157, 2009.

[9] P.A. Grünberg. From Spinwaves to Giant Magnetoresistance (GMR) and Beyond. In K. Grandin, editor, *Les Prix Nobel. The Nobel Prizes 2007*, page 92. Nobel Foundation Stockholm, 2008.

[10] S. Iwasaki. Perpendicular Magnetic Recording. *IEEE Transactions on Magnetics*, MAG-16: 71, 1980.

[11] A.S. Hoagland. History of Magnetic Disc Storage Based on Perpendicular Magnetic Recording. *IEEE Transactions on Magnetics*, 39:1871, 2003.

[12] Y. Shiroishi, K. Fukuda, I. Tagawa, H. Iwasaki, S. Takenoiri, H. Tanaka, H. Mutoh, and N. Yoshikawa. Future Options for HDD Storage. *IEEE Transactions on Magnetics*, 45: 3816, 2009.

[13] X. Wang, J. Fernandez de Castro, K. Gao, and Z. Jin. Thermal Reversal of Magnetic Grains Under Time Varying Pulse Field. *IEEE Transactions on Magnetics*, 42:2294, 2006.

[14] C.-G. Stefanita. *From Bulk to Nano. The Many Sides of Magnetism*, page 131. Springer Series in Materials Science. Springer Verlag Berlin Heidelberg, 2008.

[15] S.H. Charap, P.-L. Lu, and Y. He. Thermal Stability of Recorded Information at High Densities. *IEEE Transactions on Magnetics*, 33:978, 1997.

[16] C.P. Bean and J.D. Livingston. Superparamagnetism. *J. Appl. Phys.*, 30:S120, 1959.

[17] C.A. Ross. Patterned Magnetic Recording Media. *Annu. Rev. Mater. Res.*, 31:203–235, 2001.

[18] A. Moser, K. Takano, D.T. Margulies, M. Albrecht, Y. Sonobe, Y. Ikeda, S. Sun, and E.E. Fullerton. Magnetic recording: advancing into the future. *J. Phys. D: Appl. Phys.*, 35: R157, 2002.

[19] J. Nickel and G. Gibson. Beyond Magnetic Storage: Atoms and Molecules. In G.C. Hadjipanayis, editor, *Magnetic Storage Systems Beyond 2000*, NATO Science Series, page 599. Kluwer Academic Publishers Dordrecht, 2001.

[20] N.S. Hush. An Overview of the First Half-Century of Molecular Electronics. *Ann. N.Y. Acad. Sci.*, 1006:1–20, 2003.

[21] M. Tsutsui and M. Taniguchi. Single-Molecule Electronics and Devices. *Sensors*, 12: 7259–7298, 2012.

[22] N. Renaud, M. Hliwa, and C. Joachim. Single Molecule Logical Devices. In R.M. Metzger, editor, *Unimolecular and Supramolecular Electronics II - Chemistry and Physics Meet at Metal-Molecule Interfaces*, Topics in Current Chemistry, page 217. Springer Verlag Berlin Heidelberg, 2012.

[23] S.M.J. Aubin, M.W. Wemple, D.M. Adams, H.-L. Tsai, G. Christou, and D.N. Hendrickson. Distorted $\mathrm{Mn}^{IV}\mathrm{Mn}_3^{III}$ Cubane Complexes as Single-Molecule Magnets. *J. Am. Chem. Soc.*, 118:7746–7754, 1996.

[24] D. Gatteschi and R. Sessoli. Quantum Tunneling of Magnetization and Related Phenomena in Molecular Materials. *Angew. Chem. Int. Ed.*, 42:268, 2003.

[25] G. Christou, D. Gatteschi, D.N. Hendrickson, and R. Sessoli. Single-Molecule Magnets. *MRS Bull.*, 25:66–71, 2000.

[26] J. Tejada, E.M. Chudnovsky, E. del Barco, J.M. Hernandez, and T.P. Spiller. Magnetic qubits as hardware for quantum computers. *Nanotechnology*, 12:181–186, 2001.

[27] D.D. Awschalom, D.P. DiVincenzo, and J.F. Smyth. Macroscopic Quantum Effects in Nanometer-Scale Magnets. *Science*, 258:414, 1992.

[28] M.N. Leuenberger and D. Loss. Quantum computing in molecular magnets. *Nature*, 410:789, 2001.

[29] L. Bogani and W. Wernsdorfer. Molecular spintronics using single-molecule magnets. *Nature Materials*, 7:179, 2008.

[30] N. Goldman, P. Bertone, S. Chen, C. Dessimoz, E.M. LeProust, B. Sipos, and E. Birney. Towards practical, high-capacity, low-maintenance information storage in synthesized DNA. *Nature*, 494:77, 2012.

[31] M. Mannini, F. Pineider, P. Sainctavit, L. Joly, A. Fraile-Rodríguez, M.-A. Arrio, C. Cartier dit Moulin, W. Wernsdorfer, A. Cornia, D. Gatteschi, and R. Sessoli. X-Ray Magnetic Circular Dichroism Picks out Single-Molecule Magnets Suitable for Nanodevices. *Adv. Mater.*, 21:167–171, 2009.

[32] M. Mannini, F. Pineider, C. Danieli, F. Totti, L. Sorace, Ph. Sainctavit, M.-A. Arrio, E. Otero, L. Joly, J.C. Cezar, A. Cornia, and R. Sessoli. Quantum tunnelling of the magnetization in a monolayer of oriented single-molecule magnets. *Nature*, 468:417, 2010.

[33] G. Rogez, B. Donnio, E. Terazzi, J.-L. Gallani, J.-P. Kappler, J.-P. Bucher, and M. Drillon. The Quest for Nanoscale Magnets: The example of [Mn12] Single Molecule Magnets. *Adv. Mater.*, 21:4323–4333, 2009.

[34] R.E.P. Winpenny. Serendipitous assembly of polynuclear cage compounds. *Dalton Trans.*, 2002:1–10, 2002.

[35] T. Lis. Preparation, Structure, and Magnetic Properties of a Dodecanuclear Mixed-Valence Manganese Carboxylate. *Acta Cryst. B*, 36:2042–2046, 1981.

[36] R. Sessoli, H. L. Tsai, A. R. Schake, S. Wang, J. B. Vincent, K. Folting, D. Gatteschi, G. Christou, and D. N. Hendrickson. High-spin molecules: $[Mn_{12}O_{12}(O_2CR)_{16}(H_2O)_4]$. *J. Am. Chem. Soc.*, 115:1804–1816, 1993.

[37] R. Bagai and G. Christou. The Drosophila of single-molecule magnetism: $[Mn_{12}O_{12}(O_2CR)_{16}(H_2O)_4]$. *Chem. Soc. Rev.*, 38:1011–1026, 2009.

[38] T. Glaser, M. Heidemeier, T. Weyhermüller, R.-D. Hoffmann, H. Rupp, and P. Müller. Property-Oriented Rational Design of Single-Molecule Magnets: A C_3-Symmetric Mn_6Cr Complex based on Three Molecular Building Blocks with a Spin Ground State of S_t=21/2. *Angew. Chem. Int. Ed.*, 45:6033–6037, 2006.

[39] T. Glaser. Rational design of single-molecule magnets: a supramolecular approach. *Chem. Commun.*, 47:116–130, 2011.

[40] V. Hoeke, M. Heidemeier, E. Krickemeyer, A. Stammler, H. Bögge, J. Schnack, A. Postnikov, and T. Glaser. Environmental Influence on the Single-Molecule Magnet Behavior of $[\mathbf{Mn_6^{III}Cr^{III}}]^{3+}$: Molecular Symmetry versus Solid-State Effects. *Inorg. Chem.*, 51:10929–10954, 2012.

[41] H. Wende and C. Antoniak. X-Ray Magnetic Dichroism. In E. Beaurepaire, H. Bulou, F. Scheurer, and J.-P. Kappler, editors, *Magnetism and Synchrotron Radiation*, Springer Proceedings in Physics, page 145. Springer Verlag Berlin Heidelberg, 2010.

[42] R. Sessoli, M. Mannini, F. Pineider, A. Cornia, and Ph. Sainctavit. XAS and XMCD of Single Molecule Magnets. In E. Beaurepaire, H. Bulou, F. Scheurer, and J.-P. Kappler, editors, *Magnetism and Synchrotron Radiation*, Springer Proceedings in Physics, page 279. Springer Verlag Berlin Heidelberg, 2010.

[43] T. Nakamura and M. Suzuki. Recent Progress of the X-ray Magnetic Circular Dichroism Technique for Element-Specific Magnetic Analysis. *J. Phys. Soc. Jpn.*, 82:021006, 2013.

[44] N. Müller, T. Lischke, M.R. Weiss, and U. Heinzmann. Spin resolved photoelectron spectroscopy from paramagnetic Gd at the 4d→4f resonance using circularly polarized radiation, a cross comparison with MCD. *J. Electron Spectrosc. Relat. Phenom.*, 114-116: 777–782, 2001.

[45] U. Fano. Spin Orientation of Photoelectrons Ejected by Circularly Polarized Light. *Physical Review*, 178:131–136, 1969.

[46] G. van der Laan and B.T. Thole. Spin polarization and magnetic dichroism in photoemission from core and valence states in localized magnetic systems. IV. Core-hole polarization in resonant photoemission. *Phys. Rev. B*, 52:15355, 1995.

[47] U. Heinzmann and J.H. Dil. Spin-orbit-induced photoelectron spin polarization in angle-resolved photoemission from both atomic and condensed matter targets. *J. Phys.: Condens. Matter*, 24:173001, 2012.

[48] D. Gatteschi, R. Sessoli, and J. Villain. *Molecular Nanomagnets*, pages 6,11,17,138,145. Oxford University Press, 2006.

[49] R. Sessoli, D. Gatteschi, A. Caneschi, and M.A. Novak. Magnetic bistability in a metal-ion cluster. *Nature*, 365:141, 1993.

[50] A. Caneschi, D. Gatteschi, and R. Sessoli. Alternating Current Susceptibility, High Field Magnetization, and Millimeter Band EPR Evidence for a Ground S=10 State in $[Mn_{12}O_{12}(CH_3COO)_{16}(H_2O)_4] \cdot 2CH_3COOH \cdot 4H_2O$. *J. Am. Chem. Soc.*, 113:5873–5874, 1991.

[51] T. Glaser. Rational Design of Single-Molecule Magnets. In C. Hill and D.G. Musaev, editors, *Complexity in Chemistry and Beyond: Interplay Theory and Experiment*, NATO Science for Peace and Security Series, page 73. Springer Science+Business Media Dordrecht, 2012.

[52] R.A. Robinson, P.J. Brown, D.N. Argyriou, D.N. Hendrickson, and S.M.J. Aubin. Internal magnetic structure of Mn_{12} acetate by polarized neutron diffraction. *J. Phys.: Condens. Matter*, 12:2805–2810, 2000.

[53] M. Heidemeier. *Koordinationschemie M-phenylenverbrückter Übergangsmetallkomplexe und deren Verwendung in der gezielten Synthese von Einzelmolekülmagneten.* dissertation, Mathematisch-Naturwissenschaftliche Fakultät der Westfälischen Wilhelms-Universität Münster, 2006.

[54] W. Wernsdorfer. Classical and Quantum Magnetization Reversal Studied in Nanometer-Sized Particles and Clusters. In I. Prigogine and S.A. Rice, editors, *Complexity in Chemistry and Beyond: Interplay Theory and Experiment*, volume 118 of *Advances in Chemical Physics*, page 99. John Wiley & Sons, Inc. New York, 2001.

[55] T. Glaser, M. Heidemeier, E. Krickemeyer, H. Bögge, A. Stammler, R. Fröhlich, E. Bill, and J. Schnack. Exchange Interactions and Zero-Field Splittings in C_3-Symmetric $\mathrm{Mn}_6^{\mathrm{III}}\mathrm{Fe}^{\mathrm{III}}$: Using Molecular Recognition for the Construction of a Series of High Spin Complexes Based on the Triplesalen Ligand. *Inorg. Chem.*, 48:607–620, 2009.

[56] C.-G. von Richthofen, A. Stammler, H. Bögge, M.W. DeGroot, J.R. Long, and T. Glaser. Synthesis, Structure, and Magnetic Characterization of a C_3-Symmetric $\mathrm{Mn}_3^{\mathrm{III}}\mathrm{Cr}^{\mathrm{III}}$ Assembly: Molecular Recognition Between a Trinuclear $\mathrm{Mn}^{\mathrm{III}}$ Triplesalen Complex and a *fac*-Triscyano $\mathrm{Cr}^{\mathrm{III}}$ Complex. *Inorg. Chem.*, 48:10165–10176, 2009.

[57] E. Krickemeyer, V. Hoeke, A. Stammler, H. Bögge, J. Schnack, and T. Glaser. Synthesis and Characterization of the Heptanuclear $[\mathbf{Mn}_6^{\mathrm{III}}\mathbf{Co}^{\mathrm{III}}]^{3+}$ Triplesalen Complex: Evidence for Exchange Pathways Involving Low-spin $\mathrm{Co}^{\mathrm{III}}$. *Z. Naturforsch.*, 65b:295–303, 2010.

[58] V. Hoeke, K. Gieb, P. Müller, L. Ungur, L.F. Chibotaru, M. Heidemeier, E. Krickemeyer, A. Stammler, H. Bögge, C. Schröder, J. Schnack, and T. Glaser. Hysteresis in the ground and excited spin state up to 10 T of a $[\mathbf{Mn}_6^{\mathrm{III}}\mathbf{Mn}^{\mathrm{III}}]^{3+}$ triplesalen single-molecule magnet. *Chem. Sci.*, 3:2868–2882, 2012.

[59] V. Hoeke, M. Heidemeier, E. Krickemeyer, A. Stammler, H. Bögge, J. Schnack, and T. Glaser. Structural influences on the exchange coupling and zero-field splitting in the single-molecule magnet $[\mathbf{Mn}_6^{\mathrm{III}}\mathbf{Mn}^{\mathrm{III}}]^{3+}$. *Dalton Trans.*, 2012:12942, 2012.

[60] T. Glaser, M. Heidemeier, R. Fröhlich, P. Hildebrandt, E. Bothe, and E. Bill. Trinuclear Nickel Complexes with Triplesalen Ligands: Simultaneous Occurence of Mixed Valence and Valence Tautomerism in the Oxidized Species. *Inorg. Chem.*, 44:5467–5482, 2005.

[61] A. Helmstedt, M. D. Sacher, A. Gryzia, A. Harder, A. Brechling, N. Müller, U. Heinzmann, V. Hoeke, E. Krickemeyer, T. Glaser, S. Bouvron, and M. Fonin. Exposure of $[\mathrm{Mn}_6^{\mathrm{III}}\mathrm{Cr}^{\mathrm{III}}]^{3+}$ single-molecule magnets to soft X-rays: The effect of the counterions on radiation stability. *J. Electron Spectrosc. Relat. Phenom.*, 184:583–588, 2012.

[62] Xi. Shen, B. Li, J. Zou, Z. Xu, Y. Yu, and S. Liu. Crystal structure of a cyanide-bridged heptanuclear manganese(III)–chromium(III) complex with a ground state S = 21/2. *Trans. Metal Chem.*, 27:372–376, 2002.

[63] T. Glaser, M. Gerenkamp, and R. Fröhlich. Targeted Synthesis of Ferromagnetically Coupled Complexes with Modified 1,3,5-Trihydroxybenzene Ligands. *Angew. Chem. Int. Ed.*, 41:3823, 2002.

[64] T. Glaser, M. Heidemeier, S. Grimme, and E. Bill. Targeted Ferromagnetic Coupling in a Trinuclear Copper(II) Complex: Analysis of the S_t=3/2 Spin Ground State. *Inorg. Chem.*, 43:5192–5194, 2004.

[65] V.Â. Ung, A.M.W. Cargill Thompson, D.A. Bardwell, D. Gatteschi, J.C. Jeffery, J.A. McCleverty, F. Totti, and M.D. Ward. Roles of Bridging Ligand Topology and Conformation in Controlling Exchange Interactions between Paramagnetic Molybdenum Fragments in Dinuclear and Trinuclear Complexes. *Inorg. Chem.*, 36:3447–3454, 1997.

[66] A. Bencini, I. Ciofini, and M.G. Uytterhoeven. Angular overlap calculations of the spin Hamiltonian parameters of transition metal ions in low symmetry environments. High spin iron(II), iron(III) and manganese(III). *Inorg. Chim. Acta*, 274:90–101, 1998.

[67] B.J. Kennedy and K.S. Murray. Magnetic Properties and Zero-Field Splitting in High-Spin Manganese(III) Complexes. 1. Mononuclear and Polynuclear Schiff-Base Chelates. *Inorg. Chem.*, 24:1552, 1985.

[68] W. Gerlach and O. Stern. Der experimentelle Nachweis der Richtungsquantelung im Magnetfeld. *Zeitschrift für Physik A*, 9:349, 1922.

[69] W. Gerlach and O. Stern. Das magnetische Moment des Silberatoms. *Zeitschrift für Physik A*, 9:353, 1922.

[70] J. Mehra and H. Rechenberg. *The Quantum Theory of Planck, Einstein, Bohr and Sommerfeld: Its foundation and the Rise of Its Difficulties 1900-1925*, volume 1 of *The Historical Development of Quantum Theory*, pages 375,629,684. Springer Verlag New York Heidelberg Berlin, 1982.

[71] D.I. Blokhintsev. *Quantum Mechanics*, page 193. D. Reidel Publishing Company Dordrecht Holland, 1964.

[72] G.E. Uhlenbeck and S. Goudsmit. Ersetzung der Hypothese vom unmechanischen Zwang durch eine Forderung bezüglich des inneren Verhaltens jedes einzelnen Elektrons. *Naturwissenschaften*, 13:953, 1925.

[73] S. Goudsmit and G.E. Uhlenbeck. Die Kopplungsmöglichkeiten der Quantenvektoren im Atom. *Zeitschrift für Physik A*, 35:618, 1925.

[74] W. Pauli. Über den Zusammenhang des Abschlusses der Elektronengruppen im Atom mit der Komplexstruktur der Spektren. *Zeitschrift für Physik A*, 31:765–783, 1925.

[75] G.E. Uhlenbeck and S. Goudsmit. Spinning electrons and the Structure of Spectra. *Nature*, 117:264, 1926.

[76] D.J. Griffiths. *Introduction to Quantum Mechanics*, pages 171,174,175. Pearson Education International, 2005.

[77] B.H. Bransden and C.J. Joachain. *Quantum Mechanics*, pages 293,299,308,311,684,714. Pearson Education International, 2000.

[78] R.H. Dicke and J.P. Wittke. *Introduction to Quantum Mechanics*, page 194. Addison-Wesley Publishing Company Inc., 1960.

[79] J. Kessler. *Polarized Electrons*, pages 1,9–12,20–35,40–43,60. Springer Series on Atoms+Plasmas. Springer Verlag Berlin Heidelberg New York, 1976.

[80] N. Sherman and D.F. Nelson. Determination of Electron Polarization by Means of Mott Scattering. *Phys. Rev.*, 114:1541, 1959.

[81] N. Sherman. Coulomb Scattering of Relativistic Electrons by Point Nuclei. *Phys. Rev.*, 103:1601, 1956.

[82] M. Getzlaff, B. Heidemann, J. Bansmann, C. Westphal, and G. Schönhense. A variable-angle electron spin polarization detection system. *Rev. Sci. Instrum.*, 69:3913, 1998.

[83] F.R. Elder, A.M. Gurewitsch, R.V. Langmuir, and H.C. Pollock. Radiation from Electrons in a Synchrotron. *Phys. Rev.*, 71:829–830, 1947.

[84] H. Wiedemann. *Synchrotron radiation*, pages 31,35,59,65. Advanced Texts in Physics. Springer-Verlag, 2003.

[85] J.P. Blewett. Radiation Losses in the Induction Electron Accelerator. *Phys. Rev.*, 69:87–95, 1946.

[86] D. Iwanenko and I. Pomeranchuk. On the Maximal Energy Attainable in a Betatron. *Phys. Rev.*, 65:343, 1944.

[87] A. Liènard. Champ électrique et Magnétique. *L'éclairage électrique*, 16:5–14, 53–59, 106–112, 1898.

[88] E. Wiechert. Elektrodynamische Elementargesetze. *Ann. Phys.*, 309:667–689, 1901. Republished online: 2006.

[89] G.A. Schott. Über die Strahlung von Elektronengruppen. *Ann. Phys. (Leipzig)*, 24: 635–660, 1907.

[90] D. Cocco and M. Zangrando. Synchrotron Radiation Sources and Optical Devices. In E. Beaurepaire, H. Bulou, F. Scheurer, and J.-P. Kappler, editors, *Magnetism and Synchrotron Radiation*, Springer Proceedings in Physics, page 127. Springer Verlag Berlin Heidelberg, 2010.

[91] K. Codling. Atomic and Molecular Physics Using Synchrotron Radiation - the Early Years. *J. Synchrotron Rad.*, 4:316–333, 1997.

[92] D.W. Lynch. Tantalus, a 240 MeV Dedicated Source of Synchrotron Radiation, 1968-1986. *J. Synchrotron Rad.*, 4:334–343, 1997.

[93] G.N. Kulipanov. Ginzburg's invention of undulators and their role in modern synchrotron radiation sources and free electron lasers. *Physics-Uspekhi*, 50:368–376, 2007.

[94] S. Sasaki. Analyses for a planar variably-polarizing undulator. *Nucl. Instrum. Meth. A*, 347:83–86, 1994.

[95] H. Winick. Properties of Synchrotron Radiation. In H. Winick and S. Doniach, editors, *Synchrotron Radiation Research*, page 11. Plenum Press New York London, 1980.

[96] C. Kunz. Introduction - Properties of Synchrotron Radiation. In C. Kunz, editor, *Synchrotron Radiation. Techniques and Applications*, page 11. Springer Verlag Berlin Heidelberg New York, 1979.

[97] K. Godehusen (BESSY-II, Helmholtz-Zentrum Berlin). UE52-SGM beamline technical documentation, 2009. personal communication.

[98] W. Mahler (FHI der MPG, BESSY-II, Helmholtz-Zentrum Berlin). UE56/2-PGM-2 beamline technical documentation, 2013. personal communication.

[99] Alexei B. Preobrajenski (MAX-II, MAX lab Lund). D1011 beamline technical documentation, 2009. personal communication.

[100] Loïc Joly (SLS, Paul-Scherrer-Institut Villigen). X11MA/SIM beamline technical documentation, 2011. personal communication.

[101] J. Bahrdt, W. Frentrup, A. Gaupp, M. Scheer, W. Gudat, G. Ingold, and S. Sasaki. Elliptically polarizing insertion devices at BESSY II. *Nucl. Instrum. Meth. A*, 467-468:21–29, 2001.

[102] A.T. Young, E. Arenholz, J. Feng, H. Padmore, S. Marks, R. Schlueter, E. Hoyer, N. Kelez, and C. Steier. A Soft X-Ray Undulator Beamline at the Advanced Light Source With Circular and Variable Linear Polarization for the Spectroscopy and Microscopy of Magnetic Materials. *Surf. Rev. Lett.*, 9:549–554, 2002.

[103] K. Godehusen, H.-C. Mertins, T. Richter, P. Zimmermann, and M. Martins. Electron-correlation effects in the angular distribution of photoelectrons from Kr investigated by rotating the polarization axis of undulator radiation. *Phys. Rev. A*, 68:012711, 2003.

[104] F. Senf (BESSY-II, Helmholtz-Zentrum Berlin). UE52-SGM flux data, 2009. personal communication.

[105] K.J.S. Sawhney, F . Senf, M. Scheer, F. Schäfers, J. Bahrdt, A. Gaupp, and W. Gudat. A novel undulator-based PGM beamline for circularly polarised synchrotron radiation at BESSY II. *Nucl. Instrum. Meth. A*, 390:395–402, 1997.

[106] H. Petersen. The Plane Grating and Elliptical Mirror: A New Optical Configuration For Monochromators. *Optics Commun.*, 40:402, 1982.

[107] H. Petersen, C. Jung, C. Hellwig, W.B. Peatman, and W. Gudat. Review of plane grating focusing for soft x-ray monochromators. *Rev. Sci. Instrum.*, 66:1–14, 1995.

[108] R. Nyholm, S. Svensson, J. Nordgren, and A. Flodström. A Soft X-Ray Monochromator for the MAX Synchrotron Radiation Facility. *Nucl. Instrum. Meth. A*, 246:267–271, 1986.

[109] Highly Oriented Pyrolytic Graphite, type ZYB, manufacturer: Anfatec Instruments AG, Melanchthonstr. 28, D-08606 Oelsnitz.

[110] brand name: Arrandee, manufacturer: Dr. Dirk Schröer, Schlossstrasse 94, D-33824 Werther, Germany.

[111] manufacturer: MaTeck GmbH, Im Langenbroich 20, D-52428 Juelich.

[112] M. Meinert. personal communication, November 2010.

[113] Plano G2730A (400 mesh, thin bar, Au coated copper), manufacturer: Plano GmbH, Ernst-Befort-Strasse 12, D-35578 Wetzlar.

[114] model: Grafo T1, manufacturer: Harder & Steenbeck GmbH & Co. KG, Hans-Böckler-Ring 37, D-22851 Norderstedt.

[115] D. Attwood. *Soft X-Rays and Extreme Ultraviolet Radiation*, page 2. Cambridge University Press, 1999.

[116] J.A. Bearden and A.F. Burr. Reevaluation of X-Ray Atomic Energy Levels. *Rev. Mod. Phys.*, 39:125, 1967.

[117] M. Cardona and L. Ley, editors. *Photoemission in Solids I: General Principles*, pages 84,85. Springer Verlag Berlin, 1978.

[118] J.C. Fuggle and N. Mårtensson. Core-Level Binding Energies in Metals. *J. Electron Spectrosc. Relat. Phenom.*, 21:275–281, 1980.

[119] A.C. Thompson, editor. *X-RAY DATA BOOKLET*, pages 1–1. Lawrence Berkeley National Laboratory, 2009.

[120] S. P. Cramer, F.M.F. de Groot, Y. Ma, C. T. Chen, F. Sette, C. A. Kipke, D. M. Eichhorn, M. K. Chan, W. H. Armstrong, E. Libby, G. Christou, S. Brooker, V. McKee, O. C. Mullins, and J. C. Fuggle. Ligand Field Strengths and Oxidation States from Manganese L-Edge Spectroscopy. *J. Am. Chem. Soc.*, 113:7937–7940, 1991.

[121] M. M. Grush, Y. Muramatsu, J. H. Underwood, E. M. Gullikson, D. L. Ederer, R. C. C. Perera, and T. A. Callcott. Soft X-ray emission and absorption – a comparative study on the sensitivity to oxidation state and ligand environment of transition metal complexes. *J. Electron Spectrosc. Relat. Phenom.*, 92:225–229, 1998.

[122] K.J. Tiemann, J.L. Gardea-Torresdey, G. Gamez, K. Dokken, I. Cano-Aguilera, M.W. Renner, and L.R. Furenlid. Effects of Oxidation State on Metal Ion Binding by *Medicago sativa* (Alfalfa): Atomic and X-Ray Absorption Spectroscopic Studies with Fe(II) and Fe(III). *Environ. Sci. Technol.*, 34:693–698, 2000.

[123] A.N. Mansour, P.H. Smith, W.M. Baker, M. Balasubramanian, and J. McBreen. In situ XAS investigation of the oxidation state and local structure of vanadium in discharged and charged V_2O_5 aerogel structures. *Electrochim. Acta*, 47:3151–3161, 2002.

[124] M. Haumann, C. Müller, P. Liebisch, L. Iuzzolino, J. Dittmer, M. Grabolle, T. Neisius, W. Meyer-Klaucke, and H. Dau. Structural and Oxidation State Changes of the Photosystem II Manganese Complex in Four Transitions of the Water Oxidation Cycle ($S_0 \rightarrow S_1$, $S_1 \rightarrow S_2$, $S_2 \rightarrow S_3$, and $S_{3,4} \rightarrow S_0$) Characterized by X-ray Absorption Spectroscopy at 20 K and Room Temperature. *Biochemistry*, 44:1894–1908, 2005.

[125] S. Voss, M. Fonin, L. Burova, M. Burgert, Y.S. Dedkov, A.B. Preobrajenski, E. Goering, U. Groth, A. R. Kaul, and U. Ruediger. Investigation of the stability of Mn_{12} single molecule magnets. *Appl. Phys A*, 94:491–495, 2009.

[126] R.C. Nelson and J.T. Miller. An introduction to X-ray absorption spectroscopy and its *in situ* application to organometallic compounds and homogeneous catalysts. *Catal. Sci. Technol.*, 2:461–470, 2012.

[127] A. Bianconi. XANES Spectroscopy. In D.C. Koningsberger and R. Prins, editors, *X-Ray Absorption. Principles, Applications, Techniques of EXAFS, SEXAFS and XANES*, page 573. John Wiley & Sons, 1988.

[128] F.C. Brown. Inner-Shell Threshold Spectra. In H. Winick and S. Doniach, editors, *Synchrotron Radiation Research*, page 61. Plenum Press New York London, 1980.

[129] W. Demtröder. *Experimentalphysik 3: Atome, Moleküle und Festkörper*, page 170. Springer Verlag Heidelberg Berlin, 2005.

[130] F. de Groot and J. Vogel. Fundamentals of X-Ray Absorption and Dichroism: The Multiplet Approach. In F. Hippert, E. Geissler, J.L. Hodeau, E. Lelièvre-Berna, and J.-R. Regnard, editors, *Neutron and X-ray Spectroscopy*, Grenoble Sciences, page 3. Springer, 2006.

[131] S.M. Heald. Design of an EXAFS Experiment. In D.C. Koningsberger and R. Prins, editors, *X-Ray Absorption. Principles, Applications, Techniques of EXAFS, SEXAFS and XANES*, page 87. John Wiley & Sons, 1988.

[132] J. Jaclevic, J.A. Kirby, M.P. Klein, and A.S. Robertson. Fluorescence Detection of EXAFS: Sensitivity Enhancement for Dilute Species and Thin Films. *Solid State Commun.*, 23: 679–682, 1977.

[133] S.P. Cramer, O. Tench, M. Yocum, and G.N. George. A 13-Element Ge Detector for Fluorescence EXAFS. *Nucl. Instrum. Meth. A*, 266:586–591, 1988.

[134] J. Vogel and M. Sacchi. Experimental estimate of absorption length and total electron yield (TEY) probing depth in dysprosium. *J. Elec. Spectrosc. Relat. Phenom.*, 67:181–188, 1994.

[135] M. Abbate, J.B. Goedkoop, F.M.F. de Groot, M. Grioni, J.C. Fuggle, S. Hofmann, H. Petersen, and M. Sacchi. Probing Depth of Soft X-ray Absorption Spectroscopy Measured in Total-electron-yield Mode. *Surf. Int. Anal.*, 18:65–69, 1992.

[136] W. Gudat and C. Kunz. Close Similarity between Photoelectric Yield and Photoabsorption Spectra in the Soft-X-Ray Range. *Phys. Rev. Lett.*, 29:169, 1972.

[137] J. Somers. X-Ray Absorption Spectroscopy of Small Molecules, Free and Adsorbed on Surfaces. In J.C. Fuggle and J.E. Inglesfield, editors, *Unoccupied Electronic States. Fundamentals for XANES, EELS, IPS and BIS*, volume 69 of *Topics in Applied Physics*, page 177. Springer Verlag Berlin Heidelberg, 1992.

[138] M. Pedio, J.C. Fuggle, J. Somers, E. Umbach, J. Haase, T. Lindner, U. Höfer, M. Grioni, F.M.F. de Groot, B. Hillert, L. Becker, and A. Robinson. Covalency in oxygen chemisorption as probed by x-ray absorption. *Phys. Rev. B*, 40:7924, 1989.

[139] B.T. Thole, G. van der Laan, J.C. Fuggle, G.A. Sawatzky, R.C. Karnatak, and J.-M. Esteva. $3d$ x-ray-absorption lines and the $3d^9 4f^{n+1}$ multiplets of the lanthanides. *Phys. Rev. B*, 32:5107, 1985.

[140] M. Grioni. Photoelectron Spectroscopy. In F. Hippert, E. Geissler, J.L. Hodeau, E. Lelièvre-Berna, and J.-R. Regnard, editors, *Neutron and X-ray Spectroscopy*, Grenoble Sciences, page 189. Springer, 2006.

[141] J.L. Erskine and E.A. Stern. Calculation of the $M_{2,3}$ magneto-optical absorption spectrum of ferromagnetic nickel. *Phys. Rev. B*, 12:5016, 1975.

[142] G. Schütz, W. Wagner, W. Wilhelm, P. Kienle, R. Zeller, R. Frahm, and G. Materlik. Absorption of Circularly Polarized X-Rays in Iron. *Phys. Rev. Lett.*, 58:737, 1987.

[143] C.T. Chen, F. Sette, Y. Ma, and S. Modesti. Soft-x-ray magnetic circular dichroism at the $L_{2,3}$ edges of nickel. *Phys. Rev. B*, 42:7262, 1990.

[144] F. Meier and D. Pescia. Spin-polarized photoemission by optical orientation. In F. Meier and B. Zakharchenya, editors, *Optical Orientation*, Modern Problems in Condensed Matter Sciences, page 295. North-Holland Physics Publishing, 1984.

[145] J. Stöhr. X-ray magnetic circular dichroism spectroscopy of transition metal thin films. *J. Electron Spectrosc. Relat. Phenom.*, 75:253–272, 1995.

[146] A. Scherz. *Spin-dependent X-ray Absorption Spectroscopy of* $3d$ *Transition Metals: Systematics and Applications.* dissertation, Fachbereich Physik der Freien Universität Berlin, 2003.

[147] U. Heinzmann. Photoemission and Absorption Spectroscopy of Solids and Interfaces with Synchrotron Radiation. In M. Campagna and R. Rosei, editors, *Proceedings of the International School of Physics "Enrico Fermi"*, page 463. North-Holland, 1990.

[148] P. Stoppmanns, B. Schmiedeskamp, B. Vogt, N. Müller, and U. Heinzmann. Spin Resolved Auger-Spectroscopy on Rb-Layers after Core-Hole Creation by Circularly Polarized VUV-Light. *Physica Scripta*, T41:190–193, 1992.

[149] N.A. Cherepkov. Spin Polarization of Photoelectrons ejected from unpolarised atoms. *J. Phys. B: At. Mol. Opt. Phys.*, 12:1279–1296, 1979.

[150] P. Stoppmanns. *Spinaufgelöste Auger-Elektronenspektroskopie an metallischen Alkali-Schichten nach Anregung mit zirkular polarisierter Strahlung.* dissertation, Fakultät für Physik der Universität Bielefeld, 1995.

[151] R. David. *Spinaufgelöste Augerspektroskopie an 3d-Metallen und Jod nach Anregung mit zirkular polarisierter Synchrotronstrahlung.* dissertation, Fakultät für Physik der Universität Bielefeld, 1998.

[152] F. Baudelet. X-ray Magnetic Circular Dichroism. In F. Hippert, E. Geissler, J.L. Hodeau, E. Lelièvre-Berna, and J.-R. Regnard, editors, *Neutron and X-ray Spectroscopy*, Grenoble Sciences, page 103. Springer, 2006.

[153] S. Fiedler. *Magnetische Momente massenselektierter CoPd und FePt Legierungscluster auf Ni/Cu(100) untersucht mittels XMCD.* dissertation, Department Physik der Universität Hamburg, 2010.

[154] J. Stöhr and Y. Wu. In A.S. Schlachter and F.J. Wuillcumier, editors, *New Directions in Research with Third-Generation Soft X-Ray Synchrotron Radiation Sources*, page 221. Kluwer Academic Publishers, Netherlands, 1994.

[155] M.D. Sacher. *Charakterisierung der Barrieren-Grenzflächen magnetischer Tunnelelemente mit halbmetallischen Elektroden.* dissertation, Fakultät für Physik der Universität Bielefeld, 2007.

[156] B.T. Thole, P. Carra, F. Sette, and G. van der Laan. X-ray Circular Dichroism as a Probe of Orbital Magnetization. *Phys. Rev. Lett.*, 68:1943, 1992.

[157] P. Carra, B.T. Thole, M. Altarelli, and X. Wang. X-ray Circular Dichroism and Local Magnetic Fields. *Phys. Rev. Lett.*, 70:694, 1993.

[158] C.T. Chen, Y.U. Idzerda, H.-J. Lin, N.V. Smith, G. Meigs, E. Chaban, G.H. Ho, E. Pellegrin, and F. Sette. Experimental Confirmation of the X-Ray Magnetic Circular Dichroism Sum Rules for Iron and Cobalt. *Phys. Rev. Lett.*, 75:152, 1995.

[159] R. Wu, D. Wang, and A.J. Freeman. First Principles Investigation of the Validity and Range of Applicability of the X-Ray Magnetic Circular Dichroism Sum Rule. *Phys. Rev. Lett.*, 71:3581, 1993.

[160] R. Wu and A.J. Freeman. Limitation of the Magnetic-Circular-Dichroism Spin Sum Rule for Transition Metals and Importance of the Magnetic Dipole Term. *Phys. Rev. Lett.*, 73: 1994, 1994.

[161] G. Schütz, P. Fischer, K. Attenkofer, M. Knülle, D. Ahlers, S. Stähler, C. Detlefs, H. Ebert, and F.M.F. de Groot. X-ray magnetic circular dichroism in the near and extended absorption edge structure. *J. Appl. Phys.*, 76:6453, 1994.

[162] G. van der Laan. Sum rule practice. *J. Synchrotron Rad.*, 6:694–695, 1999.

[163] A.I. Nesvizhskii, A.L. Ankudinov, and J.J. Rehr. Normalization and convergence of x-ray absorption sum rules. *Phys. Rev. B*, 63:094412, 2001.

[164] Y. Teramura, A. Tanaka, and T. Jo. Effect of Coulomb Interaction on the X-Ray Magnetic Circular Dichroism Spin Sum Rule in $3d$ Transition Elements. *J. Phys. Soc. Jap.*, 65: 1053–1055, 1996.

[165] C. Piamonteze, P. Miedema, and F.M.F de Groot. The accuracy of the spin sum rule in XMCD. *J. Phys.: Conf. Series*, 190:012015, 2009.

[166] C. Piamonteze, P. Miedema, and F.M.F. de Groot. Accuracy of the spin sum rule in XMCD for the transition-metal L edges from manganese to copper. *Phys. Rev. B*, 80:184410, 2009.

[167] K. Kuepper, M. Raekers, C. Taubitz, M. Uhlarz, C. Piamonteze, F.M.F. de Groot, E. Arenholz, V. R. Galakhov, Ya. M. Mukovskii, and M. Neumann. The x-ray magnetic circular dichroism spin sum rule for $3d^4$ systems: Mn^{3+} ions in colossal magnetoresistance manganites. *J. Phys.: Condens. Matter*, 24:435602, 2012.

[168] F. Reinert and S. Hüfner. Photoemission spectroscopy–from early days to recent applications. *New Journal of Physics*, 7:97, 2005.

[169] K. Siegbahn, C. Nordling, A. Fahlman, K. Hamrin, J. Hedman, G. Johansson, T. Bergmark, S.E. Karlsson, J. Lindgren, and B. Lindberg. *Electron Spectroscopy for Chemical Analysis. Atomic, Molecular and Solid State Structure Studies by Means of Electron Spectroscopy.* Almquist and Wiksells, Uppsala, 1967.

[170] K. Siegbahn, C. Nordling, G. Johansson, J. Hedman, P.F. Hedén, K. Hamrin, U. Gelius, T. Bergmark, L.O. Werme, R. Manne, and Y. Baer. *ESCA Applied to Free Molecules.* North-Holland Amsterdam London, 1969.

[171] K. Siegbahn. Electron Spectroscopy for Atoms, Molecules and Condensed Matter. In T. Frängsmyr and G. Ekspong, editors, *Nobel Lectures in Physics 1981-1990*, page 63. World Scientific Publishing Co. Singapore, 1993.

[172] C. Nordling, E. Sokolowski, and K. Siegbahn. Precision Method for Obtaining Absolute Values of Atomic Binding Energies. *Phys. Rev.*, 105:1676, 1957.

[173] L. Hedin, J. Michiels, and J. Inglesfield. Transition from the adiabatic to the sudden limit in core-electron photoemission. *Phys. Rev. B*, 58:15565, 1998.

[174] S. Tougaard and P. Sigmund. Influence of elastic and inelastic scattering on energy spectra of electrons emitted from solids. *Phys. Rev. B*, 25:4452, 1982.

[175] C.N. Berglund and W.E. Spicer. Photoemission Studies of Copper and Silver: Theory. *Phys. Rev.*, 136:A1030–A1044, 1964.

[176] R.H. Fowler. The Analysis of Photoelectric Sensitivity Curves for Clean Metals at Various Temperatures. *Phys. Rev.*, 38:45, 1931.

[177] N.V. Smith. Photoemission properties of metals. *C R C Critical Reviews in Solid State Sciences*, 2:45–83, 1971.

[178] G.E. McGuire. Instrumental Methods in ESCA. In *Applied Electron Spectroscopy For Chemical Analysis*, page 1. Wiley Interscience New York, 1982.

[179] M.E. Rudd. Electrostatic Analyzers. In *Low Energy Electron Spectrometry*, page 17. Wiley Interscience New York, 1972.

[180] J. Kirschner. Sources and Detectors for Polarized Electrons. In *Polarized Electrons in Surface Physics*, page 245. World Scientific Publishing Co. Singapore, 1985.

[181] R. Bertacco, D. Onofrio, and F. Ciccacci. A novel electron spin-polarization detector with very large analyzing power. *Rev. Sci. Instrum.*, 70:3572, 1999.

[182] M. Escher, N.B. Weber, M. Merkel, L. Plucinski, and C.M. Schneider. FERRUM: A New Highly Efficient Spin Detector for Electron Spectroscopy. *e-J. Surf. Sci. Nanotech.*, 9: 340–343, 2011.

[183] A. Gellrich, K. Jost, and J. Kessler. Elimination of instrumental asymmetries in electron polarization analysis. *Rev. Sci. Instrum.*, 61:3399, 1990.

[184] J.R. Taylor. *An introduction to error analysis*, page 73. University Science Books, 1997.

[185] K. Weltner, J. Grosjean, W.J. Weber, and P. Schuster. *Mathematics for Physicists and Engineers*, page 547. Springer Verlag Heidelberg London New York, 2009.

[186] A. Helmstedt, N. Müller, A. Gryzia, N. Dohmeier, A. Brechling, M. D. Sacher, U. Heinzmann, V. Hoeke, E. Krickemeyer, T. Glaser, S. Bouvron, M. Fonin, and M. Neumann. Spin resolved photoelectron spectroscopy of $[\mathrm{Mn}_6^{\mathrm{III}}\mathrm{Cr}^{\mathrm{III}}]^{3+}$ single-molecule magnets and of manganese compounds as reference layers. *J. Phys.: Condens. Matter*, 23:266001, 2011.

[187] N. Müller, T. Khalil, M. Pohl, T. Uphues, M. Polcik, O. Rader, F. Heigl, K. Starke, S. Fritzsche, N. M. Kabachnik, and U. Heinzmann. Interference of spin states in resonant photoemission induced by circularly polarized light from magnetized Gd. *Phys. Rev. B*, 74:161401R, 2006.

[188] N. Müller, R. David, G. Snell, R. Kuntze, M. Drescher, N. Böwering, P. Stoppmanns, S.-W. Yu, U. Heinzmann, J. Viefhaus, U. Hergenhahn, and U. Becker. Spin resolved Auger electron spectroscopy after photoexcitation with circularly polarized radiation from the BESSY crossed undulator. *J. Electron Spectrosc. Relat. Phenom.*, 72:187–193, 1995.

[189] R. David, P. Stoppmanns, S.-W. Yu, R. Kuntze, N. Müller, and U. Heinzmann. Circularly polarized undulator radiation from the new double crossed undulator beamline at BESSY and its first use for spin resolved Auger electron emission spectroscopy. *Nucl. Instrum. Meth. A*, 343:650–654, 1994.

[190] manufacturer: Dr. Sjuts Optotechnik, Am Schlehdorn 1, D-37077 Göttingen.

[191] I. Lindau, P. Pianetta, K. Yu, and W.E. Spicer. The intrinsic linewidth of the 4f levels in gold as determined by photoemission. *Phys. Lett. A*, 54:47–48, 1975.

[192] D.J. O'Connor, B.A. Sexton, and R.St.C. Smart, editors. *Surface Analysis Methods in Materials Science*, page 175. Springer Verlag Berlin Heidelberg New York, 2003.

[193] L. G. Gray, M. W. Hart, F. B. Dunning, and G. K. Walters. Simple, compact, medium-energy Mott polarization analyzer. *Ref. Sci. Instrum.*, 55:88–91, 1983.

[194] P. Bauer. *Longitudinale und transversale Spinpolarisation bei der Beugung niederenergetischer Elektronen: Einfluss von Zeitumkehr, Kristallsymmetrie und Kristallpotential.* dissertation, Fakultät für Physik der Technischen Universität München, 1980.

[195] manufacturer: Omicron NanoTechnology GmbH, Limburger Strasse 75, D-65232 Taunusstein.

[196] M. Prinz, M. Raekers, M. Neumann, K. Kuepper, S. Khanra, T. Weyhermüller, and P. Chaudhuri. Synthesis, Structure, and Valency Verification of a $Mn_6^{III}O_2$-Cluster. *Z. Phys. Chem.*, 223:145–155, 2009.

[197] S. Voss, M. Burgert, M. Fonin, U. Groth, and U. Rüdiger. A comparative study on the deposition of Mn_{12} single molecule magnets on the Au(111) surface. *Dalton Trans.*, 2008:499–505, 2008.

[198] M. Mannini, P. Sainctavit, R. Sessoli, C. Cartier dit Moulin, F. Pineider, M.-A. Arrio, A. Cornia, and D. Gatteschi. XAS and XMCD Investigation of Mn_{12} Monolayers on Gold. *Chem. Eur. J.*, 14:7530–7535, 2008.

[199] A. Saywell, A.J. Britton, N. Taleb, M. del Carmen Giménez-López, N.R. Champness, P.H. Beton, and J.N. O'Shea. Single molecule magnets on a gold surface: in situ electrospray deposition, x-ray absorption and photoemission. *Nanotechnology*, 22:075704, 2011.

[200] A. Gryzia, H. Predatsch, A. Brechling, V. Hoeke, E. Krickemeyer, C. Derks, M. Neumann, T. Glaser, and U. Heinzmann. Preparation of monolayers of $[Mn_6^{III}Cr^{III}]^{3+}$ single-molecule magnets on HOPG, mica and silicon surfaces and characterization by means of non-contact AFM. *Nanoscale Research Letters*, 6:486, 2011.

[201] E. Wendler-Kalsch and H. Gräfen. *Korrosionsschadenkunde*, pages 335–337. Springer-Verlag Berlin Heidelberg, 1998.

[202] E. Wendler-Kalsch. Corrosion and stress corrosion cracking of iron materials in methanol under practical conditions. In *8^e Congrès Européen de Corrosion*, pages 56–1 to 56–6. Centre Français de la Corrosion, Paris, 1985.

[203] R. T. Bayard and D. Alpert. Extension of the Low Pressure Range of the Ionization Gauge. *Rev. Sci. Instr.*, 21:571, 1950.

[204] E. A. Trendelenburg. *Ultrahochvakuum*, page 26. Verlag G. Braun Karlsruhe, 1963.

[205] R. N. Bloomer and M. E. Haine. The electronic clean-up of gases in sealed-off vacuum systems. *Vacuum*, 3:128, 1953.

[206] H. S. W. Massey. Excitation and Ionization of Atoms by Electron Impact. In S. Flügge, editor, *Encyclopedia of Physics*, volume 36, pages 880,957,986,992,1023. Springer Verlag Berlin Göttingen Heidelberg, 1956.

[207] J. Yano, J. Kern, K.-D. Irrgang, M. J. Latimer, U. Bergmann, P. Glatzel, Y. Pushkar, J. Biesiadka, B. Loll, K. Sauer, J. Messinger, A. Zouni, and V.K. Yachandra. X-ray damage to the Mn_4Ca complex in single crystals of photosystem II: A case study for metalloprotein crystallography. *PNAS*, 102:12047–12052, 2005.

[208] L. Rulíšek and U. Ryde. Structure of Reduced and Oxidized Manganese Superoxide Dismutase: A Combined Computational and Experimental Approach. *J. Phys. Chem. B*, 110:11511–11518, 2006.

[209] M. Grabolle, M. Haumann, C. Müller, P. Liebisch, and H. Dau. Rapid Loss of Structural Motifs in the Manganese Complex of Oxygenic Photosynthesis by X-ray Irradiation at 10-300 K. *J. Biol. Chem.*, 281:4580–4588, 2006.

[210] C. M. Wilmot, T. Sjögren, G. H. Carlsson, G. I. Berglund, and J. Hajdu. Defining Redox State of X-Ray Crystal Structures by Single-Crystal Ultraviolet-Visible Microspectrophotometry. *Methods Enzymol.*, 353:301–318, 2002.

[211] T. Bücher and M. Klingenberg. Wege des Wasserstoffs in der lebendigen Organisation. *Angew. Chem.*, 70:552–570, 1958.

[212] P. K. Pal, S. Chowdhury, M. G. B. Drew, and D. Datta. The electrooxidation of the tetraphenylborate ion revisited. *New J. Chem.*, 26:367–371, 2002.

[213] A. F. Holleman, E. Wiberg, and N. Wiberg. *Lehrbuch der Anorganischen Chemie*, pages 480–481. deGruyter, Berlin, 2007.

[214] N. Schmidt, A. Scheurer, S. Sperner, and R. H. Fink. Microspectroscopic Analysis of the X-Ray-induced Photoreduction in Fe- and Mn-containing SMMs. *Z. Naturforsch.*, 65b: 390–398, 2010.

[215] R. W. Saalfrank, I. Bernt, E. Uller, and F. Hampel. Template-Mediated Self Assembly of Six- and Eight-Membered Iron Coronates. *Angew. Chem. Int. Ed. Engl.*, 36:2482–2485, 1997.

[216] R. W. Saalfrank, I. Bernt, M. M. Chowdhry, F. Hampel, and G. B. M. Vaughan. Ligand-to-Metal Ratio Controlled Assembly of Tetra- and Hexanuclear Clusters Towards Single-Molecule Magnets. *Chem. Eur. J.*, 7:2765–2769, 2001.

[217] R. W. Saalfrank, A. Scheurer, R. Prakash, F. W. Heinemann, T. Nakajima, F. Hampel, R. Leppin, B. Pilawa, H. Rupp, and P. Müller. Synthesis, Redox, and Magnetic Properties of a Neutral, Mixed-Valent Heptanuclear Manganese Wheel with S=27/2 High-Spin Ground State. *Inorg. Chem.*, 46:1586–1592, 2007.

[218] R. W. Saalfrank, T. Nakajima, N. Mooren, A. Scheurer, H. Maid, F. Hampel, C. Trieflinger, and J. Daub. Syntheses and Properties of Metal-Centered Mixed-Valent $[NEt_4]\{Mn^{II}\subset[Mn^{II}_3Mn^{III}_3Cl_6(L)_6]\}$ Manganese Wheels. *Eur. J. Inorg. Chem.*, 2005:1149–1153, 2005.

[219] A. Kikas, A. Maiste, A. Saar, and M. Elango. $L_{23}MM$ Resonant Auger spectra of Mn in $KMnF_3$. *J. Electron Spectrosc. Relat. Phenom.*, 72:113–117, 1995.

[220] J. Vayrynen. Differences in $L_{23}MM$ Auger electron spectra of atomic and metallic manganese. *J. Electron Spectrosc. Relat. Phenom.*, 22:27–42, 1981.

[221] Yu. Kucherenko, B. Sincović, E. Shekel, P. Rennert, and S. Hubert. Spin-resolved Fe $L_3M_{2,3}M_{2,3}$ and $L_3M_{2,3}V$ Auger transitions on and off resonance by excitation with linearly polarized photons. *Phys. Rev. B*, 62:5733–5741, 2000.

[222] E.D. Roberts, P. Weightman, and C.E. Johnson. Photoelectron and $L_{23}MM$ Auger electron energies for arsenic. *J. Phys. C: Solid State Phys.*, 8:1301, 1975.

[223] P. Weightman, E.D. Roberts, and C.E. Johnson. $L_{23}MM$ Auger processes in selenium. *J. Phys. C: Solid State Phys.*, 8:550, 1975.

[224] B. Gilbert, B.H. Frazer, A. Belz, P.G. Conrad, K.H. Nealson, D. Haskel, J.C. Lang, G. Srajer, and G. De Stasio. Multiple Scattering Calculations of Bonding and X-ray Absorption Spectroscopy of Manganese Oxides. *J. Phys. Chem. A*, 107:2839–2847, 2003.

[225] S. Tougaard. Practical algorithm for background subtraction. *Surface Science*, 216: 343–360, 1989.

[226] H. Klar. Spin polarisation of Auger electrons. *J. Phys. B: Atom. Molec. Phys.*, 13:4741–4749, 1980.

[227] N.M. Kabachnik and O.V. Lee. Spin polarisation of Auger electrons following atomic photoionisation by circularly polarised x-rays. *J. Phys. B: At. Mol. Opt. Phys.*, 22:2705–2716, 1989.

[228] N.M. Kabachnik and I.O. Sazhina. On the problem of a 'complete' experimental characterisation of Auger decay. *J. Phys. B: At. Mol. Opt. Phys.*, 23:L353–L357, 1990.

[229] L. Yin, T. Tsang, and I. Adler. Electron delocalization and the characterization of the L_3MM Auger spectra of $3d$ transition metals. *Phys. Rev. B*, 15:2974, 1977.

[230] L. Yin, T. Tsang, I. Adler, and E. Yellin. L-S coupling interpretation of high-resolution LMM Auger spectra of Cu and Zn. *J. Appl. Phys.*, 43:3464, 1972.

[231] M. Cini. Density of states of two interacting holes in a solid. *Solid State Comm.*, 20: 605–607, 1976.

[232] G.A. Sawatzky. Quasiatomic Auger Spectra in Narrow-Band Metals. *Phys. Rev. Lett.*, 39: 504–507, 1977.

[233] D.M. Sherman. The electronic structure of manganese oxide minerals. *Am. Mineralogist*, 69:788–799, 1984.

[234] H. Kurata and C. Colliex. Electron-energy-loss core-edge structures in manganese oxides. *Phys. Rev. B*, 48:2102, 1993.

[235] R. Norrestam. α-Manganese(III) Oxide – a C-Type Sesquioxide of Orthorhombic Symmetry. *Acta Chem. Scand.*, 21:2871–2884, 1967.

[236] S. Khanra, K. Kuepper, T. Weyhermüller, M. Prinz, M. Raekers, S. Voget, A.V. Postnikov, F.M.F de Groot, S.J. George, M. Coldea, M. Neumann, and P. Chaudhuri. Star-Shaped Molecule of $\mathrm{Mn}_4^{\mathrm{II}}\mathrm{O}_6$ Core with an $S_t = 10$ High-Spin State. A Theoretical and Experimental Study with XPS, XMCD, and Other Magnetic Methods. *Inorg. Chem.*, 47:4605–4617, 2008.

[237] N.A. Cherepkov and V.V. Kuznetsov. Optical activity of polarised atoms. *J. Phys. B: At. Mol. Opt. Phys.*, 22:L405–L409, 1989.

[238] K. Starke, E. Navas, E. Arenholz, Z. Hu, L. Baumgarten, G. van der Laan, C.T. Chen, and G. Kaindl. Magnetic circular dichroism in $4d \rightarrow 4f$ resonant photoemission and photoabsorption of Gd metal. *Phys. Rev. B*, 55:2672, 1997.